Studies on the Friction of Structured Interfaces, the Static Friction Peak in Reciprocating Sliding and the Role of Friction in Triboelectrification.

By

Saad Bin Jaber

Submitted in fulfilment of the requirements for the degree of Doctor of Philosophy in Mechanical Engineering.

April 2023

James Watt School of Engineering

College of Science and Engineering

University of Glasgow, UK

Author’s declaration

“I declare that, except where explicit reference is made to the contribution of others, this dissertation is the result of my own work and has not been submitted for any other degree at the University of Glasgow or any other institution.”

Signature:

Printed name: **Saad Bin Jaber**

Abstract

This project investigates the frictional behaviour of contacting surfaces at different test conditions to better understand the contact mechanism. It aims to implement novel techniques and theoretical approaches to acquire more control over the friction response of contacting surfaces. It has been suggested that surface structuring is beneficial for controlling the friction response. This project utilises photochemical etching (photolithography) to produce micro-trenches (square-wave features). Five different sample categories were prepared with different micro-feature widths. These structured features were placed in contact with unstructured silicon surfaces. The silicon samples possess idealised surface conditions with sub 1 nm roughness and flatness of 1 µm. The tests were carried out on a bespoke friction rig. This research topic is directed to examine the applicability of Amontons' first and second laws of friction on these structured features with nanoscale roughness. It has been found that the COF of these structured surfaces is independent of the manipulation of the feature contact area and normal load. This means that the real contact area was not varied with the different feature contact areas. To validate this assumption, two theoretical approaches using the Bush, Gibson and Thomas (GBT) model and Boundary Element Method (BEM) were implemented. These approaches estimate the real contact area by inserting experimental parameters and roughness data of the contacting surfaces. The models' results showed that the real contact area was independent of the changes in the feature contact area. The experimental and model results indicate that the nanoscale roughness on the raised features was sufficient for the friction laws to be obeyed.

The second part of the thesis concerns the static friction peak in reciprocating sliding. It has been noticed that the peak has not been observed in the studies of friction hysteresis loops. The purpose of studying this aspect of friction is to determine the reason for the absence of the static friction peak in commonly published hysteresis loops. Experiments were performed on the unstructured silicon samples using the friction rig. The tests showed that the peak was apparent in the initial cycles. It then started to decay towards the end of the test. It is believed that sliding roughened the surfaces resulting in a lower real contact area. The reduction in the real contact area decreased static friction towards kinetic friction leading to burying the peak. This assumption was verified by an adhesive contact model. It is worth noting that the only variable in the model was the roughness data, to inspect the impact of wear through changes in surface roughness. The model showed a similar trend as the experiment indicating that wear was responsible for the disappearance of the peak. The reason for not observing the peak in the literature is most probably because the reported data was recorded well after the peak is buried.

The final research topic aims to investigate the frictional and electrical behaviour of triboelectric layers via performing a triboelectric nanogenerator study (TENG). There has been a lack of studies on the role of friction in triboelectrification. To perform the tests, electrical measurements were incorporated into the friction rig to simultaneously measure friction and electrical output to find whether friction can be correlated with the electrical output. Another main goal of this topic is to systematically compare the electrical output of the two main modes of TENG (sliding and vertical contact separation modes). In a sense, a direct comparison of contact electrification and triboelectrification for exactly the same material pair and test conditions etc. was performed. The friction and output voltage showed almost the same trend suggesting that they are influenced by the same source. It has also resulted that the existence of friction in the sliding mode was advantageous. It helps acquire more triboelectric charges giving rise to higher outputs. It should be noted that triboelectric layers in the sliding mode are susceptible to wear requiring careful attention and future study.

Acknowledgment

I would like firstly to thank my principal supervisor Dr Daniel Mulvihill for his unlimited support, guidance and patience throughout my PhD. I really appreciate the opportunity that he's given me to work in this interesting project. I've gained enormous knowledge from him. I consider myself lucky to be supervised by Dr Mulvihill. I'd like also to express my thanks to the co-supervisors, Prof Nikolaj Gadegaard and Dr Mehmet Kartal for their guidance. I'm as well very grateful for Dr Yang Xu and Dr Charchit Kumar for their endless support and guidance particularly during the experiments designs. Without their help, the project wouldn't have reached the final stage. I am thankful to all of the technicians in the James Watt Nanofabrication centre who helped me with preparing and characterising my samples. I should also thank Dr Alex Hamilton and Dr Jacek Olender for giving me their precious time to help me with performing some aspects of my experiments.

My sincere gratitude to the Saudi Arabian Cultural Bureau in London and Imam Mohammed bin Saud Islamic university (IMSIU) in Riyadh for sponsoring my studies and facilitating everything related to this sponsorship. I am also grateful for IMSIU to for allowing me to pursue my study.

My final thanks are to my family (father, mother and siblings) who have always given me support, encouragement and prayers throughout my time abroad. Last, but not the least, I'm sincerely grateful for my wife (Mrs Rawan Al-Muhayya) for enduring the difficult times during the PhD study. There've been so many times where the work was difficult, but she was so patient and very understanding. She was very supportive and I really appreciate that.

List of Publications

1- **Saad Bin Jaber**, Alex Hamilton, Yang Xu, Mehmet E. Kartal, Nikolaj Gadegaard, Daniel M. Mulvihill, “Friction of flat and micropatterned interfaces with nanoscale roughness”, *Tribology International*, Volume 153, 2021, 106563, ISSN 0301-679X, https://doi.org/10.1016/j.triboint.2020.106563.

2- **Saad Bin Jaber**, Yang Xu, Mehmet E. Kartal, Nikolaj Gadegaard, Daniel M. Mulvihill, “The static friction peak in reciprocating sliding”, *Tribology International*, Volume 180, 2023, 108240, ISSN 0301-679X, https://doi.org/10.1016/j.triboint.2023.108240

List of Figures

Fig. 1. 1. a simplified representation of the difference between rolling and sliding 2
Fig. 1. 2. A schematic of the friction hysteresis loops identifying the point of interest (static friction peak) 5

Fig. 2. 1. A schematic to represent the effect of the normal load on the atomic scale between an indenter and asperity atoms of the counter surface. (a) The indenter is being pressed, but still, the load does not transmit to the asperity atoms. (b) The (critical) load is forcing the atoms to re-distribute. (c) The atoms are in their new stable state [37]. 11
Fig. 2. 2. Typical behaviour of the COF throughout sliding. It begins with an initial value which increases towards the maximum and then drops slightly to the sliding (stable) COF [7]. 13
Fig. 2. 3. Representation of the six stages of the COF in a frictional interface [7]. 13
Fig. 2. 4. A wear particle interaction in (a) hard-hard interface, (b) hard-soft interface and (c) the size of the wear particle [7]. 16
Fig. 2. 5. Illustration of the friction apparatus. key components: Q- upper surface (spherical slider), YZ- Duralumin arm, XX- Bifilar suspension, P- bottom surface, R- circular spring to apply the load, J- pulley, K- axle [42]. 23
Fig. 2. 6. Utilisation of a pneumatic cylinder for applying normal load on a specimen [45]. 24
Fig. 2. 7. Schematic diagram of deflections on vertical and horizontal axes occurring on the leaf flexures [15]. 25
Fig. 2. 8. Measurement of the real contact area carried out by light reflection on a Perspex truncated prism as a lower surface (B) in contact with a Perspex surface (A) that is fixed to a holder (D) through a rubber sheet (C) [34]. 26
Fig. 2. 9. Optical image of the reflected light through the truncated prism. The dark spots are the points of contact (destructive interference). The size and number of these spots can be related to the applied contact pressure [34]. 26
Fig. 2. 10. The parameters that affect the trapping mechanism [38]. 31
Fig. 2. 11. A typical frictional hysteresis loop from a reciprocating sliding test. K_t is tangential stiffness (adapted from [77]). 32
Fig. 2. 12. The impact of wear caused by the reciprocating sliding is sketched to showcase how the surfaces are affected by sliding cycles [78]. 33
Fig. 2. 13. The friction hysteresis loops are characterised into three main stages: (a) partial slip, (b) mixed stick-slip, and (c) gross slip [78]. 34

Fig. 2. 14. A schematic to illustrate the edge effects of a frictional interface into two possible cases: (a) interactions at the macroscale, and (b) microscopic interactions (peaks and troughs) [81]. 37
Fig. 2. 15. A visual explanation of the electron transfer in a dielectric-dielectric interface for insulators whose electronic structure can be represented by energy band gaps. The surfaces are initially apart. Then they are forced to contact resulting in an electron transfer. The surfaces are separated again and become electrically charged. The transferred electron cannot return to its original position unless it gains thermal energy [98]. 42
Fig. 2. 16. The atomic-scale interactions between two contacting atoms: (a) The two atoms are in the equilibrium state and separated by a bond length, (b) The atoms are in the repulsive region with a separation distance smaller than the bond length and (c) The atoms are separated by a larger distance than the bond length and they are in the attractive region [88]..... 43
Fig. 2. 17. Representation of the four main types of TENG showing the possible application of each type [110]..... 45
Fig. 2. 18. Schematic for misalignment that might occur in full lateral separation..... 50

Fig. 3. 1. A diagram of the inclined plane showing the forces affecting the interface between the silicon surfaces. The force of gravity is equal to mass (m) x gravitational acceleration (g), the normal load is represented by mg $\cos(\theta)$ and friction force is obtained by mg $\sin(\theta)$..... 57
Fig. 3. 2. Schematic of the friction rig setup: (1) Upper specimen, (2) Lower specimen, (3) Upper backing block, (4) Lower backing block, (5) X-shape arm, (6) Button load cell, (7) Connecting rod, (8) Motorised linear stage, (9) Low friction ball bearing, (10) Base plate and (11) Tension/compression load cell (12) and (13) stopper set. 58

Fig. 4. 1. Photolithographic etching steps for structured surface fabrication. 66
Fig. 4. 2. Schematic representation of feature contact area ratios. Feature contact area ratio $\mathrm{AnfAn} = \lambda\mathrm{f}\lambda\mathrm{f} + \lambda\mathrm{c}$. 66
Fig. 4. 3. Schematic of the experimental 'sled type' friction rig: (1) Upper silicon specimen, (2) Lower silicon specimen (always flat), (3) Upper backing plate, (4) Lower backing plate, (5) Upper arm, (6) Miniature button load cell, (7) Connecting rod, (8) Linear bearing, (10) Base plate, (11) Tension/compression load cell and (12) Stoppers..... 67
Fig. 4. 4. Representative tangential force versus displacement plots for surfaces having feature contact area ratios (AnfAn) of: (a) 0.2, (b) 0.4, (c) 0.6, (d) 0.8 and (e) 1. Each plot shows the effect of varying the normal load P (see legend). 69

Fig. 4. 5. (a) Static friction force F versus normal load P (for all feature contact area instances) and (b) coefficient of static friction μ versus normal load P (also for all feature contact area instances). Feature contact area ratio ($AnfAn$) is given in the legend. 70
Fig. 4. 6. Coefficient of static friction μversus feature contact area ratio ($AnfAn$). 70
Fig. 4. 7. Predicted real area of contact A_r versus feature contact area ratio (A_{nf}/A_n) as estimated by (a) the BGT model and (b) the BEM method. Normal load P = 50 N. Nominal areas (i.e. 10 x 10 mm^2) and feature areas etc. are the same as for the experimental specimen. 72

Fig. 5. 1. Unidirectional sliding curve between silicon surfaces under 30 N normal load (Adapted from Bin Jaber et al [135]). 76
Fig. 5. 2. Representative friction hysteresis loops for contact between aluminium bronze and steel for an experimental study performed by Hintikka et al. [141] (The graph is adapted). 77
Fig. 5. 3. The components that affect the liquid-solid interface according to Young's equation [146]. 83
Fig. 5. 4. Contact angle measurements on silicon samples performed to calculate the surface energy of the silicon surface. 85
Fig. 5. 5. The relative relationship between the liquid surface tension and the surface energy of a solid [151]. 85
Fig. 5. 6. Experimental sliding curves with varying dwell time: (a) no dwell time, (b) Dwell time = 2 seconds, (c) Dwell time= 4 seconds, (d) Dwell time= 10 seconds and (e) Dwell time= 20 seconds. The legend shows the colours that represent the number of cycles. The dwell time refers to the time for which the contact is held static at the end of each sliding stroke. 88
Fig. 5. 7. Representative sliding curves from (a) experiment and (b) model prediction illustrate the static peak evolution with cycles. The experiment graph shows only the forward direction to help compare with the model prediction. 91
Fig. 5. 8. The relative friction difference ($\Delta F/F_k$) versus cycles for (a) the five tests and (b) the average. The inset equation is for the best-fitted curve. 91
Fig. 5. 9. Predictions of the model of the relative friction difference ($\Delta F/F_k$) versus cycles for (a) individual samples and (b) a comparison between experimental and model averages. 92
Fig. 5. 10. Normalised real contact area versus tangential displacement illustrating the stuck contribution (black :) and sliding contribution (blue --) to the total of the real contact area (red -). The graph shows the evolution of the real contact area at Cycle 1 of the sample results presented in Fig. 5. 7. 93

Fig. 5. 11. Averages of (a) real contact area in stuck stage normalized by the nominal contact area versus cycles and (b) static friction versus cycles as predicted from the present model with a fitted curve equation inserted. 93

Fig. 6. 1. Synchronous friction-voltage test rig of freestanding TENG: (1) PET layer, (2) Copper strips, (3) Acrylic backing plate, (4) Glass plate, (5) Moving metal plate, (6) Button load cell, (7) x-shaped arm, (8) Springs, (9) Stoppers, (10) Connecting rod, (11) Tension/compression load cell, (12) Motorised linear stage, ... 100

Fig. 6. 2. Illustration of the S-TENG test mechanism showing the relative movement between the triboelectric layers and corresponding curves of friction and voltage. 102

Fig. 6. 3. The output voltage versus the sliding speed with applying different normal loads. 103

Fig. 6. 4. Frictional behaviour of the triboelectric layers showing: (a) Dynamic friction versus sliding speed and (b) COF against normal load. 104

Fig. 6. 5. The relationship between the output voltage and frequency with different normal loads of a CS-TENG test. 105

Fig. 6. 6. The voltage signals for (a) S-TENG and (b) CS-TENG tests experiencing different normal loads. 105

Fig. 6. 7. Current and voltage measurements of (a) S-TENG and (b) CS-TENG. Multiplication of these measurements provide the electrical power of (c) S-TENG and (d) CS-TENG. 106

Fig. 6. 8. The stability of the output voltage for an S-TENG device experiencing 1500 cycles with 10 N normal load and 125 mm/s sliding speed. 107

Fig. 6. 9. Optical images of the Cu surface before (a) and after (b) testing. 107

List of Tables

Table 4. 1. Mean RMS surface roughness Rq before and after testing. Roughness values are the mean of five different scans per sample for each of the five repeat tests (i.e. mean of 25 measurements). Bracketed values are standard deviations. 68
Table 4. 2. Input values of the parameters inserted in Eq. (4) to obtain the contact area ratio ($E*$= 181 Gpa). 72

Table 5. 1. Total surface tension, dispersive surface tension and polar surface tension of the liquids used in the measurement of surface energy obtained from [159] and [163]. 84
Table 5. 2. Roughness inputs used to extract the model results. These parameters were accompanied with a list of constants as follows: E^*= 181 GPa, τ_0= 10 GPa, ν= 0.272, w= 42.8 x 10^{-6} mJ/mm^2, $\lambda = 0.22$ and $\varepsilon = 0.2$ nm. 86
Table 5. 3. Average RMS roughness Rq and average RMS asperity peak height σs for silicon samples before and after 100 cycles of reciprocating sliding (bracketed values are standard deviations). 89

Abbreviations

GDP	Gross Domestic Product
COF	Coefficient of friction
TENG	Triboelectric nanogenerators
PET	polyethylene terephthalate
MEMS	Microelectromechanical systems
LST	Laser surface texturing
DLIP	Direct laser interference patterning
PCT	Photochemical texturing
UV	Ultraviolet
LED	Light emitting diode
PTFE	polytetrafluoroethylene
PA	Nylon
Cu	Copper
Al	Aluminium
ITO	Indium tin oxide
CS-TENG	Contact separation mode TENG
S-TENG	Sliding mode TENG
DAQ	Data acquisition
AFM	Atomic force microscope
NI	National instruments
RMS	Root mean square
BGT	Bush, Gibson and Thomas
BEM	Boundary Element Method
PC	Papangelo and Ciavarella

OWRK	Owens, Wendt, Rabel and Kaelbel
SP	Polar surface tension
ST	Total surface tension
SD	Dispersive surface tension

Nomenclature

F	Friction force
P	Normal load
μ	Coefficient of friction
A_r	Real contact area
k	Proportionality constant
n	Exponent
τ_s	Shear strength
µm	Micro-metre
MPa	Mega Pascal
kPa	Kilo Pascal
cm	Centimetre
mm	Millimetre
m	Mass
g	Gravitational acceleration
N	Newtons
nm	Nano-meter
mm^2	Millimetre square
A_{nf}	Nominal feature contact area
A_n	Nominal contact area
μm^2	Micro-metre square
Rq	Root mean square roughness
λ_f	Feature width
λ_c	Feature separation distance
$\overline{p}$	Average contact pressure

E^*	Effective Young's modulus
mm/s	Millimetre per second
Hz	Hertz
η	Asperity density
R	Root mean square asperity radius
σ_s	Asperity height
GPa	Giga Pascal
v	Poisson ratio
E	Young's modulus
γ_l	Total surface tension of liquid
γ_l^d	Dispersive surface tension of liquid
γ_l^p	Polar surface tension of liquid
γ_s	Surface tension of solid
γ_{ls}	Interfacial surface tension
θ	Contact angle
mN	Milli-Newtons
mJ/m^2	Milli-Joule per meter square
F_s	Static friction
F_k	Kinetic friction
$\Delta F/F_k$	Relative friction difference
V	Volt
µA	Micro-Ampere
nA	Nano Ampere
µW	Micro-Watt
GΩ	Giga Ohm

Contents

Author's declaration ii

Abstract iii

Acknowledgment v

List of Publications vi

List of Figures vii

List of Tables xi

Abbreviations xii

Nomenclature xiv

Chapter 1: Introduction 1

Chapter 2: Literature review 7

2.1. Basis of sliding friction: 8

2.2. Components of friction and its interactions 12

2.3. Comparative review on friction of ceramics, metals and polymers 16

2.4. Measurement of friction 22

2.4.1. Tangential movement 22

2.4.2. Application of normal load 23

2.4.3. Measurement of friction force and contact area 24

2.5. Surface texturing 27

2.5.1. Introduction 27

2.5.2. Early stage of surface texturing 27

2.5.3. Novel techniques for texturing 28

2.5.4. Influential factors 29

2.6. Friction in reciprocating sliding 31

2.7. Friction and triboelectrification 38

2.8. Conclusion 52

Chapter 3: Rig description 54

3.1. Challenges in Friction Rig Design 55
3.2. Suggested Design Options 56
3.3. Final friction rig design 57
3.4. Further details of friction rig development 59
3.5. Conclusion 62
Chapter 4: Tailoring the static friction of micropatterned surfaces 63
4.1. Introduction 64
4.2. Surface fabrication and testing 65
4.3. Results and discussion 67
4.4. Conclusion 73
Chapter 5: The static friction peak in reciprocating sliding 75
5.1. Introduction 76
5.2. Experimental procedure 78
5.3. Adhesive friction modelling approach 79
5.3.1. Theoretical background 79
5.3.2. Model input parameters 81
5.4. Results and discussion 86
5.5. Conclusions 94
Chapter 6: The effect of friction on triboelectrification 96
6.1. Introduction: 97
6.2. Experimental procedure: 99
6.3. Results and discussion 101
6.4. Conclusion 108
Chapter 7: Conclusion and future recommendations 109
7.1. Conclusion 110
7.2. Future recommendation 112
Bibliography I
Appendices X

Chapter 1: Introduction

When bodies are brought into contact, attempts to slide them relative to one another gives rise to a resistive tangential force. The limiting maximum value of this force before sliding is known as the static friction force and its value thereupon (i.e. during gross slip) is known as sliding (or kinetic) friction. Friction can be defined as material resistance to a tangential displacement caused by pulling/pushing one surface with respect to the other in the presence of normal load [1]. It is worth noting that a resistive response resulting from an interface occurs even before applying a tangential load [2]. When the interface is pressed by a normal load, it experiences micro deformation resulting in resistive force [2]. Friction can be seen in surfaces experiencing (linear or rotational) sliding or rolling. In principle, these two general friction terms have specific laws that might contradict each other. For example, smooth surfaces in sliding friction tend to be more resistant to tangential movement. This does not agree with the nature of rolling friction, where there is almost no resisting force (the grip between the two surfaces is compromised) if one of the contact pairs is very smooth. In sliding friction, the friction interaction occurs on a single interface (considering only the macroscale level for simplification), whereas, usually multiple discrete interfaces between rollers and a counter surface contribute to rolling friction. Usually, the force required to overcome friction in sliding contacts is much larger than the equivalent in rolling. Fig. 1. 1 illustrates a simplified example to show the main mechanism of these two terms.

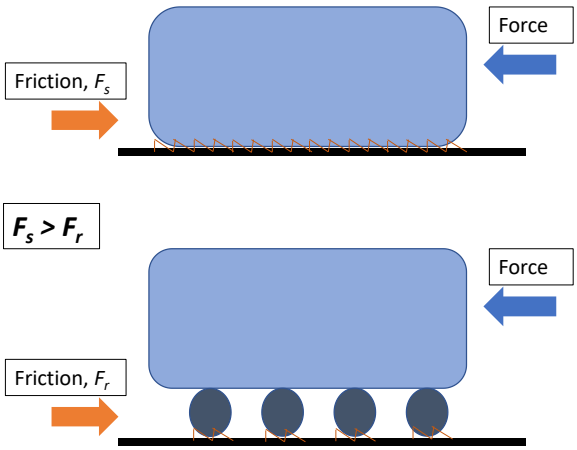

Fig. 1. 1. A simplified representation of the difference between rolling and sliding.

The scope of this study is directed towards investigating friction between flat surfaces in linear sliding (both unidirectional and reciprocating sliding). Friction interactions are ubiquitous in daily life and unfortunately can lead to an economic loss of 5% of GDP (Gross Domestic Product) for developed countries [3]. Better understanding and control of friction promises more efficient designs and energy savings. However, high friction in some applications is required. For example, to increase the effectiveness of turbine blades, so-called under-platform dampers are inserted in the structure of

turbines to increase friction between blade platforms to mitigate any unwanted vibrations [4]. Similarly, high and controlled friction is also desirable in clutch facings to obtain better performance of clutches [5]. Apart from the Renaissance studies carried out by Da Vinci, Friction was first studied by Amontons [6] in 1699. Amontons succeeded in establishing two main relationships for friction stating that the normal load and tangential (friction) force are linearly proportional with the proportionality constant being the coefficient of friction (COF). The second observation noted that the nominal contact area and the friction force generally seemed to be independent. Even though these findings seem simple, they apply to a remarkably wide range of materials and scales (i.e. macro-, micro- and nano-scale). It is commonly acknowledged that the COF is a key factor in any frictional interaction. It provides useful information about the frictional behaviour of contacting surfaces. However, it should be noted that the COF is not a given property of materials [3]. It normally depends on the system condition of a friction test and surface characteristics of mating objects. Consequently, it is vital to pay careful attention to material properties and influential experiment parameters used by other researchers before considering their outcomes. This is because friction results can be considerably altered if just one experiment parameter is changed.

The resistive response from surfaces experiencing tangential load is categorised into three main divisions. They are adhesion, deformation and ploughing [7, 8]. The adhesion contribution can be manipulated by altering real contact area and surface properties [8]. The contribution from adhesion is even observed with zero load due to the Van der Waals and capillary forces [9] and is more seen in light loads [10]. Once the normal load is applied, contributions from deformation and ploughing join the adhesion in the friction equation (i.e. the summation of the three contributions). Deformation occurs at the asperity level and is influenced by contact stress and surface properties [8]. The asperities undergo plastic and/or elastic deformation which gives rise to altering real contact area [2, 7]. Asperity deformation is believed to be a dominant part of friction interaction at the early stage of sliding [11]. As sliding continues, wear particles start to come out from the contacting surfaces causing ploughing [7, 8]. These three main divisions contribute differently to interfacial friction depending on the state of the friction interaction.

Measurement of friction among surveyed studies was mainly performed via the pin-on-disk configuration which includes rotation motion forming a circular contact area to help obtain conformal contact. Additionally, friction experiments in previous studies have been performed on metals and/or coated surfaces to examine their applicability in industry. These studies were significant to understand the friction behaviour of contacting objects, which can help design an effective experiment. Studies on (dry) friction have shown that friction is often derived from a rather small fraction (approximately <1%) of the apparent contact area of mating surfaces (of course, this depends on the normal load).

This small fraction emerges from the surface roughness of the contacting surfaces, constituting the real contact area [12]. Hypothetically, this leads us to the possibility of controlling friction by tailoring this real contact area, as is implied by Bowden and Tabor's understanding of sliding contacts [13]. This possibility suggests the option of structuring surfaces in such a way as to control and tailor friction via the real contact area. Various studies have implemented aspects of this idea to accurately analyse the frictional behaviour of contacting surfaces [9, 14-17]. A Review of these studies will be presented later in Chapter 2.

Chapter 2 will also include a survey on frictional hysteresis loops, as the second experimental portion of the thesis investigates static friction in reciprocating sliding. An explanation of the friction hysteresis loop concepts will be shown and reviewed in Chapter 2. The chapter will also involve a discussion on the apparent absence of the static friction peak from measured hysteresis loops in the literature.

The final part of the literature review (Chapter 2), explores studies relating to friction and triboelectrification focusing on contact charge formation between triboelectric layers and how it can be enhanced. The chapter will try to explore the literature to find a correlation between friction and contact charge formation in TENG devices. It is widely known that tribo-charges are influenced by friction between a contact pair [18-22]. This is more observed in surfaces that experienced stick-slip events [20, 21]. An attempt to explore this correlation in TENGs will be discussed in this final part.

Having considered these studies, an experimental study has been designed to investigate the fundamentals of sliding friction on flat surfaces moving in linear motion. Friction tests in this project involve unidirectional and reciprocating sliding applied on silicon surfaces and metal/polymer interfaces to study the frictional behaviour of silicon with nanoscale roughness and triboelectric properties of a copper and polyethylene terephthalate (PET) interfaces. The testing has been carried out using a bespoke friction rig developed for this work. The rig aimed to enable application of different linear friction test scenarios (i.e. loads, frequencies, stroke distances etc.). Building the rig from scratch was associated with challenges which were mostly overcome during the design stage. A full description of the design and construction of the rig will be presented in Chapter 3. The chapter will discuss the challenges and suggested solutions encountered in rig development and refinement.

The first series of experiments in the thesis explores the idea of controlling friction by manipulating surface features. These features were structured by photolithography (photochemical etching). Altering the features is believed to play an important role in friction force. The work here explores the possibility of tailoring the static friction of structured surfaces experiencing unidirectional sliding. The aim is to re-visit Amontons' first and second laws for these structured surfaces. This work is motivated by the Bowden and Tabor theory of sliding contacts where the real contact area is directly proportional

to friction force [13]. The experiment description and discussion of the results is the subject of Chapter 4. The experimental results were supported by analytical models known as “Bush, Gibson and Thomas” and “Boundary Element Method”. These two model approaches were applied to obtain a thorough explanation of the experimental results.

The second portion of research concerns the existence (or not) of the static friction peak in reciprocating sliding. The main aspect of this work is to explore why the static friction peak is absent from friction force hysteresis loops in the literature. An illustration of the typical hysteresis loops with the absence of the static peak is shown in Fig. 1. 2. This aspect has not been studied at all in the literature. Chapter 5 aims to discuss the existence of the static peak in the loops via applying reciprocating sliding on smooth (unstructured) silicon samples. A detailed discussion of the transition from static to kinetic friction will also be pointed out in Chapter 5. The experiment is accompanied by an adhesive friction model to help rationalise the experimental results.

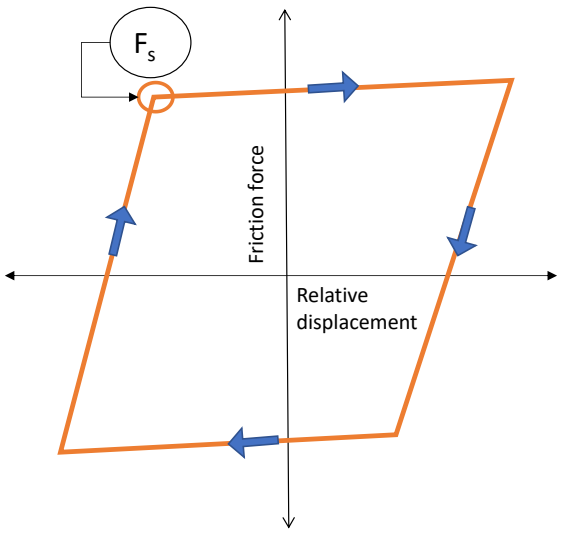

Fig. 1. 2. A schematic of the friction hysteresis loops identifying the point of interest (static friction peak)

Friction between sliding contacts is an important aspect that should always be considered. It was noticed that there has been a lack of studies on the role of tribological parameters such as friction and wear in triboelectrification. The frictional interaction between the triboelectric layers is often ignored in triboelectric studies. Understanding these mechanical aspects of a triboelectric interface is likely to be critical in understanding device performance and boosting electrical outputs. A thorough experimental study that investigates the tribological and triboelectric properties of an interface between triboelectric layers will be presented in Chapter 6, concluding the experimental work of this thesis.

Having performed all these experimental works, a conclusion associated with future work and limitations will be discussed in Chapter 7.

Chapter 2: Literature review

2.1. Basis of sliding friction:

A typical friction mechanism for contacting surfaces consists of primarily a transition from stick to full slip and/or repetitive stick-slip. Observing such a mechanism is dominated by the nature of materials used in the friction test [12]. Much of the study in this thesis uses silicon wafers on account of their high flatness and nanoscale roughness, but also because Si is easy to structure using conventional lithography and etching. Materials generally undergo a friction interaction which is generally characterised by a critical point where the tangential force assumes a maximum value, resulting in a static peak (static friction) [23]. After experiencing static friction, the tangential force generally relaxes to a steady force, known as sliding friction [12]. The transition from stick to slip can be gradual or sudden depending on the properties of the chosen materials.

The sliding stages can be categorised into three stages: full stick, partial slip and gross sliding. In the partial slip stage, a majority of the surface asperities of the contacting objects are stuck, whereas some asperities are locally slipping [24]. As the tangential force increases, more asperities transition from stick to slip [2, 25]. This increase continues until the tangential force overcomes the static friction of the object [2, 25]. At this point, the friction mechanism transfers from the partial slip to the full sliding (or gross slip) stage [24].

The point that marks the transition from stick to slip/full sliding is known as the static friction peak, which is a significant feature of sliding friction. The peak is not always observed in sliding friction tests. The existence of the peak depends on the dynamics of the transition from stick to full slip. The transition occurs when the applied shear force exceeds the static friction of the sheared surface marking the onset of sliding [2]. The shear force causes elastic deformation in the junctions [23]. This process continues with the increase of the tangential force until the junctions become plastically deformed [23]. The plastic deformation makes the junctions weaker leading to initiation of sliding [23]. The transition from stick to slip is usually represented by a sudden drop in force. The drop can be mutually caused by a reduction in interface strength and real contact area [23, 26]. This leads to lower friction, giving rise to the difference between static and kinetic friction which forms the static peak.

Normally, static friction is the prime aspect of a friction interaction, as it indicates a surface's ability to resist tangential force. The value of the static friction can be also an indication of surface damage due to wear. This means that a surface that possesses high static friction is more likely to suffer more surface damage and material loss when the tangential force exceeds the maximum resisting force. Controlling such an aspect would ease tailoring the friction behaviour of contacting surfaces. Additionally, static friction can be easily identified in most cases. In contrast, measuring dynamic friction is not a straightforward process, because it is susceptible to surface changes due to wear along

the sliding range [2, 27] and it often fluctuates during sliding. Controlling either static or dynamic friction is relatively difficult, as asperities on real surfaces are generally stochastically distributed [28]. They possess random-distributed peaks and troughs in the micro- and nano-scale [28, 29]. This is a key source of the difficulty in tailoring the friction (i.e. the COF). Despite these difficulties, friction generally obeys the rather simply empirical laws noticed by Amontons [6]:

Amontons concluded the general friction laws into two main findings. The first law states that the friction force *F* is linearly proportional to the normal load *P* pressing the surfaces together:

$$F = \mu P, \tag{1}$$

where the proportionality constant is the COF μ. The second law is expressed as the friction force is normally independent of the nominal contact area. These two laws are widely applicable and highly useful for various contacting surfaces.

These laws can be explained via two elementary relationships. They are based on the real contact area (A_r). A_r is established from the asperity tips of mating surfaces, which is often considerably smaller than the nominal contact area [30-33]. The first elementary relationship says that A_r is roughly linearly proportional to the normal load *P*:

$$A_r = \kappa P, \tag{2}$$

where κ is the proportionality constant. It should be noted that this relationship is solely true if the surfaces are not too smooth nor too rough (i.e. there are random-distributed surface asperities), which is the case for almost all real surfaces [12]. It is important to note that the linear relationship between real contact area and normal load is not always obeyed. Archard [34] deduced that the formula could slightly be modified to generalise this relationship for wider material pairs. The formula is modified by inserting an exponent *n* on the normal load *P*. Value of *n* is the range between *2/3* to *1*, where *n= 1* indicates the linear relationship between A_r and *P*. Hertz's theory suggests that when a single sphere asperity is in contact with a flat surface, the contact is elastic and the exponent *n* equals *2/3* [34]. The second key relationship concerns a force required to overcome shear stress (τ_s) of bonding surfaces (interfacial shear strength). This force is the friction force and is influenced by A_r. This relationship is based on the Bowden and Tabor [13] theory of sliding contacts, where the asperity tips are plastically deformed:

$$F = \tau_s A_r \tag{3}$$

Combining Eqs. (2) and (3) by replacing A_r leads directly to the requirement that the friction force *F* also be linearly proportional to the normal load, thus offering a satisfactory explanation for the first

law of friction (Eq. (1)). The proportionality constants after combining Eqs. (2) and (3) (i.e. κ and τ_s) form the COF. It can be deduced from the previous equations that friction is independent of the nominal contact area for a given surface. Obtaining the COF from this law is only attainable experimentally (i.e. not a material property) [3]. It is dependent on the materials used and experiment conditions applied [3, 35]. As friction is dependent on many factors, it is difficult to control it. However, from Eq. (3), it seems feasible to control friction by controlling A_r. This can be achieved by structuring surfaces (or at least one surface) involved in the friction interaction.

The independence of the COF on the normal load (Amontons law) is generally applicable to most surfaces that experience plastic deformation in their frictional interactions. Here, a question could be raised: what will be the case when a frictional interface only experiences an elastic deformation? It is generally agreed that a frictional interface under elastic conditions does not obey the Amontons law. Surfaces under elastic deformation usually show a decreasing trend in the relationship between the normal load and COF [34, 36]. From the literature, it can be said that asperity deformation is a critical element that can dictate the frictional response. It is generally acknowledged that surface asperities initially deform elastically when the normal load (contact pressure) is low. An increase in the normal load, on the same area, causes the asperities to transit from elastic to plastic deformation mode. Determining the critical point where the transition occurs has been discussed in the literature to help understand the actual mechanism for the transition. Greenwood and Williamson [6] believed that the transition between elastic to plastic modes is not primarily affected by the changes in load. They suggested that the transition is mainly attributed to the plasticity index of the materials. The plasticity index determines the critical load where the transition can occur [6]. The deformation tends to be elastic if the plasticity index is low, approximately less than 0.6, and the load is somehow reasonable [6]. When the asperities are pressed under a sufficiently large load, the asperities cannot withstand the pressure and thus would be plastically deformed. In the case where the materials in contact have a plasticity index higher than 1 (which is the case for most surfaces), plastic deformation can occur at very low loads [6]. It is also important to note that the shape of the asperity affects the deformation mode [6]. Sharper asperities deform plastically earlier than the curved asperity [6]. Archard [34] was also interested in understanding the deformation modes during a friction test. Archard aimed to apply a friction test on materials with low elastic moduli (i.e. the pressure is distributed over a larger area of contact). The experiments were performed using smooth and rough Perspex surfaces to examine the effect of surface finish on the deformation regime. The normal load range of the experiments was from 1 to 100 kg. The results showed a decreasing trend of the COF of the smooth surfaces even with low loads. This was also observed in the rough surfaces when higher loads were applied. At low loads on a rough Perspex surface (less than 3 kg), the COF was lower than the one obtained from the smooth

surface and it was constant (independent of the load) indicating that such surfaces obey the Amontons law. Archard [34] suggested for the smooth surfaces and rough surfaces under high pressure that the contact region can be seen as a single contact region. The real contact area can be close to the apparent area of contact indicating that fewer points are engaged when the load was increased [34]. It can be deduced from Archard's experiments that surface finish is a critical element that determines the deformation mode experienced in friction tests.

The previous findings concerned the quantitative analysis on the macro/micro-scale, but it would be interesting to investigate the transition in the atomic scale. Kim and Suh [37] were able to quantify the critical load that marks the transition. They aimed to estimate the critical load that a single asperity can withstand before it plastically deforms at the atomic level. A model involving a flat and extremely smooth indenter pressing on atoms of the asperity was designed to accomplish the aim. The model is illustrated in Fig. 2. 1. Firstly, the load forces the asperity atoms to distribute themselves to support the load [37]. This situation continues until the atoms transfer to a new stable state even after removing the load [37]. The critical load to cause this new distribution of atoms is estimated to be 1 nN, taking into consideration that the bond energy is assumed to be 1 eV [37]. Loads equal to 1 nN and higher on a single asperity are more likely to cause the permanent deformation of the asperity [37].

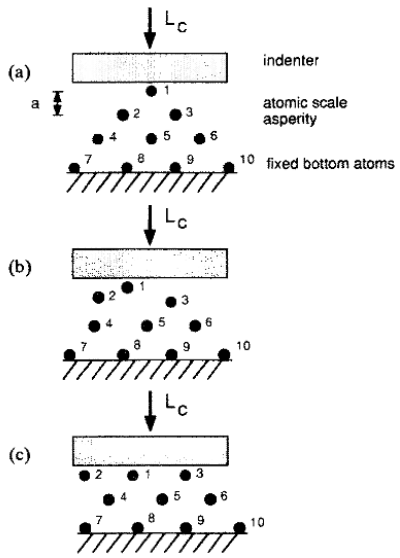

Fig. 2. 1. A schematic to represent the effect of the normal load on the atomic scale between an indenter and asperity atoms of the counter surface: (a) the indenter is being pressed, but still, the load does not transmit to the asperity atoms, (b) the (critical) load is forcing the atoms to re-distribute and (c) the atoms are in their new stable state [37].

2.2. Components of friction and its interactions

Understanding the process behind the frictional response between surfaces experiencing sliding friction is essential to properly analyse the frictional behaviour. Friction interaction is known to be affected by three main factors; namely: adhesion, deformation and ploughing. The resultant friction force is obtained by summation of these three components. Each of these elements has a direct impact on friction but to different extents. For example, the adhesion theory states that similar materials should produce high friction due to the strong bonds between the surfaces [37]. The existence of these components depends on the local state that the frictional interface experiences during sliding [38]. It is believed that the adhesion contribution might have the lowest effect among the other factors on friction [7, 36-38]. Minimising the mechanical factors such as ploughing and deformation would help obtain very low friction which can be regarded as dominant factors. There has been general agreement that adhesion theory, where strong bonds are formed even with no normal load creating a resistive response, cannot explain most of the frictional responses [7, 37, 39]. The friction components have been studied extensively in the literature and here are two representative studies [7, 37] that systematically investigated the contribution of these components. They will be discussed next.

The first study involves tests using two cylinders: one is held stationary and the other is moving [7]. The tests were applied in different scenarios attempting to isolate the friction components to inspect their direct impact on friction. The scenarios are: same materials in contact with each other, hard materials in contact with soft materials and lastly, soft surface pressed against a hard one. From these test conditions, the authors suggested that there are three principal values of COF which are presented in Fig. 2. 2. The first one is the initial friction response to a tangential force which is usually low. The tangential force increases until it overcomes the static friction of the interface resulting in the subsequent value of the COF (static COF). This is usually followed by a slight decrease in the friction response towards a stable COF (kinetic COF). The transition between these values can be categorised into six stages that most frictional interfaces should experience when sliding and is illustrated in Fig. 2. 3. It resulted that there was always an initial coefficient of friction regardless of test conditions and materials tested. The value of the initial COF was always lower than the COF in the subsequent stages throughout sliding. The results also showed that when materials were reversed in their roles (the moving part was stationary and vice versa), there was a pronounced increase in the COF. This indicates that adhesion was not only the factor that impacts friction. The analysis of the six stages is presented as follows. At Stage 1, adhesion and asperity deformation did not play a significant role in the early stage of sliding as mentioned earlier. This was observed for all materials used and experimental conditions. The initial value of COF is followed by a slow increase due to adhesion caused by the

interlocking between the contacting asperities. This stage is not present when the interface is lubricated as adhesion is vanishing in this condition. The adhesion contribution increased leading to a rise in the real contact area (more contacting points were engaged). Additionally, wear particles were produced due to the rise in friction. The combined impact of the adhesion and ploughing caused a steep increase in the COF, representing Stage 3. When the number of wear particles generated in the interface was equal to the number of particles leaving the interface, the COF reached the maximum and the adhesion contribution stabilised at this stage (Stage 4). The saturation of the wear particles was also observed in Ref [40]. After experiencing Stage 4, the interface was either undergoing a decrease in COF or stabilising at the same level at the maximum COF (Stage 5 & Stage 6), reaching the final stage of the frictional interaction. The previous analysis is believed to be seen mostly in contacting materials with a similar hardness which indicates the dependence of the COF on the mechanical properties of the contacting surfaces.

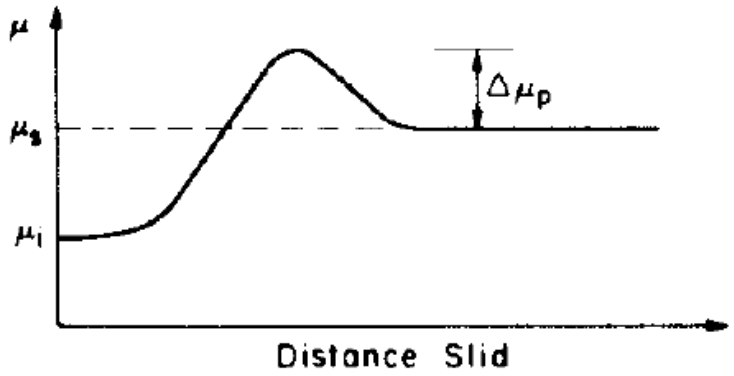

Fig. 2. 2. Typical behaviour of the COF throughout sliding. It begins with an initial value which increases towards the maximum and then drops slightly to the sliding (stable) COF [7].

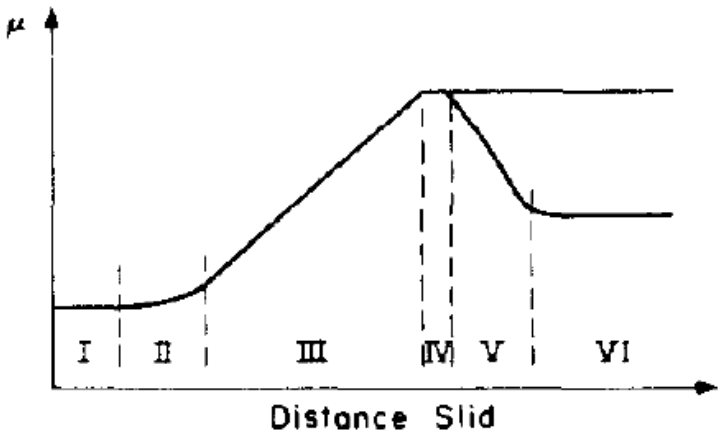

Fig. 2. 3. Representation of the six stages of the COF in a frictional interface [7].

The second systematic study to investigate the friction components was done by Kim and Suh [37]. The work here attempts to exclude the mechanical aspects of friction interaction such as ploughing and plastic asperity deformation by applying low loads. To do so, hard surfaces including silicon, sapphire and silicon carbide (SiC) were used in the tests. These surfaces possess very low roughness around 1 nm. The authors believed that applying a friction test on smooth surfaces helps minimise the effect of deformation. Having hard surfaces is also important to reduce the generation of wear particles and thus reduce ploughing. The tests were applied using a deadweight weighing 5 grams with a sliding speed of 0.3 cm/s. Two test configurations were utilised: pin-on-disk and flat-on-flat using the same tribo-tester. Applying low loads and relatively slow speed allows for neglecting thermal and inertial effects on the frictional response. The main difference between the two test configurations can be seen in the contact stress. It is known that a frictional interface in the pin-on-disk configuration results in higher contact stress than the flat-on-flat due to the small apparent area of contact. Therefore, higher friction is expected from the pin-on-disk test when using the absolute same test parameters because of a higher possibility of suffering from mechanical factors. It is important to note that this assumption is only true when local stresses at the contact junctions do not exceed the failure stress and the effect of adhesion is minimal [37]. The tests using the pin-on-disk configuration were performed mainly on two pairs of surfaces. The first pair involved testing rough hard silicon surfaces with roughness around 1 μm on a hard counterpart surface. The second pair entailed studying soft mica on a hard sphere such as steel. The first set of tests showed a very high COF of around 0.8 which is expected due to the effect of interlocking and deformation [37]. These led to generating more wear particles and ploughing causing the asperity interlocking. The results of the second set showed also a relatively high COF of around 0.55. This is attributed to the ploughing contribution to the soft mica by the steel sphere [37]. These tests using the pin-on-disk arrangement were applied to compare results with the flat-on-flat – which is the main aim. COF values obtained from different tests on the flat-on-flat surfaces showed relatively lower values than the ones obtained from the pin-on-disk which can be said to be a result of the lower contact stress experienced on the flat surface. It was noticed that wear tracks were observed for almost all test specimens, indicating that the mechanical interaction based contribution to friction is significant [37]. It is worth noting that one pair composed of sapphire and silicon did not show clear wear tracks (even when inspecting on optical and electron microscopes) suggesting that the friction force resulted from the interatomic interactions between the surfaces. However, the authors implied that this assumption can be acceptable only if the COF between the sapphire and silicon was far less than the one observed in the existence of wear tracks. Consequently, the authors suggested that the wear tracks should be present even if they cannot be detected by their inspection techniques.

It is useful at this point to discuss the ploughing contribution in more detail. Wear caused by ploughing is mainly due to the mechanical properties of the contacting surfaces. This can be categorised into two cases and is shown in Fig. 2. 4. The first one is when surfaces with similar hardness are pressed together (hard-hard interface). It has been suggested that wear particles can easily penetrate both surfaces causing a rise in friction due to groove formation [7]. The other case is that one of the surfaces possesses higher hardness than its counterpart [7]. At such a condition, there would not be ploughing as wear particles would just slide along the interface [7]. In some cases where a hard surface is slid against a soft one, a mirror finish layer is formed [7]. This decreases frictional force because the wear particles are not anchored (held) anymore on the polished surface and the contribution of deformation is decreased [7]. The impact of wear was also studied via varying radii of a diamond sphere pressed on a SiC surface [36]. The radii of the diamond spheres were 0.3, 0.15 and 0.02 mm. It has been shown that a diamond sphere of a radius of 0.3 mm in contact with SiC results in only elastic deformation [36]. This is supported by the absence of grooves or cracks on the SiC surface when examined in SEM with 10^6 magnification and obtaining a low value of the COF [36]. When diamond spheres with radii of 0.15 and 0.02 mm were pressed on the SiC surface, the COF was not constant, it even increased as the load increased [36]. Grooves and wear tracks were observed with the 0.02 mm sphere with loads higher than 20 grams, indicating that plastic deformation occurred when these loads were applied [36]. Here, the contact pressure is high, particularly for loads of 50 g and higher [36]. For example, the contact pressure at 50 g load equals 2000 kg/mm^2 and reaches its maximum at the centre of the sphere at 3000 kg/mm^2 which is the yield pressure of SiC [36]. With the 0.15 mm radius sphere, smaller grooves were observed only after applying 50 g [36]. This indicates that SiC can deform elastically and plastically when pressed by the 0.15 mm sphere [36]. It is suggested that friction experienced on SiC using the 0.15 and 0.02 mm radii was a result of ploughing and the shearing of the adhesive bonds [36]. The experiments showed that both radii did not experience cracks for loads less than 20 grams [36]. It is believed that the critical load for such an interface might lay around 30 grams [36].

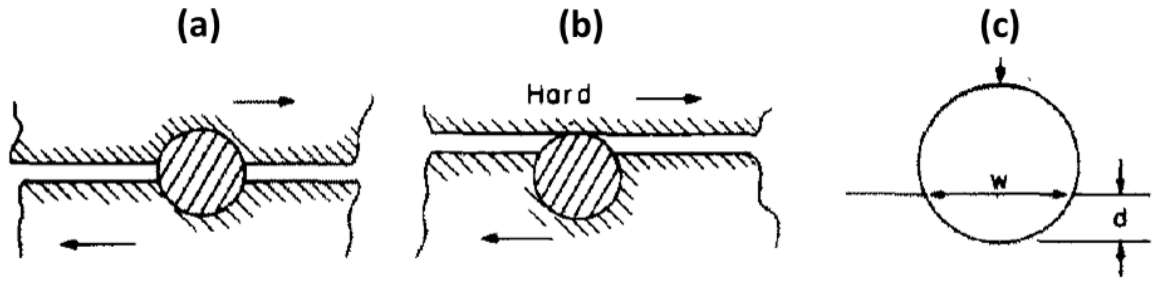

Fig. 2. 4. A wear particle interaction in: (a) hard-hard interface, (b) hard-soft interface and (c) the size of the wear particle [7].

It can be concluded that friction is a result of a combined effect of mechanical interactions and adhesion. The mechanical interactions result from ploughing and asperity deformation which generate heat in the interface. The heat facilitates generation of more wear particles leading to more severe ploughing [38]. The contribution of these components to friction can be summarised in the following. It is suggested that the asperity deformation influences mainly the static COF and has a slight effect on dynamic COF, only if there is a continuous generation of new asperities, but with no effect on the initial COF [7]. As sliding continues, wear particles are generated on the sliding interface causing ploughing. Wear particles in frictional interfaces normally have two possibilities. They might leave the interface or penetrate one of the surfaces [7, 38]. The penetration of the wear particles inside the counterpart surface results in more generation of the wear particles [38]. The ploughing contribution reaches its lowest value when there are no wear particles in the interface or a hard smooth (mirror finish) surface in contact with a soft surface [7]. The impact of ploughing is more pronounced when wear particles on a frictional contact of identical metals penetrate deep inside the other surface [7]. Regarding the adhesion contribution, it almost has no effect on the initial COF and can be neglected due to the presence of third-body layers of contaminants [7]. The absence of the third-body layers causes an increase in the contribution of adhesion to its maximum [7]. The adhesion and ploughing contributions can be reduced by applying liquid lubricant to prevent interlocking and seizure [38]. The number of wear particles can be minimised and also transported away from the interface through the lubricant [38]. However, it is not applicable for applications that experience high temperatures while sliding. The contribution of plastic deformation can be also avoided by ensuring a low contact stress is applied to the interface. High stresses are the main driving force to deform junctions plastically [37].

2.3. Comparative review on friction of ceramics, metals and polymers

It is acknowledged that friction is a materials-dependent interaction. This means that a friction mechanism can differ notably if a contact pair was altered from one material category to another. The

most commonly used materials in friction studies are ceramics, metals and polymers. They differ largely in their mechanical and tribological properties. Ceramics in general have outstanding mechanical properties such as high wear resistance [36]. They, however, suffer from their inherent brittleness [41]. This causes internal and surface flaws during fabrication and machining [41]. Ceramics experience fracture with plastic flow in the surface layers causing changes in the crystal structure such as dislocations, vacancies and stacking faults [42]. The plastic flow in ceramics can be observed under relatively modest conditions of sliding in magnesium oxide, aluminium oxide and silicon carbide [42]. When comparing ceramics to metals, metals are ductile materials and can be easily deformed plastically under lower loads [42]. Dry friction between ceramics is usually lower than metals in the same condition even at high temperatures [36]. In metallic contact, the principal interaction is the formation and then breaking of the metallic junctions [43]. As friction is determined by the direct contact of the surface irregularities, which are pressed by high concentrated pressure resulting in strong welded junctions (strong adhesion; cold-welded) [43, 44]. Due to the high pressure, plastic deformation occurs on the surface irregularities until they can support the load [44]. Metals and ceramics behave similarly under low contact pressure [42]. Both experience elastic deformation under this condition with no presence of grooves or cracking caused by the plastic flow [42]. In the case of exceeding the elastic limit, ceramics (as opposed to metals) undergo gross fracture in addition to plastic deformations [42]. When the metallic interface experiences tangential stress in addition to the normal stress, junction growth becomes more pronounced which is a typical phenomenon in metallic contacts [44]. The situation in polymers is quite different from those in ceramics and metals. It has been suggested that junction growth is small in polymers (i.e. it can be neglected) [44].

Another significant feature of metals affecting the friction interaction is their chemical activity [42, 45]. This is correlated to the d-shells population in the metals' molecular structure [45]. It has been shown that a large d-shells population means that the metal would be less active and this gives rise to a lower COF and vice versa [45]. The reason for that is the presence of strong interfacial bonds formed between the highly active metal and the counter surface [42]. Polymers could be a good alternative to metals in engineering due to their low friction [46]. They could be used as a self-lubricant (i.e. there is less or no need for a lubricant), particularly in the presence of PTFE (fluoropolymer of tetrafluoroethylene) [46, 47]. The low friction in polymers compared to metals can be attributed to the adhesion contribution which is relatively weak when polymers contact metals [46]. Adhesion in polymers arises from Van der Waal's force or hydrogen bonds [46]. They have low shear strength and high yield stress which favours the shearing [46]. Polymers also have high resistance to corrosion which is suitable for a corrosive medium [46]. In polymers, it is expected to observe a single point of contact in high loads where the real contact area approaches the nominal contact area [44]. On the

other hand, the mechanical properties of polymers are quite poor compared to other materials (metal and ceramic) [46]. For example, polymers behave poorly in compression due to their low strength and can be easily worn [46].

The friction of materials is notably affected by the presence of third-body layers such as oxide or contaminant layers which prevent the surfaces from direct contact [42]. The thickness of the inevitable oxide layers on the frictional interface is believed to be around 80 to 100 angstroms [43]. Such layers act as a protective film at light loads [43]. The removal of such layers leads to direct contact between the surfaces, causing increased friction due to adhesion and chemical interactions between the atoms of the contacting surfaces, which is commonly observed in ceramics and metals [42]. The third-body layers are believed to have a strong influence on the contacting surfaces at light loads [43]. In light loads, usually the oxide-on-oxide contact is the predominant interaction and thus friction would be low [43]. An observed increase in the load causes the oxide film to rupture leading to a rise in friction [43]. The presence of the oxide layers in metals can show different behaviours. For example, it was shown that the oxide layer on the silver surface was so thin which was not capable of protecting the metal surfaces from naked contact [43]. Friction in such a condition was fluctuating [43]. When testing aluminium, the oxide layer on aluminium was strong (high hardness) relative to silver and copper surfaces and easily sheared [43]. It was suggested that the high hardness and ease of shearing are the main requirements for the oxide layer to cause low friction [43]. A way to attain clean surfaces by removing the third-body layers and examining the effects of the contaminant is to perform a friction test in a vacuum after heating the surfaces at high temperatures [48, 49]. Surfaces were tested in varied temperature conditions. For a friction test of surfaces cleaned by ordinary methods, the COF could be as low as 0.3 [49]. This value jumped to 6 after prolonged heating at high temperatures above 1000 ^{o}C [49]. Friction was low for a metal-ceramic interface for a temperature of 250 ^{o}C [48]. It rapidly increased when the temperature was in the range from 400 ^{o}C to 800 ^{o}C [48]. The increase in friction was attributed to the increase in adhesion (strong molecular adhesion) and plastic flow [48, 49]. This was associated with the absence of oxide and contaminant layers [48]. If carbon was involved in one of the surfaces structure such as silicon-carbide, the further increase in temperature above 800 ^{o}C led to introduce graphitisation on the silicon-carbide surface which rapidly decreased friction [48]. The oxide layer can also be present after heating when the surfaces were allowed to rest at room temperature in a vacuum resulting in a gradual friction decrease due to the building up of contaminants [49]. To investigate the oxygen presence in a more meaningful way, surfaces were exposed to oxygen, nitrogen and hydrogen [49]. It was shown that imposing oxygen on metallic contacts gave rise to a significant reduction in the COF [49]. The quantity of oxygen needs to be sufficiently large to cause the reduction [49]. Adding hydrogen or nitrogen did not cause any change

in the COF of the vacuum-heated surfaces [49]. It is worth noting that for a gold-on-gold contact, the introduction of oxygen did not lead to a pronounced decrease which was opposed to the other metal pairs [49].

The relationship between the COF and the normal load can exhibit different trends depending on the materials used and the applied pressure. It was found that ceramics and polymers produce a decreasing trend of the COF with the load. For ceramics, it is believed that this is only true under very light normal loads. This was investigated using silicon carbide in contact with a diamond under light loads ranging from 5 to 50 g using a diamond sphere with a radius of 0.3 mm as a top object [36]. The relation between the load and the COF for such an interface showed a decreasing trend which is typical behaviour of a mostly elastic deformation regime [36]. This was supported by the absence of grooves or cracks on the tested silicon carbide surface even at high magnification of the electron microscope [36]. In polymers, the decreasing trend could be observed under a wide range of normal loads due to their elastic nature. It was shown that polymers can exhibit a varied degree of sensitivity with the load [47]. It resulted that the lightly loaded interface showed less sensitivity with the load, meaning that the COF was not varied in that condition [47]. With the continuous increase in the load, the COF became highly sensitive to the load (i.e. the COF was decreasing with the load) [47]. The pressure value that determines the transition from low to high sensitivity was dependent on the material hardness [47]. Softer polymers showed a transition between 25 to 35 MPa, while the harder ones showed a transition at 60 MPa [47]. The degree of sensitivity is believed to be also related to the relationship between the nominal pressure and the yield pressure of the polymer [47]. It was found that for low-yield stress, a fast decrease in the COF was observed [46]. In metals, the relationship between the COF and the load for a wide spectrum of metallic contacts is usually constant (1^{st} friction law). However, there was some deviation from this statement for copper-on-copper or steel-on-copper interfaces where load-dependent COF was observed [43]. Three distinctive normal load regions were experienced depending on a certain load range [43]. Initially, the COF was constant around 0.4 (independent of the load) for a load range from 0.01 to 1 g [43]. A gradual increase in the COF from 0.4 to 1.8 was observed for loads from 1 to 40 g [43]. After 40 g (until 40 kg), the COF was stable again but at a higher value of around 1.8 [43]. The increase in friction was attributed to the engagement of more metallic junctions after the penetration of the oxide layer when the load was increased [43]. Experiments on silver-on-silver and aluminium-on-aluminium as well as steel-on-aluminium showed no dependence of the COF on load even under light loads [43]. The independence of the COF on the load is believed to be attributed to the width of the plastically deformed region (for a pin-on-disc, it is the wear track) and the thickness of the deformed layer [50]. If the multiplication of

these two components is linear with respect to the normal load, then the COF would be constant (independent of the load) [50].

Surface topography is another influential factor in the friction of materials. Experiments were performed in different contact scenarios and varied surface topography to examine the impact of manipulating surface topography on friction. It resulted that varying surface geometrics can give rise to different friction behaviour of contacting surfaces [14, 51]. It was also shown that the orientation of the modified surface (linear grating) relative to the sliding direction and the counter surface (if both surfaces were varied) had a direct impact on the resulting friction [14]. If the surfaces had the same orientation (i.e. the alignment is 0^o between them) and the sliding direction was perpendicular to both surfaces, this rose the COF to higher values than the reference sample (un-modified) and as well the 90^o alignment [14]. This was attributed to interlocking occurring at 0^o alignment unlike the orthogonal alignment [14]. An interesting feature in the reference sample was an observed increase in the COF throughout sliding shown in two slopes unlike the modified surfaces [14]. The different slopes of the increase in the COF of the reference sample were attributed to the inhomogeneous oxide layer on the surface that affected the interfacial shear strength [14]. It was believed that the interfacial shear strength was varied during sliding as the interface was altered due to the oxide layer presence [14]. This was also seen in a study performed by Rabinowicz [52] who found that the interfacial shear strength was indeed altered during sliding. Another way to study the impact of surface topography was to design surfaces with different shapes and texture densities. Two texture shapes including linear and wavy grating were designed with different texture distances ranging from 100 to 400 µm [51]. It was shown that the wavy texture resulted in the lowest COF among the other surfaces [51]. This was more pronounced in 100-µm texture distance [51]. When the texture distance was increased to 400 µm, there was no clear difference between all surfaces [51]. The surfaces with varied surface topography showed an enhanced stress distribution where the stress was distributed uniformly across the contact area [51]. The stress distribution on the reference sample was not uniform and was highly concentrated around the edge of the contact area which caused evident wear scars on these regions [51].

Wear in ceramics and polymers is generally induced by plastic deformation and ploughing due to the dissipation of the friction energy that marks the transition from elastic to plastic deformation regimes. When the normal load is first applied, the surface asperities may experience elastic or plastic deformation [47]. If the local pressure is high and exceeds the plastic flow pressure of the material, plastic deformation occurs [47]. As soon as the tangential load is applied, the interface experiences normal and tangential stresses which would facilitate the plastic deformation due to shearing the asperities [47]. Generally, in polymers, a transfer film is observed particularly in an interface involving

PTFE [53]. The transfer film observed in PTFE when contacting metals (or hard surfaces) is useful in reducing wear in the interface as the transfer film can act as a lubricant [53]. Wear in ceramics is mainly affected by plastic flow, cleavage (of certain structure orientation) and fracture [36, 41]. At ambient temperature, brittle interactions such as cracking or pull-out of grains in ceramics are likely to strongly influence the wear rate [41]. Wear in ceramics (some concepts can be also applied to polymers) can be categorised into two principal terms which are adhesive wear and abrasive wear [42]. The adhesive wear is related to the adhesion between two ceramics into contact or ceramic-metal interface [42]. For the adhesion-induced wear to occur, the fracture strength of one surface must be less than the interfacial fracture strength [42]. If the interfacial fracture (bonding) strength is less than the two surfaces in contact, the fracture occurs with no wear (theoretically suggested) [42]. Once high pressure is applied, local pressure regions are developed causing fracture of cohesive bonds. In the case of a ceramic-metal interface, a metal transfer is likely to occur due to the strong adhesive bonds in the interface which are much larger than the cohesive bonds of the metal [42]. The abrasive wear occurs when the hardness of contacting surfaces is significantly different (e.g. one surface is much harder than the other one) [42]. Such a wear condition was also observed when hard particles of the third body were entrapped in the interface that were harder than one or both of the contacting surfaces [42]. The existence of the wear particles in the interface can cause abrasion and ploughing due to their interactions in the sliding contacts [54]. They also can act as load-carrying elements which reduces the wear rate [54].

Friction and wear of ceramics are strongly affected by the sliding speed of the sliding contacts. It was shown that high sliding speed favours the reduction of the wear rate, but at the expense of increasing the COF [41, 54]. A wide range of sliding speeds was applied in Denape and Lamon's study [54] to inspect the speed effect on the tribological behaviour of ceramics. The wear rate was initially decreased with a sliding speed towards a minimum rate then started to rapidly increase after a critical sliding speed of 0.5 m/s [54]. In contrast, the COF was initially increasing until the critical speed towards a maximum COF then started to decrease [54]. It was noticed that among the tested ceramics, sintered silicon carbide exhibited a relatively constant COF and wear rate (unaffected by the sliding speed) and these values were the lowest among the remaining ceramics [54]. The dynamics of the tribological interactions can be briefly discussed in the following. The low-speed condition (below the critical value) caused the accumulation of wear debris [54]. This debris increased the COF due to ploughing but decreased the wear rate [54]. The decrease in the wear rate was believed to be the result of the load-carrying effect of the wear particles, reducing the wear effect caused by the contact pressure [54]. Exceeding the critical speed led to eliminating the wear debris from the interface causing a reduction to the load-carrying effect, thus more wear particles were generated [54].

2.4. Measurement of friction

Experiments on measuring friction generally involve either a pin-on-disk configuration (rotation motion) or reciprocating sliding (linear) or unidirectional sliding. They all were useful tests depending on the specific application. Choosing a certain method is normally dependent on the test objectives and the facilities available. The first two methods are commonly implemented in friction experiments because they can be used to acquire friction and wear results via a single test. They have been also employed in many commercial tribometers which widens their applicability. However, a smaller number of studies have investigated friction by unidirectional sliding. This might be because it is restricted to very limited sliding displacement. Nevertheless, it provides vital information for materials properties concerning friction and stiffness of materials. Friction experiments are usually associated with elements that should be carefully assigned to obtain successful results. They are mainly related to ways of applying tangential force (movement), normal load, and measuring these forces. In the following, a brief literature review of these three elements will be presented.

2.4.1. Tangential movement

Applying tangential movement was mostly achieved in the literature by a motorised actuator. Utilising an actuator to cause a linear motion differs from one study to another. It can be used to move a lower-, upper-surface or specimen between the surfaces while performing a friction test. For example, Mulvihill *et al*. [55] used actuators to move a carbon fibre tow between two glass surfaces. The glass surfaces are held stationary, while the tow is pulled by the actuator. Friction force in this arrangement is measured from the double contact between the two surfaces and the fibre. However, moving a specimen between two surfaces might cause a little complication in the system as there are two friction interfaces between the specimen and the two surfaces. The contribution of each interface to the resultant friction might not be known precisely. Therefore, studies in the literature are more directed to measuring friction from a single contact by moving one surface relative to the other.

Contrary to the motion caused by a motorised actuator, tangential movement can be initiated by mechanical action. Bowden and Leben [56] utilised water pressure to initiate a linear movement resulting in friction between two surfaces. This method seems to be a conventional way to perform sliding, but it was relatively as effective as the motorised actuator. In the experiment of Bowden and Leben, water pressure was employed to apply tangential motion to a lower surface mounting on a carriage. The carriage is attached to parallel rails. This movement enables the two surfaces to be in contact initiating tangential force. The mechanism of the tangential movement was achieved by filling water in a cylinder that contains needle valves to control water flow through the cylinder. The cylinder

contains pistons moving at a steady rate to ensure a steady movement of the lower surface. Fig. 2. 5 illustrates a diagram of the apparatus used in the Bowden and Leben study.

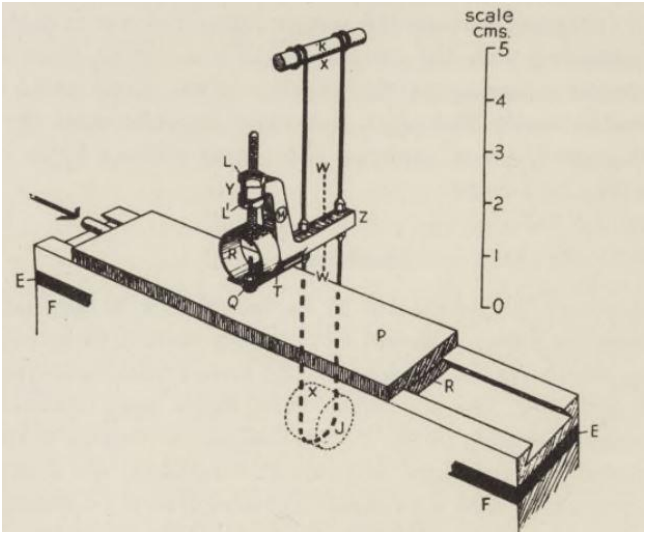

Fig. 2. 5. Illustration of the friction apparatus. key components: Q- upper surface (spherical slider), YZ- Duralumin arm, XX- Bifilar suspension, P- bottom surface, R- circular spring to apply the load, J- pulley, K- axle [56].

2.4.2. Application of normal load

Exerting normal load on a friction interface can be done in various ways. When applying the load, it is important that it can be controlled and unaffected by surface irregularities. One way to achieve this is by Implementing piezo-actuation on an upper surface to eliminate the effects of the irregularities on the load [14, 57]. It can be applied for example by dead weights [58], compression springs [55] and pneumatic cylinders [59]. Dead weights are commonly used in sliding contact experiments. The method is usually implemented with a pulley to help maintain the load. To obtain a more flexible load range, compression springs and pneumatic cylinders are utilised. In the former [55], the load is applied by compressing the springs with nuts. The springs are positioned in the top corners of the contact interface. The load is then measured by a load cell connected to a computer interface for accurate measurement. In this method, the contribution of individual springs should be equal over the interface to ensure better interface alignment. The pneumatic cylinders [59] permit utilising gas or pressurised air to produce force. The cylinder is attached to a load cell and can vary the load between 1 to 100 N. The resulting signal is proportional to an applied force. The signal is then amplified to be measured by a computer interface. The load is transmitted through a lever arm pivoted on ball bearings. This mechanism allows controlling the value of the load without any effect from deflections of a sample or sample holder. The performed method is shown in Fig. 2. 6. The load can be fixed or varied during a

sliding test. The fixed load is needed to inspect the effect of sliding distance or speed on friction [58], whereas the varied load is required to observe how friction changes with load.

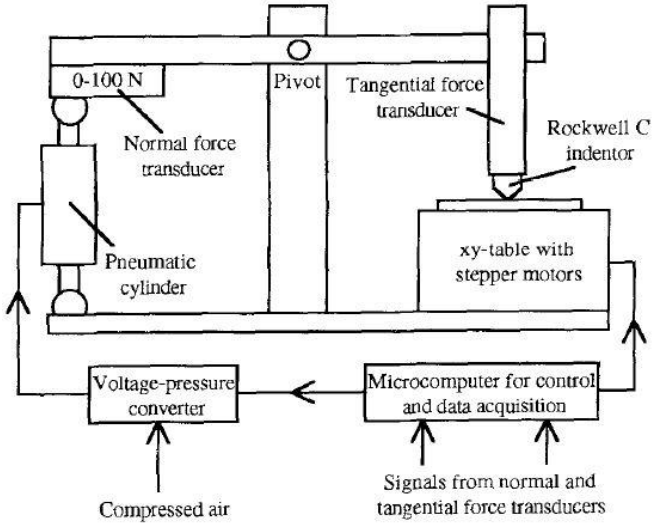

Fig. 2. 6. Utilisation of a pneumatic cylinder for applying normal load on a specimen [59].

2.4.3. Measurement of friction force and contact area

Even though it is known that employing load cells for measuring forces provides accurate results, there are non-load-cell methods that allow for obtaining accurate measurements. For example, Bowden and Leben [56] implemented a torsion arm attached to a lower surface to measure friction force. Once there is tangential force, the arm is deflected which is an indication of a force between two contacting surfaces. Measuring the deflection was carried out by the reflection of a light beam through a mirror passing via a horizontal slit in a camera. Another method to use the deflection of an object to measure friction force was applied by Gachot [57]. The study used the deflection of a spring in the horizontal axis to measure the tangential force. The spring has a tangential stiffness of 1.1447 mN/µm. The deflection is measured by optical displacement sensors. This method employs a fibre-optical sensor to measure the deflection of an elastic arm connected to a contact zone. In addition to these two studies, Kang et al. [15] utilised deflection of bi-axial leaf flexures (see Fig. 2. 7). The magnitude of the deflection is calculated by measuring the displacement of the flexures in the presence of the force by knowing the stiffness of the leaf flexures. To monitor the normal load throughout sliding, a precise load cell was inserted underneath the sample and above the mounting stage. The leaf fixtures were made from aluminium alloy that has an elastic modulus of 71.7 GPa. The PDMS half-sphere was first aligned with the opposing surface. As soon as the PDMS touches the surface, a deflection in the normal direction occurs, ensuring contact. Then, sliding is taking place causing the rigid members, which hold the hemispherical PDMS, to deform. The defection is measured by a laser displacement meter.

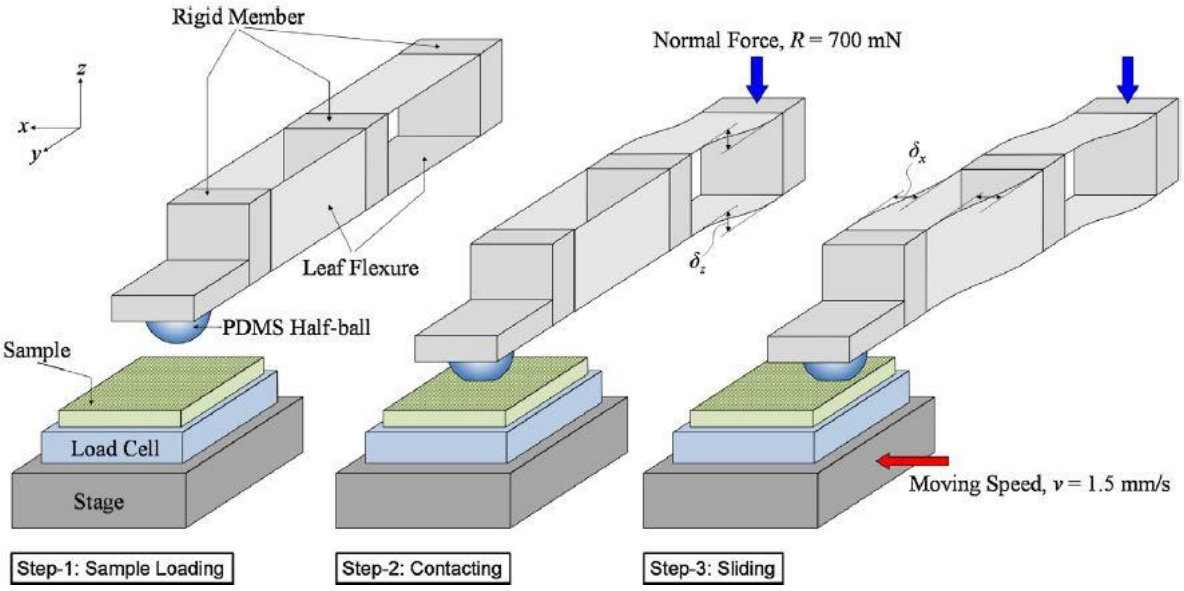

Fig. 2. 7. Schematic diagram of deflections on vertical and horizontal axes occurring on the leaf flexures [15].

It is acknowledged that friction force is directly proportional to the real contact area (A_r). Therefore, it is vital to implement techniques that permit measuring the real contact area. This allows tailoring friction force to attain control over the frictional behaviour of contacting surfaces. Measuring A_r in friction tests can be carried out by using optical techniques. This typically requires transparent surfaces to permit the passing of light through the contact zone, which does limit the applicability of the optical techniques in the real contact area measurements. An early example of using light reflection to measure the true contact area was achieved by Archard [34]. An illustration of the procedure is shown in Fig. 2. 8. The experimental setup to measure the contact area involved a Perspex truncated prism as a lower flat surface (labelled as "B" in the figure) pressed by an upper Perspex surface (A) fixed to a holder (C) through a rubber sheet (D) to optimise the conformity when the load was applied. The procedure began with illuminating the side-face of the prism via a mercury lamp. The light entering the prism ideally should be totally reflected from the other side of the prism. If there was no intimate contact between the flat surface of the truncated prism and its counterpart, the light passed the Perspex surface and would be totally reflected. The areas where there were intimate contacts between the surfaces did not allow the light to pass and were shown as dark spots. The size and number of these spots were determined by the load. Higher normal loads resulted in more dark spots and some of them with larger sizes as illustrated in Fig. 2. 9

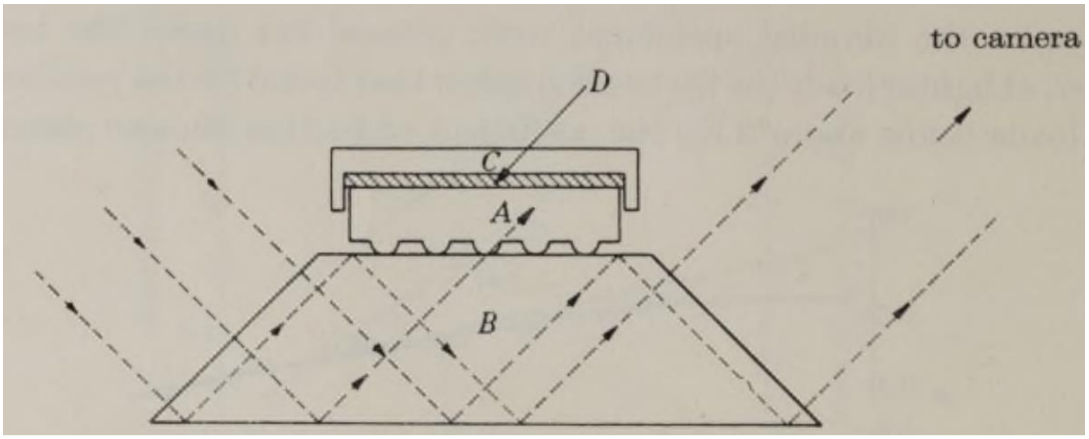

Fig. 2. 8. Measurement of the real contact area carried out by light reflection on a Perspex truncated prism as a lower surface (B) in contact with a Perspex surface (A) that is fixed to a holder (D) through a rubber sheet (C) [34].

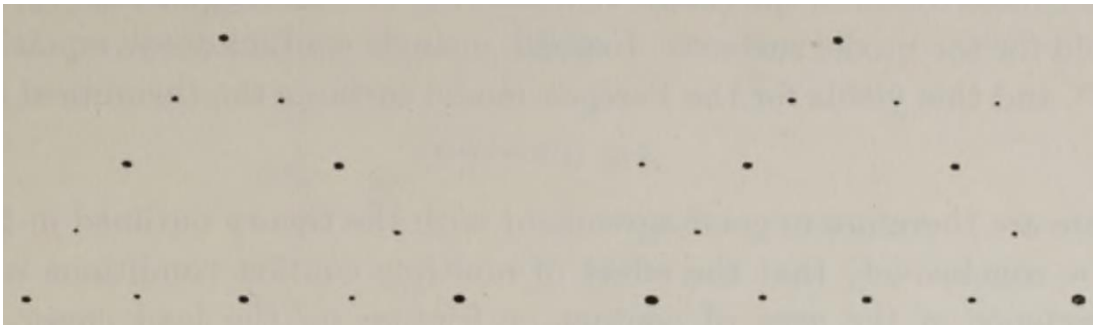

Fig. 2. 9. Optical image of the reflected light through the truncated prism. The dark spots are the points of contact (destructive interference). The size and number of these spots can be related to the applied contact pressure [34].

Another (relatively) recent attempt to utilise the light reflection was carried out by Ovcharenko *et al* [60]. This study used a light beam emitting towards a contact zone. The light reflected when it touched an asperity peak that was not in contact with the counter body (air gaps). Light reflection formed Newton's rings, where the centre of the rings corresponded to the real area of contact. The area was then measured by using image processing algorithms. Despite the requirement of transparent surfaces to measure A_r by optical techniques, Mulvihill *et al*. [55] managed to measure A_r of opaque material with an optical microscope. Their technique involved coating a glass plate positioned on top of a carbon fibre tow containing filaments used for conducting the test. The coating was composed of a base layer of 8 nm thick of chromium and a thickness of 140 nm of silica as an outer layer. The filaments produced colour when they touched the glass plate and this was seen through a microscope. This method was optimised with regard to image contrast to distinguish the non-contacting filaments from other parts that might touch the plate. A similar approach was implemented by Weber *et al.* [26]

using pressure-sensitive film coated on glass surfaces in contact with a polystyrene sphere. The study aimed to investigate the growth of the real contact area during the three stages of sliding.

2.5. Surface texturing

2.5.1. Introduction

Surface texturing is considered an important aspect of materials engineering. It has been implemented in different applications, such as magnetic storage and MEMS [17]. It is used to achieve certain purposes, concerning altering surface characteristics [61]. For example, the soles of laborers' shoes have been textured to facilitate the movement of laborers on mouldy grounds [61]. Texturing surfaces in tribology can be defined as changing the surface topography of materials to improve their tribological properties [29]. The structures are in a form of organised (uniform) features with controlled geometry [29]. This technique has been widely studied in terms of improving the tribological properties of materials.

Topographical modifications have led to promising advances in micro and nano-scale structures [9]. The modifications permit improving friction interactions between contacting surfaces [17, 62, 63]. It has resulted that modifying surfaces by texturing showed lower friction than un-modified ones [9, 17, 38, 63]. However, it should be emphasised that friction is a function of multiple parameters that influence the overall friction (i.e. contributions from adhesion, ploughing and deformation) [38]. For instance, structured surfaces can help reduce the effects of adhesion, but there are still other parameters that should be managed [38]. The impact of surface texturing will be discussed in detail later in this chapter. Before investigating surface texturing, it is worth providing a basic history of how and when texturing began to be important in engineering applications.

2.5.2. Early stage of surface texturing

Structuring surfaces rose in importance with the basic idea being explored more than a century ago in the United States [64]. The idea was to texture surfaces to allow better rotation of a bearing without unnecessary friction [64]. This mechanism enables feeding the bearing with adequate lubrication facilitating the rotation movement [64]. Later in 1917, German researchers improved the idea by producing depressions on surfaces to improve the tribological properties of surfaces [64]. The idea of texturing surfaces continued to develop due to the need to overcome obstacles encountering contacting objects, especially those in engines [64]. Such objects experience high temperatures that lead to severe scuffing (surface damage) due to lubrication shortage [64]. Textured surfaces have succeeded in minimising the effect of lubrication shortage between parts of diesel engines; thus, it proved possible to reduce friction between the engine parts by structuring their surfaces [64].

In addition to the previous achievement, another early industrial attempt to produce structured surfaces was achieved by Schneider in 1984 [65]. The manufactured surfaces were made by a technique called vibro-rolling [65]. Use of this method was successful in reducing surface damage to materials that are susceptible to scratching and seizure [65]. This was more pronounced on contacts under the early sliding friction regime, where materials have high resistance to movement [65]. These successful attempts paved the way to create more robust techniques to further improve the quality of the textured surfaces.

2.5.3. Novel techniques for texturing

Texturing techniques have developed dramatically since the nanotechnology revolution begun. Nanotechnology has entered the competition of producing cost-effective structured surfaces. It can provide good topography control for a textured surface [61]. It also enables obtaining a good analysis of lithography-fabricated structures by employing white light interferometry [61]. This interferometry technique uses a broadband light source emitting towards a target surface to measure height variation [66]. This is then compared to a mirror-like object inside the apparatus promoting an accurate analysis of surface topography to effectively examine fabricated surfaces [66]. The significance of such a non-contact profiler is that it can provide sub-nanometre vertical resolution, providing high resolution with less probability of surface damage [67].

Multiple techniques have been used in the literature to modify surface topography. They are mainly laser surface texturing (LST) [14, 51, 68-71], photolithographic etching [72-76], crystallisation [77, 78] and micro-cutting [79]. It is important before implementing a texturing technique to consider the availability of a suitable facility that allows producing and characterising surfaces, while at the same time, having good control over the parameters of the final surface. It is also significant to take the cost associated with a chosen technique into account. Among these techniques, LST and photolithographic etching are the most common techniques to produce structured surfaces. These two lithographic techniques have shown their capability to produce repeatable and good-fidelity structures. The features of these two techniques will be discussed in the following.

The first technique to discuss is Laser surface texturing (LST). It is an approach that is widely implemented to structure surfaces for friction tests. It uses laser interference to create micro/nanostructures [14]. These structures are generally formed by splitting a primary laser beam into two secondary beams that are then interfered with [14]. Formation of the structures is achieved by inducing a surface tension gradient by a temperature gradient between maximum and minimum laser intensity [62]. Following this, surface topography is formed as isolated lines with micro/nano dimensions by the projected sinusoidal waves [14]. By this technique, re-solidification, intermetallic

phases and melting can be induced [14]. Even though LST is a promising technique for tailoring surfaces, it introduces residual stresses and microcracks during the melting/re-melting process [61, 74]. Surfaces made by LST might give rise to severe abrasive wear on a counter interface caused by molten particles ejected during the feature formation [29]. The molten particles cause wear because they are re-solidified on the minimum laser intensity positions, causing surface imperfection [29]. However, a technique called direct laser interference patterning (DLIP) can be used to reduce the effects of these issues [61]. It also can produce complex structures [61, 80]. However, it should be noted that the productivity of LST is low due to a slow process of texturing [61].

Another technique for producing textured surfaces is photolithography. It can be referred to as photochemical texturing (PCT). Patterning surfaces by photolithography is done by exposing the surfaces to ultraviolet (UV) light passing through a mask [29, 61]. The mask contains an intended pattern which is transferred onto a sacrificial layer (photo-resist) [29]. It is then followed by chemical etching to obtain the patterned structure [29]. Fabricating structures by photolithography necessitates carrying-out experiments in a clean room facility illuminated by yellow light [29]. This is because the photoresist is highly sensitive to white light – or any other coloured light – affecting its characteristic before it is even exposed to UV light [29]. PCT is preferable for practical tests in laboratories, as they are versatile [29, 61, 74] and flexible [61]. Additionally, it provides good resolution for a patterned surface with a reasonably short time for patterning, particularly for a large area of texturing [29]. This is because patterning is normally independent of the area of texturing which is opposed to LST [29].

2.5.4. Influential factors

It has been shown that the effectiveness of surfaces designed by texturing techniques has been influenced by several factors related to experimental conditions, shape design and materials used. There are also other factors that should not be ignored which are surface chemistry and microstructure of contacting materials [61].

Considering the experimental condition (including texture design), it is regarded as an important aspect that directly impacts the outcomes of friction tests. Here, two factors of the experimental procedure will be discussed. The first is related to a contact arrangement between the counter bodies. It has been shown that the feature orientation of the structured surfaces relative to the sliding direction is a critical factor. Yu *et al.* [81] have found that performing sliding perpendicular to the feature orientation resulted in higher friction than the parallel direction. They claim that this is only true if the load was sufficiently low with narrow grooves [81]. The shape design of the structured interfaces is a crucial element of a friction study. The parameters of the pattern design should be

carefully chosen. It was observed that COF for textured samples was higher by 20% than untextured ones with a spacing of 100 µm [82]. This percentage decreased to 9.4% when the spacing was increased to 250 µm [82]. This means that reducing pattern density leads to lower friction in the interface, which might be attributed to the less real contact area. However, these findings contradict Xing *et al.* [51] and Wang *et al.* [8] with respect to an observed decrease in the friction force of textured samples when small spacings were patterned. Even though there is disagreement between these studies regarding the effect of spacing, they all agree that the pattern density has a direct effect on the friction results.

The effectiveness of surface texture can also be impacted by a factor related to materials used in the friction tests, specifically for dry friction. Surface texturing in a study performed by Kang *et al.* [15] resulted in higher friction which contradicts many studies in the literature. They performed a friction test by a material pair containing an aluminium flat surface with micro domes against a hemisphere of PDMS. The PDMS is known as a soft material, opposing the aluminium surface. The aluminium is likely to penetrate through the PDMS surface requiring more force to overcome the interlocking. The increase in friction on the structured surfaces was not observed when the contacting pair contain the same material. This was seen in a study performed by Gachot *et al.* [14], comprising two steel surfaces. Such a pair resulted in a reduction in friction for the structured interfaces compared to the unstructured ones. Perris et al. [83] successfully demonstrated that it was possible to tailor structured interfaces (with an adjustable squarewave topography) to have particular design values of normal contact stiffness. They performed the tests on structured polymer surfaces produced via injection moulding using novel flexible mould inserts produced by nanoimprinting from a structured silicon master (as outlined in Hamilton et al. [84]). Likewise, Hamilton et al. [85, 86] deployed the same squarewave structures in boosting the strength and toughness of adhesively bonded polymer interfaces via mechanical interlocking of the adherands. In a sense, the present work aims to achieve similar advantageous possibilities for friction in Chapter 4.

Having succeeded to select the suitable parameters for structuring surfaces, it is reasonable to ask whether we can control key drivers of friction which are adhesion and ploughing. These two factors are affected by real contact area and wear particles, respectively. In theory, structuring surfaces might allow control of the adhesion contribution to friction by altering contact area [38, 80]. Ploughing is adjusted by trapping wear particles in the structured features (trenches), reducing its contribution to friction [8, 82].

Surface texturing is advantageous in the two typical conditions of friction experiments which are lubrication and dry friction, aiming to control the key factors of friction. Regarding lubrication,

textured features provide a micro-reservoir for lubricant applied, enhancing the lubrication mechanism [15, 17]. The textured features are particularly beneficial when lubrication becomes ineffective (boundary lubrication) [38]. In terms of dry friction, surface texturing enhances the frictional behaviour of contacting surfaces by trapping wear particles [63, 80]. The existence of these particles increases the friction force between contacting objects [7]. Trapping wear particles (debris) is achieved by accumulating these particles in surface depressions (textured structure) [38]. Removing these objects from the contact zone reduces wear between the two surfaces, thus reducing friction [38]. To achieve the trapping mechanism, it is necessary to structure the interfaces with certain parameters [38]. These parameters are illustrated in Fig. 2. 10. Firstly, the length of a feature of a structured surface (L) and a gap between any two features (g) should be in a close approximation to prevent ploughing – i.e. their ratio should not be much less than 1. Secondly, the ratio of length and height of a feature should not also be less than 1. This reduces the chances of plastic deformation [38]. Additionally, it is important to design the features in which wear particles with different sizes can be entrapped.

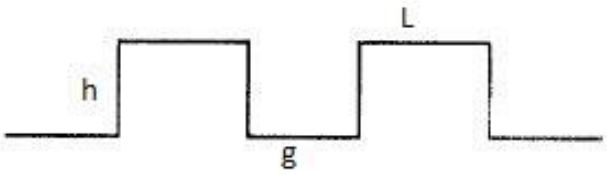

Fig. 2. 10. The parameters that affect the trapping mechanism [38].

Surface texturing has shown its importance in investigating the tribological behaviour of contacting surfaces. Previous studies have investigated metals and polymers in order to inspect the feasibility of controlling friction by structuring their surfaces to explore their applicability in industry. It would be favourable to study the effect of surface texture on the frictional behaviour of idealised materials to obtain a desirable understanding. The photolithography technique was chosen in this study due to its flexibility and capability of producing high-fidelity near idealised features. The structured features were patterned on silicon samples possessing high flatness and nanoscale roughness. Such a material condition allows for studying the frictional behaviour of the structured surfaces without interference from other factors.

2.6. Friction in reciprocating sliding

Studying the frictional behaviour of materials via reciprocating sliding is a significant aspect of assessing materials' resistance to damage. Typically, thousands of cycles are required to allow for assessing materials' endurance to severe loading. The damage occurs due to experiencing repeated sliding over the same areas. This means that the friction features of tested materials are affected by

the history of sliding. The history-dependent sliding is generally similar to unidirectional sliding in terms of elements of sliding (pre-sliding, stick and gross slip). Each cycle of the friction hysteresis loop composes of forward and backward sliding. The difference between them forms an area during cycling. The area corresponds to the energy consumed (energy dissipation) during sliding that can be consumed in different forms such as in the plastic deformation, sound or heat (see Fig. 2. 11) [27]. Observing the geometric characteristics of the loops, (i.e. width and shape etc.) in a friction test can help identify fretting regimes [87, 88]. Normally, the hysteresis loops can be in the shape of an elliptical or approximate parallelogram. The elliptical-shaped loop indicates that the test condition is under fretting fatigue (partial slip), whereas the semi-parallelogram shape is an indication of the fretting wear regime (associated with gross sliding) [27, 87]. The impact of fretting is illustrated in a simple schematic in Fig. 2. 12 to show how the surfaces are affected. The figure shows the material loss that increases with sliding cycles. It has been suggested that when surfaces experience overstraining, it results in wear formation (fretting wear), whereas crack generation (fretting fatigue) is initiated in the event of undergoing overstressing [89]. One practical example of an application that experiences the fretting regime is wind turbines [89]. The contact between the turbines and blades undergoes different forms of displacement amplitudes [89]. Therefore, wind turbines are more likely to suffer crack nucleation and wear formation.

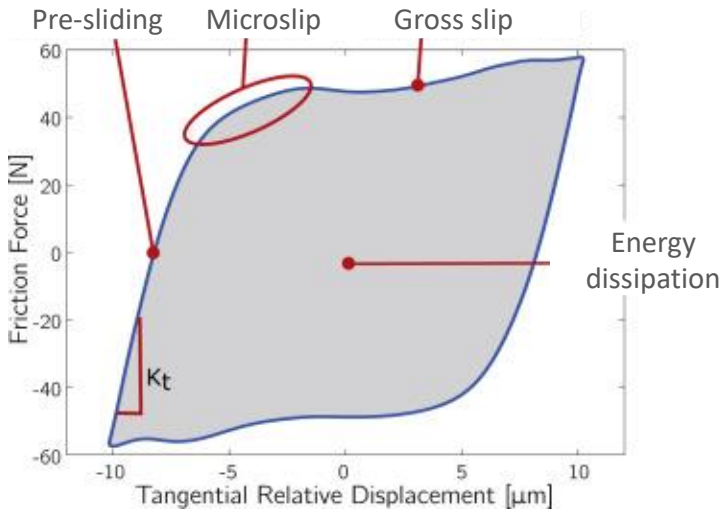

Fig. 2. 11. A typical frictional hysteresis loop from a reciprocating sliding test. K_t is tangential stiffness (adapted from [90]).

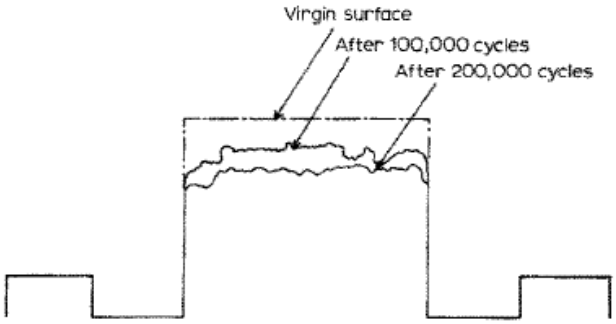

Fig. 2. 12. The impact of wear caused by the reciprocating sliding is sketched to showcase how the surfaces are affected by sliding cycles [91].

The elements of sliding, namely pre-sliding (partial slip) and gross slip, in hysteresis loops are considered the main factors that lead to causing fretting fatigue and fretting wear [92]. Experiencing such fretting types in reciprocating sliding is mainly dependent on the tangential displacement amplitude [90]. Fretting fatigue occurs when the displacement amplitude is small enough [92]. This is observed in the partial slip region, where most of the contacting points are stuck [92]. This fretting regime leads to crack generation at the interface [90]. When the displacement amplitude is larger, the fretting regime transits to fretting wear where most of the contacting points are in the gross slip region [92]. In fretting wear, normally large debris comes out from the interface resulting from material loss [27].

Studies in the literature attempted to characterise the fretting regimes and determine the boundaries where the sliding condition transits from one phase to the other. It was shown that the transition from the partial slip regime to the gross slip interaction can happen at a displacement amplitude as small as 15 µm [93]. In some cases, the partial/mixed stick-slip can continue up to a displacement amplitude of 70 µm [91]. It is suggested that the displacement boundaries that determine the fretting regimes are affected by the normal load (i.e. the load can shift the critical displacement) [91]. The former value (15 µm) was obtained from loads up to 50 N, whereas the latter (70 µm) resulted from loads reaching 147 N. It can be said that the experimental conditions (normal load, contacting materials, contact arrangement etc.) are important in determining the critical displacement amplitude. It is known that the increase in the slip amplitude adjusts the fretting regime. This can be utilised to prevent fretting fatigue from occurring, but this would be at the expense of obtaining more wear particles causing grooves on the surface [93]. The effect of the slip displacement amplitudes on loop shape is schematically presented in Fig. 2. 13. The interactions observed in the fretting tests differ from one phase to the other and are discussed in the following according to a few experimental studies in the literature.

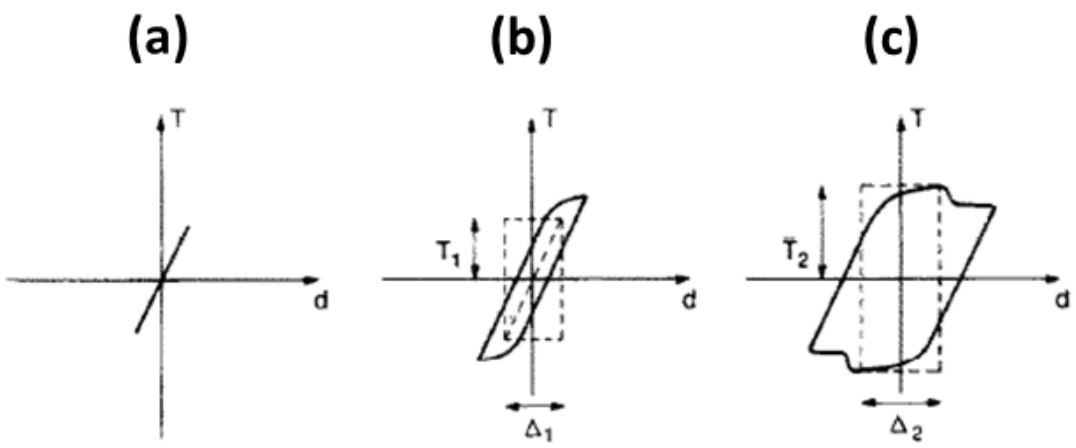

Fig. 2. 13. The friction hysteresis loops are characterised into three main stages: (a) partial slip, (b) mixed stick-slip, and (c) gross slip [91].

At a low displacement amplitude (Fig. 2. 13 (a)), a linear relationship between the force and displacement is seen for a displacement amplitude of 2 µm [93]. The fretting loop here is only a straight line. The surfaces in such a fretting regime are contacting in multiple points [93]. No damage is observed during this small slip amplitude. The linear relationship indicates that the interactions were elastic with the surface asperities deforming only elastically [89, 93]. It is suggested that surfaces in this fretting regime suffer only from mild deformation and the main action is the scratching of the oxide layer [91]. The repeated sliding in this fretting regime is believed to be the cause for the nucleation and propagation of fatigue cracks and this reduces the fatigue life of the fretted surfaces [89, 91, 93], but this was not observed in an experimental study performed by Vingsbo [93] after 10^6 cycles. This suggests that the number of cycles (in addition to other experimental conditions) might be insufficient to cause the cracks.

When the displacement amplitude increases a little more, the fretting regime transits to the mixed stick-slip phase. The width of the loop becomes slightly wider than the first case (see Fig. 2. 13 (b)). In this stage, fretting wear scars start to appear on the surface [93]. The existence of the wear scars is an indication of the transition from elastic to plastic deformation where the contact asperities are sheared [93]. The wear scars observed in this stage were surrounded by areas (i.e. the rim of the wear scar) suffering from cracks [93]. The wear particles generated in the interaction are trapped in the interface and with the continued application of the contact pressure, the wear particles will be crushed into small fragments causing grooves [93]. This process continues until the particles leave the interface [93].

A further increase in the slip amplitude results in the transition to the third stage where the loops are very wide forming an approximate parallelogram shape (Fig. 2. 13 (c)). Tests performed by Vingsbo

[93] showed a decrease in the tangential force around the end of the stroke. This is believed to be attributed to the transition from static to kinetic friction stages in which all contacting asperities junctions became broken [93]. This decrease in the tangential force was also observed in certain displacement amplitudes of friction tests carried out by Mulvihill *et al* [94]. The decrease was seen after increasing the displacement amplitude from 1 mm to 1.6 mm, exposing new areas to frictional interaction. This sudden drop occurred when the moving surface was slid against unworn fresh areas. This is because the moving surface did not encounter obstruction (debris) in the intact areas while it was slid resulting in a lower tangential force. Once the fresh areas experienced wear, the loops exhibited the usual behaviour observed in the gross slip stage in the fretting tests. Surfaces under the gross-slip stage are extremely damaged with considerable rough finish and grooves [91]. Numerous grooves with widths corresponding to the particle size of the wear debris (around 2 to 3 μm) are usually observed [91]. The wear impact is more pronounced at the edges of the interface [91]. As most surfaces are tested in air, the interactions in the gross-slip phase (wear formation and grooves) can be escalated by the oxidation process on the particles [91, 93]. The enclosed area seen in the mixed stick-slip and gross slip phases mainly represents the energy consumed (friction energy) to flatten the asperities and generate wear particles. In the gross slip, the area continues to increase as there is a need to shear the junctions which leads to generating wear particles [89]. The friction energy is also required to eliminate the wear particles from the interface [89]. When the plastic deformations are no longer required, the friction energy becomes constant [89, 91]. This means that no more generation of wear particles occurs. The fretting regime transits to the reciprocating sliding where the loops are closer to a square shape. The reciprocating sliding can be seen in a slip amplitude as low as 300 μm [91].

Wear formed throughout sliding in the gross slip regime causes an increase in the tangential force due to the accumulation of wear debris, which is more evident in later cycles [94, 95]. This increase continues until it reaches a peak value at the end of the sliding stroke. The existence of the peak value at the end of the stroke is essentially caused by the interaction of the two wear scars interfering at the end of the stroke [94, 95]. Wear particles are a result of plastic deformation and ploughing [89, 95]. They form depressions and protrusions, increasing the interlock between contacting surfaces [96], requiring more tangential force and thus more energy loss. This friction behaviour (i.e. increasing with sliding rather than being constant) is termed as non-Coulomb friction due to the departure from Coulomb's idealisation that sliding friction is constant [97].

The increase in tangential force at the end of the stroke (non-coulomb behaviour) is a common feature of the gross slip phase in fretting experiments. It is believed that the increase is correlated to concentrated wear interactions at the edges of the interface [91]. To validate the suggestion that the

increase in friction force at the end of the stroke is correlated to the wear-scar effects, Mulvihill *et al.* [94] performed an extensive study on a nickel alloy Udimet 720 (often used in aerospace applications). The test initially started with a stroke length of 1 mm and 400 sliding cycles. The total displacement was then increased to 1.6 mm to observe what happens when the surfaces undergo sliding in fresh surfaces. The results were categorised into four discrete friction loops. It was first shown that in the first 10 cycles, friction results presented loops with an almost idealised shape (Coulomb behaviour) [94]. This means that there was no edge effect in the early stage of sliding. The loop shape evolved to a semi-parallelogram when the data was recorded after 400 cycles [94]. The increase in friction at the end of the stroke was clearly seen. This assures the correlation between the friction increase and wear. The total displacement was then increased to 1.6 mm to inspect the friction behaviour when sliding is taking place on fresh (virgin) areas. Reaching the new displacement was gradual and the data was recorded at a mid-point between the old and new displacement (taken after 8 cycles of the initial 400). An interesting feature was observed here in which the friction force increased to the same value reached after 400 cycles and then decreased just before reversing the direction [94]. The sudden decrease was observed as soon as the interface was slid on unworn areas (no effect of ploughing) [94]. The data was again recorded for cycle 13 after the initial 400. The displacement in this stage reached the final slip amplitude of 1.6 mm. The friction loop now showed the same behaviour observed in cycle 400 [94]. It can be deduced that the increase in friction at the end is because of ploughing caused by wear particles leading to interlocking resulting in the increase [94]. After realising the main reason for the friction increase, Mulvihill *et al* [94] expanded their study to investigate whether the edge effect is caused by macroscopic or microscopic interactions via applying a torsional fretting test. Fig. 2. 14 shows the two situations where the edge effects can impact the friction results. Two sample sets were designed to understand the scale of the wear effect. The first set was a cylinder with full ring shaped ends, whereas the second set involved segmented ring shaped ends on a cylinder as well. The two sample sets were in contact with a flat surface. The results showed that there was no observed difference between these two sample sets even for different pressure conditions [94]. This suggests that the friction increase at the end of the stroke is caused by the local interactions occurring on the peaks and troughs of the contacting pairs [94]. It can be also concluded that the surfaces obey the Amontons law (the independence of the COF on the normal load) as the change in the nominal contact area did not influence the COF [94].

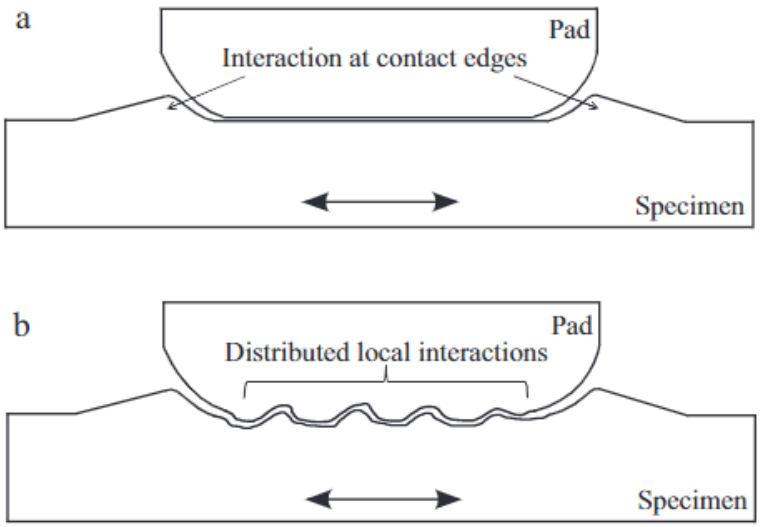

Fig. 2. 14. A schematic to illustrate the edge effects of a frictional interface into two possible cases: (a) interactions at the macroscale, and (b) microscopic interactions (peaks and troughs) [94].

The number of cycles in friction hysteresis loops is considered a prime factor. It directly affects the frictional behaviour of materials during the loops. This effect is normally observed by wear-scar effects that become evident in later cycles as presented earlier in the study of Mulvihill et al. [94]. It has been shown that the COF can vary significantly during sliding. In one study, the COF fluctuating from the beginning of sliding until exceeding $10x10^3$ cycles and then became stable [27, 98]. Similar findings were obtained by Long and Rack [99] to show the effect of a number of cycles on the COF. It has been suggested that the effect is mainly dependent on the materials used. It has been shown that constituents of titanium alloys play a prime role in the effect of cycle number on COF. This was observed in the first 20 cycles. After 20 cycles, the COF reached a steady-state stage (near 0.5) for all tested titanium alloys. This means that the COF is independent of alloy constituents after the initial cycles (i.e. after experiencing the running-in stage).

Following the impact of the number of cycles, sliding velocity is also an important parameter of hysteresis loops. The effect of sliding velocity is more pronounced in low contact stress (1.5 MPa) [99]. It has been shown that, under such contact stress, the lowest COF can result from the highest velocity [99]. Once the contact stress increased to 5 MPa, the impact of sliding velocity was not observed [99]. It has been also found that manipulating sliding velocity leads to an obvious change in friction [100]. This is dictated by the wettability and humidity of the contacting objects [100]. This study has shown that friction of an interface under high humidity can be decreased by increasing sliding velocity. This is because high velocity facilitates overcoming the effects of water molecules' presence in the highly humid interface [100]. In contrast, in less humid contacts, increasing velocity gives rise to an increase in friction due to stick-slip motion, which does not play a clear role in highly humid interfaces [100].

Investigation of friction hysteresis loops in the literature has been crucial in terms of helping to understand the detrimental effect of both fretting fatigue and fretting wear (and reduce their impact). The scope of such studies was usually directed towards material damage. The key observation which this review would like to emphasise is that the expected static friction peak appears to be absent in most published frictional hysteresis loops. The static friction peak is generally observed in unidirectional sliding – so why might it be absent in reciprocating sliding. This is the subject of Chapter 5 where the static friction peak in reciprocating sliding is explored via detailed experiments.

2.7. Friction and triboelectrification

Bringing two surfaces into periodic normal contact induces contact charges with opposite polarities due to a phenomenon called contact electrification [101] (electrons basically transfer from one surface to the other). When the periodic oscillation is sliding (rather than tapping), charges are also transferred and the phenomenon is then called triboelectrification. This phenomenon in a frictional interface generates tribo-current flowing in the direction of sliding and its value is usually in nA [102]. The magnitude of the tribo-current gives an indication of the size of the contact area and electronic properties of the tribo-layers [102]. This general contact phenomenon had been known since antiquity. It was useful for ancient humans to generate energy for heating and cooking. It is also seen in nature in the form of lightning or in daily life actions such as making a hair comb attract objects. This effect has been extensively studied recently attempting to minimise or utilise the output charges. Such charges might be detrimental, particularly in polymers that are involved in mechanical devices, as they possess a high ability to accumulate charges on their surfaces [18, 22, 103]. Polymers in such conditions are more likely to suffer from excessive heat which increases friction leading to operation failure [18]. The phenomenon also causes small charged particles to attract each other and agglomerate leading to severe problems with blockages of equipment and piping for pharmaceutical companies. Charged dust particles can also be a severe fire hazard! On the other hand, the output charges from the electrification effect originating from mechanical energy can be utilised to produce sufficient energy for powering miniature devices such as light-emitting diodes (LEDs) and self-powered sensors [104]. This can be produced by harvesting electricity resulting from mechanical motion via specialised devices. This capability is a somewhat recent development. The key device invented for the purposes of harvesting electrical energy from the triboelectric effect is known as the triboelectric nanogenerator (TENG). Invented in 2012 by Fan et. al [105], it uses thin dialectic layers to induce changes on backing electrodes (via electrostatic induction) and drive an alternating current as the surfaces continually separate and move back into contact.

Contact charges are usually associated with sliding friction tests of a metal-insulator interface. This is mostly seen due to the contribution of molecular factors, such as Van der Waals, Coulomb forces and

chemical bonds on the macroscale friction [21, 106, 107]. It was shown that the sliding mode is more effective than the tapping mode in charging the surfaces because there are higher compression forces in sliding [101]. This was concluded from experiments carried out on Kelvin probe force microscopy (FPFM) [101]. Interesting questions that arise are: how does frictional sliding contribute to charge transfer and indeed, how does charge transfer affect friction? An interesting environment to study this is the stick-slip scenario. Burgo and Erdemir [107] have shown that electrical signals fluctuated simultaneously with friction oscillations, suggesting that they originate from the same origin. This finding was also shown in an experimental study carried out by Budakian and Putterman [20] and a theoretical approach performed by Ananthakrishna and Kumar [19] where there was an obvious correlation between stick-slip events and charge transfer. In the stick events, bonds between atoms on the surfaces of metal and insulators are formed [20]. As the shear force is increasing, the bonds start to rupture causing slip events [19, 20]. Charges then begin to leave the metal after being stranded [20]. Results appear to indicate that charge transfer only occurs when slipping is taking place [20]. Experimental results showed coinciding jumps in charges with slip events, indicating the build-up of charges at these events, while the amount of charge remains constant during the stick [20].

Another way to correlate friction with contact charges is to impose chemical changes on a material's surface and observe the change in the frictional and electrical behaviour. Oxidation is one example of a chemical change that can be applied to a surface. Escobar et al [102] performed a triboelectric study using a metal needle coated with nickel and gold on an oxidised and as-annealed (original) diamond. The study aimed to investigate the macroscopic friction and tribo-current and correlate that with the electronic and tribological properties of the interface. The interface experienced a load of up to 0.3 N and a sliding speed of 20 μm/s. These relatively low values help inspect the micro-interactions between the surfaces during sliding. It was shown that the interface did not undergo plastic deformation (the tests were done several days later and no changes were observed) [102]. This might be because the load was too low to initiate plastic flow. The results showed that oxidation led to increasing friction and tribo-current [102]. The increase in friction is likely attributed to electrochemical interactions [102]. This was verified by a line fit that assumed a constant shear strength (excluding the adhesion contribution) and this perfectly fitted the results of both surfaces [102]. Both surface conditions exhibited a non-linear increase in the COF with the load (i.e. the interface does not follow Amontons' law) [102]. To further verify this assumption, the difference between friction values of the oxidised and original surfaces was obtained and then plotted with the load [102]. The friction difference and load relationship showed a linear increase. The authors [102] suggested that this excludes the physical contribution (adhesion) on friction as the difference appeared to be due to the chemical modification (oxidation). It is believed that the higher friction and

tribo-current observed in the oxidised surface are caused by a change in the electronic properties [102]. To validate this suggestion, the oxidised surface underwent brief further oxidation by imposing a voltage of 10 V through the needle on the surface. The voltage was applied for 0.5 seconds and then switched off. It was observed that the friction force instantly dropped followed by a gradual increase to the same level obtained before the former oxidation [102]. It can be said that the additional oxidation was not sufficient to increase the oxygen content which can result in higher friction [102]. The instant friction drop after applying the voltage is believed to be caused by the de-population of the electron traps on the diamond surface [102]. Initially, the electron traps were filled at equilibrium (before applying the voltage) [102]. When voltage was applied, the electron traps were de-populated leading to lower friction [102]. After removing the voltage, the electrons returned to their original traps leading to the same friction value [102]. It is worth noting that friction took 2 seconds to return to the original value which is believed to be the time for the electrons to de-populate the traps [102]. The higher tribo-current is likely because that oxidation gave rise to increasing electron affinity of the diamond (as this is a major contribution to the charge transfer) [102].

Charge transfer between a metal/dielectric interface has been the subject of many studies in the literature. It is acknowledged that in any contact scenario, the mechanism is a thermodynamic process of electrons on the molecular states of the contacting surfaces, where electrons transfer from high to low energy states. The main aim of the triboelectric studies was to understand the transfer mechanism in a metal/insulator interface. It is understood that the transfer mechanism during contact in a metal-metal or metal/semiconductor interface is achieved by coinciding with the Fermi levels of the pair to allow electrons to move from one surface to the other. The case for insulators (polymers) is quite different where the band gap is considerably large and some energy states within the band gaps can be considered to explain the transfer mechanism [108]. To ease understanding of the electronic structure of polymers (insulators), Fabish and Duke [109] have modelled the polymer's electronic energy states as double Gaussian peaks. The first peak is centred at the molecular anion energy (acceptor state), whereas the second peak is centred at the molecular cation energy (donor state). Occupation of these states is dependent on the molecular structure of a polymer [108, 109]. For example, electrons can transfer from a polymer to metal, if the relative positions of the filled donor states of the polymer are below the metallic Fermi level [108]. The electron transfer from metal to polymer occurs when the metallic Fermi level is above the empty acceptor states of the polymer [108]. The transfer mechanism can be represented by a potential well containing loosely bounded electrons in the out-shell of an atom [110]. During physical contact, the potential wells of the atoms overlap forming an asymmetric double well [110]. This allows the electrons to hop from Material 1 to Material

2 [110]. The transferred electrons will be trapped in the host potential well of Material 2 due to the energy barrier (at ordinary temperature), making the host material negatively charged [110].

The charge transfer mechanism in an interface between dielectric and dielectric can be represented by assuming their electronic structure as energy bands (the surface state model) [101]. It is worth noting that the structure of the valance and conduction bands are different from material to material [101]. This means that material A could have higher energy from the occupied states than the unoccupied states in material B [101]. Having materials with different electronic structures is necessary for the electron to transfer from one surface to the other [21]. With the presence of physical contact between the two materials, the electron is forced to transfer from the higher occupied energy states of material A to the lower unoccupied energy states of material B [101]. An illustration of the electron transfer in the dielectric/dielectric interface is presented in Fig. 2. 15. Once the electron is transferred, it cannot transfer back to its original position, because it will be trapped in the potential barrier of material B [101, 110]. In some cases, the electron can return to its original position in material A if it experiences an elevated temperature that provides the electron with enough thermal energy to return [101]. The charge transfer results in two surfaces with opposite polarities (material A will be positively charged and material B will be negatively charged) [101, 110]. It should be noted that the previous explanations of the transfer mechanism are only true if the dielectric electronic structure can be represented by surface states (energy bands) [101]. For dielectric materials that are not represented by the band gap structure, the mechanism can be explained by the potential wells of the two atoms [101]. The atoms are initially separated by a distance [101]. Their electrons are tightly bound in the orbitals of the potential wells [101]. When the two atoms are forced to contact, their electron clouds overlap forming an ionic or covalent bond [101]. With the presence of an external force, the bond length can be further shortened [101]. During the contact phase, the two potential barriers are joined to form an asymmetric double-well potential [101]. The electron then can transfer due to a lowered energy barrier between the two atoms leading to contact electrification [101]. After separation, the transferred electrons will remain on the surfaces as static charges [101]. To develop the discussion of electron transfer, Li et al [111] were able to determine the minimum separation distance for contact electrification to occur. They attempted to perform triboelectric tests using amplitude-modulated AFM to investigate the tip-sample interactions. When two surfaces approach each other, it is known that the vertical region above the opposing surface composes of attraction and repulsion regions [101, 111]. The free amplitude of the probe cantilever was set before the test to three values which are 50 nm, 70 nm and 100 nm. To see the impact of the amplitude on the tip-sample interactions, surface potential difference and vibration phase shift were examined. The results showed that the potential difference jumped from zero to a high value for the 100 nm and 70 nm, but

not for the 50 nm [111]. This indicates that contact electrification occurred only at higher amplitudes [111]. The higher amplitudes provide the probe with enough energy to overcome the repulsive force and move closer to the sample [111]. In this case, the probe reached the smallest separation distance above the sample surface [111]. The actual amplitude for the 100 nm and 70 nm were 95 nm and 62.5 nm respectively. Here, electron tunnelling occurs, thus contact electrification can be observed [111]. For the electron transfer to occur between the tip and the sample, the distance between them should be smaller than the bond length at equilibrium [101, 111]. The interatomic interactions are correlated to the overlap in the electron cloud of the two atoms (see Fig. 2. 16) [101]. The distance between the centres of these atoms is called the bonding length (interatomic distance) [101]. If the interatomic distance (x) is shorter than the equilibrium distance (a), the atoms repel each other because of the overlap, thus an external load is required to cause the contact [101]. The other case is when the interatomic distance is larger than the equilibrium distance, the two atoms are attracted towards each other due to reduced electron cloud overlap [101]. It can be said that bringing the two materials into contact results in shortening the interatomic distance so that electrons can flow [101].

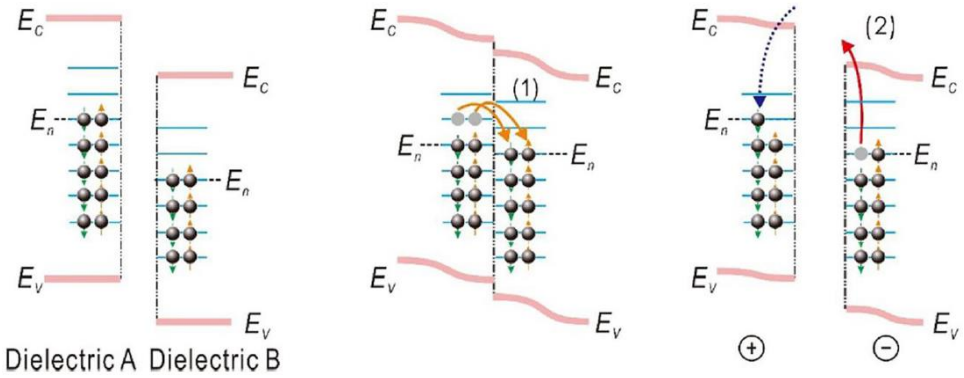

Fig. 2. 15. A visual explanation of the electron transfer in a dielectric-dielectric interface for insulators whose electronic structure can be represented by energy band gaps. The surfaces are initially apart. Then they are forced to contact resulting in an electron transfer. The surfaces are separated again and become electrically charged. The transferred electron cannot return to its original position unless it gains thermal energy [111].

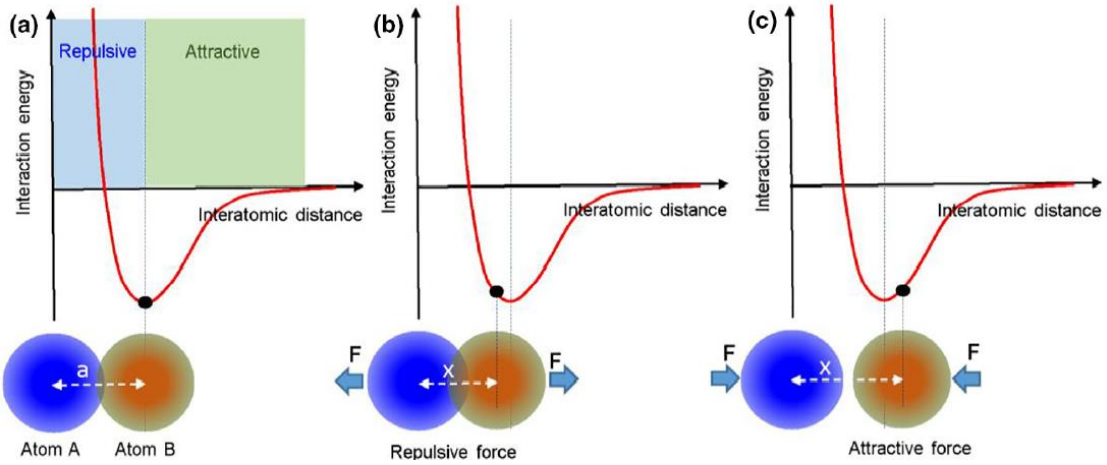

Fig. 2. 16. The atomic-scale interactions between two contacting atoms: (a) The two atoms are in the equilibrium state and separated by a bond length, (b) The atoms are in the repulsive region with a separation distance smaller than the bond length and (c) The atoms are separated by a larger distance than the bond length and they are in the attractive region [101].

The formation of tribo-charges is primarily influenced by the conditions of a test system. One main aspect is the normal load (contact pressure) which is a prime component of any contacting surface. It has been shown that there is a direct correlation between normal load and the formation of tribo-charges (contact charges) [19, 101, 103, 107, 112, 113]. The number of tribo-charges can be increased with increasing the normal load [103, 112-114]. This is because higher loads give rise to a larger contact area, resulting in more formation of charges [103]. The effect of normal load can also lead to an overlap between wavefunctions of electrons of the contacting surfaces, facilitating the electron transfer process [115]. For charge transfer to occur, the normal load needs to be sufficient to force the interatomic separation between the two surfaces to a shorter distance than the bond length [101]. When two materials are pushed into contact, a strong electron cloud/wavefunction overlap is created in the repulsive region between the atoms forcing the interatomic potential barrier to be shorter resulting in the electron transfer [101]. The relationship between contact charges and normal load in sliding contacts eventually saturates essentially when the real contact area saturates at high pressure [112, 114, 116] . The effect of the load-dependent real contact area on the electrical behaviour of triboelectric layers will be discussed later in this section. In addition to the normal load, test atmospheric pressure is also an important aspect of the generation of tribo-charges [107, 117, 118]. Experimental results showed that the highest current was obtained under a vacuum condition [107]. This is because high-energy species (e.g. x-rays, phonons) caused by mechanical stress aid the process of producing flowing current without obstacles from other factors [107]. Discharge into the air inevitably occurs in normal atmospheric conditions. The output current noticeably was reduced under

a reactive atmosphere (nitrogen and hydrogen) due to the presence of a high number of energy consumers that hurdle the flow of charges [107, 119].

As has been mentioned, charge electrification can sometimes be undesirable for certain applications, as it causes excessive heat on contacting surfaces leading to a breakdown. Many researchers have been able to mitigate the effect of the tribo-charges on contacting surfaces. It has been shown that eliminating contact charges helps to reduce friction at the interface, thus increasing the lifetime of materials [18, 103]. Using a discharge gun has been proven to be the most effective way to eliminate contact charges from the interface [18, 103, 120-122] in laboratory experiments. Other techniques involving solutions/solvents can be a good alternative to discharge the interface [18, 22]. At a lower degree, a grounding metal can be attached to one surface for contact charge mitigation [18, 103]. Owing to the metal's nature, most charges would be dissipated across the whole body of the metal away from the interface.

In other applications, it is necessary to keep and even increase the contact charge at the interface. This is the case for triboelectric nanogenerators. This technique benefits from the coupling effects of electrostatic induction and electrification [104]. Initially, two objects need to be in contact or close contact to electrically charge their surfaces. If there are stable (no relative movement), charges on both surfaces would neutralise due to charge induction. At this stage, there would be no potential difference. As soon as there is relative movement (lateral or vertical separation), the separated charges generate a potential difference [123].

As mentioned, work on TENGs has been ongoing since 2012 since the discovery by Wang's group [105, 124-126]. These studies have suggested various ways for optimal utilisation of the contact charges originating from mechanical movement. Starting from this breakthrough, many researchers have focused on optimising the contact arrangement to achieve desirable outcomes. The studies have been performed on mainly three different materials pairs. A typical material pair involves polymers on polymers with two electrodes attached to the backside of the polymers. Another contact pair composes of an electrode attached to the backside of a polymer that is in contact with another metal (known as the single electrode mode). The third option can be a polymer without an electrode on the backside in contact with a metal. Representations of these modes are illustrated in Fig. 2. 17. The selection of dielectric materials among studies in the literature mainly involves polyethylene terephthalate (PET), polytetrafluoroethylene (PTFE) and nylon (PA). These materials were often attached and/or in contact with electrode layers of copper (Cu), aluminium (Al) and indium tin oxide (ITO).

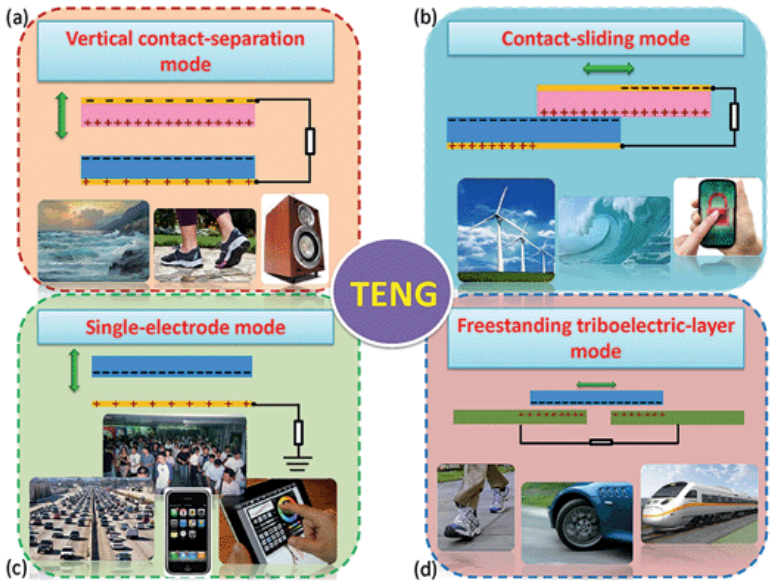

Fig. 2. 17. Representation of the four main types of TENG showing the possible application of each type [123]

The selection of materials in TENG studies is considered a vital aspect to help achieve optimal outputs. The key design table in this regard is the triboelectric series. Materials differ with regard to their tendency of losing/accepting electrons [104, 127, 128] and the triboelectric series is a ranking of materials from the most tribopositive at the top to the most tribonegative at the bottom. This affects how the charges are transferred between the triboelectric layers. An attempt to utilise the triboelectric characteristics was achieved by Song *et al* [127]. Their study has succeeded to realise the unidirectional flow of current using wood, Al and Cu. Recalling the positions of these materials in the triboelectric series, it is known that the electronegativity of copper is the highest and Al is the lowest, indicating that Cu has the highest tendency of accepting electrons and Al has the highest tendency of donating electrons when charge transfer is present. By this arrangement, electrons can continuously transfer from Al to Cu through wood realising the unidirectional flow of electrons. Eventually, this produces positive open-circuit voltage and short-circuit current at every event of charge transfer.

It is acknowledged that the normal load (contact pressure) is a critical element in triboelectric experiments. It is important to include a discussion on the impact of the load on the electrical properties of materials by revisiting studies that aimed to correlate the tribological behaviour of triboelectric layers with their electrical behaviour. The presence of contact pressure in any contact scenario is correlated to the real contact area. The dual effect of the normal load and contact area on the electrical output of TENG has been the subject of many studies in the literature, mainly in the normal contact separation mode [112, 113, 116, 129]. Recently, two systematic experimental [112, 116] and analytical [113, 129] studies aimed to correlate the load-dependent real contact area with the electrical output. Min et al. [112] and Kumar et al. [116] have shown experimentally that the

increase in normal load leads to engaging more contacting points, meaning that there is a higher chance for electrons to transfer. The analytical studies [113, 129] showed a similar trend for the observed increase in the electrical output and their results were verified experimentally using the same test conditions. The investigation of the real contact area can be done by applying a wide range of loads and then observing the effect on the results as performed by Min et al [112] and Xu et al [113]. This allows for investigating the evolution of the real contact area with the increase in the normal load, and, in the meantime, inspecting the electrical output. Both studies showed that the real contact area saturated at considerably large normal loads (contact pressure) where the real contact area was much closer to the nominal contact area (intimate contact). This saturation was also reflected in the electrical output which indicates the direct impact of the load-dependent real contact area on the triboelectric behaviour of the triboelectric layers. Another approach to correlating the real contact area with triboelectric output can be applied by varying the surface roughness of one of the surfaces at the interface. Kumar et al [116] and Vasandani et al [129] varied the roughness on their tested surfaces over quite a large range. The former used a sophisticated technique to fabricate different sets of samples with varied roughness. The latter subjected the surfaces to sandpapers of varying grit. The results in both studies showed that smoother surfaces generated higher electrical output than rougher surfaces due to the larger real contact area obtained from the smooth surface (for the particular material combinations being studied). The reason for the smaller real contact area resulting from rougher surfaces is that high peaks prevent the shorter peaks from contacting the counter surfaces leading to fewer contact points. Note that this outcome is typical of a rough soft surface being pushed into a smooth hard surface and the result would be expected to be different for the case of a rough hard surface and a smooth soft surface. To relate the correlation between the normal load and real contact area with principles of contact mechanics, Escobar et al [102] found that triboelectric output was proportional to the radius of the Hertzian contact area ($radius = \sqrt{Area/\pi}$). The proportionality was held for the whole range of the normal load which also indicates the dependence of the triboelectric output on the load. Their tested surfaces [102] exhibited a non-linear increase with the load (i.e. the interface does not follow the Amontons law). It is crucial to quantify the percentage of the real contact area experimentally to achieve a comprehensive investigation of the load-dependent real contact area and its impact on triboelectric behaviour. The two experimental studies [112, 116] joined their discussion of the dual effect by incorporating measurement of the real contact area and their studies are summarised in the following two paragraphs.

The Min et al [112] experiments used non-engineered surfaces (with microscale roughness) of copper and PET (the backside is coated with ITO) in the flat-on-flat contact arrangement. To ensure conformity, the surfaces were bonded to an optical glass plate that was very smooth and the lower

sample was placed on a spherical holder to permit self-alignment while keeping the upper sample fixed. Pressure-sensitive film was used to obtain a better estimation of the real contact area. The film composed of two PET layers named donors and receivers. The donor contained ink capsulated in micro-capsules that were crushed when the contact pressure exceeded the threshold of the capsules [112]. The ink of the crushed capsules transferred to the receiver layer [112]. Quantification of the crushed capsules provided an estimation of the real contact area. The lateral resolution was 2.6 μm corresponding to the size of the capsules [112]. It should be said that this resolution is quite low. However, this method is important because it indicated the evolution of the real contact area even if it was restricted to the microscale resolution. To visualise the evolution of the real contact area, the receiver was coated with a colour-developing layer and then post-processed to obtain the percentage of the real contact area to the nominal area [112]. The results showed that the open circuit voltage and the short circuit were increasing with the contact pressure up to 1176 kPa (753 N) [112]. The voltage and current then saturated at around 88 V and 0.83 μA respectively [112]. To rationalise the electrical output saturation after the linear increase, the pressure-sensitive layer was placed in between the triboelectric layers and applying again the same contact pressures that were applied to obtain the electrical output (the measurement of the real contact area was taken independently). The pre-test measurement of the real contact area showed that the pressure was evenly distributed across the interface, assuring conformity [112]. The visual investigation of the pressure-sensitive film showed that the real contact area was increasing linearly with the contact pressure until applying 1176 kPa [112]. Initially, at the low contact pressure (32 kPa), only a few contacting points were engaged [112]. Increasing the pressure led to engaging more asperities to form junctions [112]. For example, the percentage of the real contact area to the nominal contact area was only 0.29% for the 32 kPa and then increased to 7.3% for the 99 kPa [112]. The real contact area reached the saturation stage at a percentage of 82% when the pressure was 1176 kPa [112]. The evolution of the real contact area followed the same trend as the open circuit voltage and short circuit current. The low contact pressure produced a voltage of 14.9 V with only 0.29% of the real contact area [112]. When the pressure increased to the maximum, the voltage jumped to 87.5 V with a real contact area percentage of 82% [112]. These findings indicated that the charges are transferred only through the true contact between the contacting surfaces [112]. Finally, the correlation between the real contact area and contact pressure and their effect on the electrical output was visually demonstrated by connecting the TENG layers to a set of LEDs. As expected, larger contact pressure results in lighting up higher number of LEDs [112]. Even though Min et al [112] performed a significant systematic study on load-dependent electrical output by incorporating measurement of the real contact area, the indirect measurement of the real contact area was not ideal.

To obtain a more direct results on the relationship between real contact area and contact pressure and their impact on the electrical output, Kumar et al [116] performed in-situ measurement of the real contact area using direct optical observation. This study investigated the triboelectric behaviour of an engineered surface of soft polyvinyl-siloxane (PVS) in contact with mica. The PVS surface was fabricated using a moulding technique (the technique is explained in Ref [130]). The surfaces were made with different surface roughness ranging from 1.5 µm to 82.5 µm. Mica was chosen for this study because it has high dielectric strength, meaning that it has a higher ability for charge induction [116]. The other main aim was to estimate the real contact area of surfaces with different roughness. This was possible because the mica surface was transparent allowing the light beam to penetrate through the interface. The real contact area was estimated by observing the light interference [116]. When two asperities were in contact, the interference was destructive and it appeared as black spots on the optical image [116]. In the case where there was an air void, the interference was constructive and bright spots were shown in the image [116]. The triboelectric layers experienced contact pressure starting from 3.2 kPa to 64 kPa. The contact pressure applied in Kumar et al. [116] study was notably lower compared to what Min et al. [112] applied. The latter study is useful for applications that require utilisation of, for example, water wave energy, whereas the former can be used for sensors placed on shoes. The experimental results showed the typical increase in the output voltage with the contact pressure and this was observed for all the surfaces of PVS with different roughness [116]. The dependency on the contact pressure was mostly seen in frequencies higher than 3 Hz [116]. When comparing the results of the different surface roughness (keeping the frequency constant), the smoothest surface (1.5 µm) showed the highest output for the whole range of the applied pressure (3.2 to 64 kPa) [116]. The output voltage jumped from 43 V at 3.2 kPa to 316 V at the highest pressure [116]. An interesting feature of the relationship between pressure and voltage was that the smooth surfaces were more sensitive to the increase in pressure [116]. This was attributed to the sensitivity of the smooth surface on the change in the real contact area with the pressure [116]. For the power measurement, the open circuit voltage and short circuit current were measured to obtain the optimal power output. Again, the impact of the surface roughness was seen in the voltage and current [116]. As the power is the product of the voltage by the current, the power was also dependent on the surface roughness (i.e. real contact area) [116]. The highest power was 2.6 mW resulting from the smoothest surface, whereas the roughest surface generated only 0.9 mW [116]. The optical measurement of the real contact area under a nominal contact pressure of 64 kPa showed that the highest percentage of real contact area was obtained from the 1.5 µm roughness and it was 47% of the nominal contact area [116]. The percentage was significantly reduced to 12.6% (under the same pressure) for the surface with roughness of 82.5 µm [116]. It is observed that the lower limit of real

contact area percentage in the Kumar et al. [116] study was considerably higher than the one (0.29%) obtained from Min et al. [112] experiments. It is interesting to note that the lowest contact pressure applied by Min et al. [112] was 34 kPa, which is almost half of the maximum pressure of the Kumar et al. [116] study. The high percentage obtained from the latter study (Kumar et al.) was probably because the higher applied contact pressure (64 kPa) compared to the low pressure (34 kPa) applied in Min et al. resulting a lower contact area percentage.

The contact separation in TENGs can be essentially accomplished by two modes. The first mode is contact separation (CS-TENG) [105, 125, 126] which is commonly applied in the literature. Here, the surfaces are only separated/contacted in the normal direction with normally high frequency and small relative displacement (i.e. no gross sliding). The second configuration is the sliding mode (S-TENG). In this mode, three contact arrangements are commonly applied, including a conventional design of electrodes on both sides [131, 132], a single electrode [133, 134], and two electrodes with a gap between them (free-standing) [127, 133, 135]. The different designs were inspired by activities from our daily life [123]. For example, it is not always feasible to attach electrodes on both sides of triboelectric layers. This can be seen in the contact between a human hand and a touch screen, serving as a single electrode configuration [123].

In the final research chapter of this thesis (Chapter 6), the reciprocating sliding friction rig developed from the one in Chapter 3 is deployed to study the interplay between friction and triboelectrification. Therefore, the S-TENG is the relevant TENG in this work. In the S-TENG, it is important to consider displacement and velocity in order to obtain optimal outputs. It has been suggested that the highest electrical outputs can be obtained by applying sliding displacement just before reaching the edge of the contact interface, utilising the full viable sliding length [132, 136]. However, this might lead to misalignment between the contacting materials when the normal load is applied and reaching almost full lateral separation (see Fig. 2. 18). It has also been shown that increasing the velocity (or frequency) gives rise to higher current density and output voltage [136]. Shao *et al* [131] have claimed that the effect of increasing velocity results in a higher rate of reaching the maximum transferred charges, but it does not increase the number of transferred charges. It can be concluded that the dependence of electrical output on displacement and velocity is determined by the event of tribo-charge separation. A larger displacement range and higher velocity would mean higher possibilities of charge transfer. A larger displacement would increase the contact area, resulting in more possibility of charge formation. In the case of high velocity, there would be frequent charge separations in a given time, preventing interface induction from occurring.

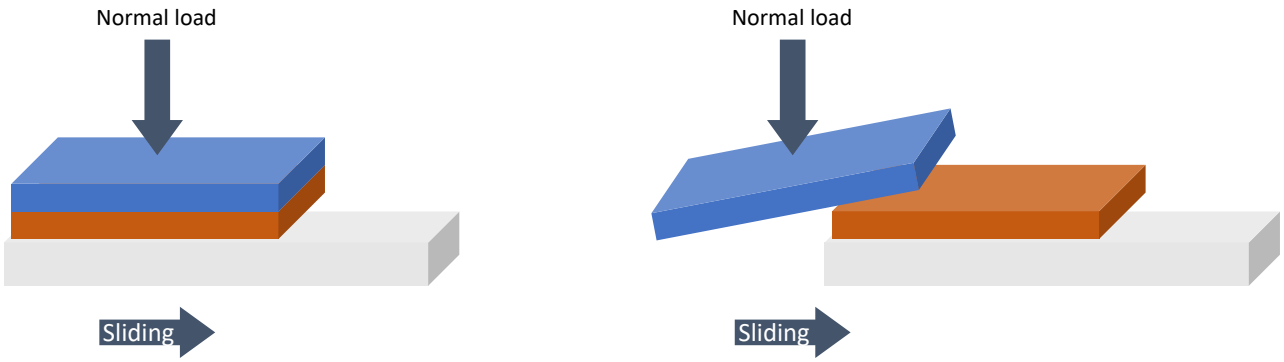

Fig. 2. 18. Schematic for misalignment that might occur in full lateral separation

The differences between these two modes have been pointed out in terms of experimental design and electrical outputs. For instance, the relative displacement is significantly low (mostly up to 1 cm) in a CS-TENG test compared to, usually, 5 to 7 cm in the S-TENG to achieve better charge separation. The large displacement permits the S-TENG to obtain higher total transferred charges, which makes them very useful for energy storage applications [127, 135]. Furthermore, S-TENG can be advantageous over CS-TENG because of friction between the contacting surfaces aiding to the acquisition of tribo-charges [22, 132, 136]. It should be noted that the existence of friction makes the surfaces highly susceptible to wear. Consequently, an optimal contact scenario should be applied to mitigate the impact of wear.

S-TENG mode has attracted researchers' attention in recent years due to its potential for improvement. Literature on the S-TENG often lacks consideration of tribology and mechanics aspects during the measurement which has drawn tribologists' attention towards TENG in the past few years. One aspect is that the normal load has not been mentioned in many S-TENG studies which is an elementary element of any frictional test. It has been also observed that some studies performed sliding by hand which clearly cannot maintain systematic control over the test! In a test with frequent events of movement, it is always necessary to carry out the test in a highly controlled system of applying normal load and sliding to help control and study friction between triboelectric layers. Recently, Armitage and co-workers carried out some interesting tribological studies on the behaviour of interacting triboelectric layers in the S-TENG [115, 137]. The principal aims of the two studies were to showcase the impact of surface topography, friction and wear on the charge accumulation of a S-TENG interface. The S-TENG configuration applied in the experiments was the free-standing mode arrangement. It was incorporated inside a commercial tribometer to obtain concurrent and accurate measurements of friction and charge for a dielectric/metal interface. In one study [137], the effect of surface roughness was clearly seen in the charge accumulation. It was shown that the smoothest surface was capable of accumulating higher charges (and vice versa) [137]. As stated earlier, smoother

surfaces facilitate attaining intimate contact with the counter surface, resulting in a larger real contact area. Having a larger real contact area means a better possibility of accumulating surface charges. The other study [115] was directed to correlating friction and wear with the electrical output of the S-TENG. Three polymers labelled as POM, PA66 and PTFE were in contact with polished steel and Aluminium. The polymers were tested in two conditions, ground and polished. In triboelectric experiments, it is often expected to see the effect of the normal load on the charge formation. The load effect was seen in increasing the rate of charge accumulation and density of saturation charge [115]. The maximum charge density was obtained from PTFE surfaces in contact with polished Aluminium. After reaching the maximum, the charge stabilised for a few minutes [115]. This was then followed by a drop which was also observed in the COF [115]. It is believed that the drop is caused by a transfer film from the PTFE deposited on the counter surface [115]. This transfer film created a new triboelectric interface that generates fewer charges than the original [115]. This leads to generating a contact between a worn surface of PTFE and a deposited transfer film as a counter surface, substantially reducing the accumulation of charges due to a lower contact potential [115]. Also, the previously trapped tribo-charges might be removed due to "de-electrification" between PTFE and the transfer film of PTFE. The drop in the COF is likely as well to be attributed to the transfer film [115]. It is believed that the film acted as a lubricant facilitating the sliding of the frictional interface [115]. This was validated by the behaviour observed in the contact between PTFE and hard polished stainless steel. The transfer film in such an interface (PTFE/stainless steel) was produced faster due to a higher difference in hardness between the PTFE and steel (hard-on-soft scenario) [115]. The effect of wear was observed by optical inspection techniques and related to the triboelectric results, but there was not a decisive conclusion on the correlation between friction and tribo-charge. Interestingly, a recent 2020 study on the sliding TENG (Wu et al. [138]) showed that wear can be significantly reduced by the addition of lubrication and that the lubricant boosted the TENG output by up to three times. It was found that the lubricant had the effect of preventing the formation of the polymer transfer film noted above. A study by Zhou et al. [139] confirmed these results and demonstrated that another key reason for higher electrical output was that the lubricant also supresses interfacial electrostatic breakdown and reduces charge loss after triboelectrification. This interplay between friction, triboelectrification and wear is still not sufficiently understood, thus further investigation with varying test parameters is required.

This study aims to correlate the frictional behaviour (friction and wear) of triboelectric layers on TENG performance. Due to the nature of S-TENG experiments, friction between triboelectric layers is inevitable, but it has not been closely studied with regard to its effect on the electrical output of the S-TENG (other than Armitage at al [115]. It should be noted that there have been extensive studies on

the effect of friction on contact charges [18-22]. The S-TENG studies often overlook such investigations. The study also intends to perform a comprehensive comparison between CS-TENG and S-TENG. Even though it seems difficult to apply a comprehensive comparison between these modes, researchers have attempted to point out the differences in terms of experimental design and electrical outputs using the same materials and similar experimental parameters. These attempts mainly lacked a systematic tribologically sound testing approach.

2.8. Conclusion

A review on investigating the frictional behaviour of contacting surfaces has been presented. First, the fundamental physics of static and sliding friction were explored including the empirical laws such as Amontons' law. This topic was followed by reviewing methods of performing friction tests. It aimed to highlight techniques and methods that researchers used to study sliding friction that might inform the present work involving the friction of nominally flat surfaces in both unidirectional and reciprocating sliding. This part of the review has shown the utilisation of mechanical movement of parts involved in the setup to initiate and measure friction force as well as the use of motorised/electrical equipment. After discussing the basis and measurement of sliding friction, surface structuring techniques that have been implemented in friction tests have been reviewed. It has been demonstrated that LST and PCT can influence the tribological behaviour of contacting surfaces. Although the level of accuracy in controlling and tailoring parameters like friction is somewhat uncertain. PCT is believed to be superior to other structuring techniques due to its flexibility and high productivity. LST is not preferable for some applications as it might introduce chemical changes on printed surfaces and does not produce highly accurate features. Diverting from the tailoring of friction via surface structure, studies on friction in reciprocating sliding have also been surveyed. Here, the review identified that the static friction peak appears to be absent in most of the published frictional hysteresis loops from reciprocating sliding tests. This is followed by a review looking at the role of friction in triboelectrification and vice versa. A brief explanation of the effect of friction on surface charge formation has been included in the survey. The investigation also involves a short survey on TENG and its types focusing on the S-TENG mode. It was found that many sliding TENG tests have been carried out without a sufficiently accurate test setup for both control of the experiment and measurement of parameters like normal and tangential load. This coincides with a general absence of tribological and mechanics based investigation although some recent papers have begun to study TENGs through the lens of tribology and mechanics.

Having reviewed studies on the frictional behaviour of contacting surfaces, it was necessary to tackle the research gaps that have been found in the literature. It was noticed that friction of structured interfaces can impose changes to the tribological behaviour of surfaces. Some studies showed that

structured interfaces are beneficial in controlling/enhancing friction and wear. This, however, was contradicted by other studies in the literature. Such studies found that structured interfaces did not enhance tribological behaviour; interestingly, they even generated higher friction and wear. The un-agreement on the impact of surface texturing on friction was the first research gap that needed investigating. With the continuous review of the frictional behaviour of surfaces, it was observed that the static friction peak was not apparent in reciprocating sliding. This was an interesting feature as the static friction peak was seen in most of the unidirectional sliding studies. To widen our understating of friction, the role of friction in triboelectrification was surveyed to inspect how friction can affect the triboelectric effect of materials. These three main research gaps were the driving force for carrying out a friction study to acquire a better understanding of friction. To apply such a study, a bespoke friction rig was designed to tackle these gaps. The next chapter will present and discuss the importance of the rig in achieving reliable friction results.

Chapter 3: Rig description

After identifying the research gaps, a customised friction rig was built to perform friction studies by applying different contact scenarios to enhance the understanding of friction. The friction rig was initially built to attain friction results from flat-on-flat contacts in unidirectional sliding. The rig was then adapted for carrying out reciprocating sliding to enable the study in Chapters 5 and 6. It is necessary for designing a friction experiment to ensure that a friction interface is solely influenced by the experiment parameters assigned. This means that it is desirable to isolate external factors from contributing to the resulting friction force. This gives rise to challenges associated with designing a rig that fulfils the requirement. These challenges will be discussed in the following section. This is followed by suggested solutions to mitigate the difficulties encountered. The final design will then be described in detail.

3.1. Challenges in Friction Rig Design

Challenges for designing the friction rig are mainly related to chosen materials. Materials choice is critical as different parameters of friction tests would be restricted to the properties of the interface. For example, the main aim of performing a friction test in this project is to conduct an experimental study to inspect the frictional behaviour of structured and unstructured surfaces of silicon. Silicon is not a typical material for performing mechanical testing. Therefore, it is important to find an effective way to obtain the best possible results from silicon samples. Silicon is also known as a brittle material which is highly susceptible to breaking during testing. In addition, the silicon samples used in this study are just around 1 mm thick. Consequently, it is required to select a reasonable range of an applied load (pressure) that avoids sample failure. Knowing the allowable normal load would be useful to facilitate choosing a suitable load cell capacity.

Load cell capacity and load conformity are the crucial aspects that dictate selecting a load cell. The capacity of a load cell implemented to measure the normal load needs to match the applied load. This is vital as applying a low normal load on a large capacity load cell would lessen the accuracy of the measurement. Similarly, a load cell used for measuring tangential force should match the anticipated force range. The tangential force range can be anticipated by knowing the normal load range and the COF of the materials to be tested. Another critical aspect of choosing a load cell is to consider the conformity of the load applied to the interface. The chosen load cell should produce an equal distribution of the load over the interface.

Choosing suitable load cells is not the only main concern for measuring forces involved in the friction test. Forces measured in the friction test, particularly tangential force, should have solely resulted from the interface. Realistically, this is not readily possible. It is necessary for any friction interface that is not between the tested surfaces to be kept minimal during the whole experiment. It is also

important to ensure that there is no shear stress between a load cell implemented to measure normal load and an upper surface during sliding. Furthermore, it is necessary to maintain the load while the sliding is in progress.

These are the challenges that might be encountered while performing the friction test. It is vital to consider these challenges before proposing a design for the friction rig. In the next section, some suggestions will be shown that can be implemented to overcome the challenges.

3.2. Suggested Design Options

As silicon is not typical material for performing mechanical testing, it is essential to bond silicon samples to backing plates for testing. This prevents their failure, leading to obtaining more reliable results. The bonding would also increase the sample thickness which can expand the normal load range.

Knowing the range of normal load would help identify suitable experiment parameters, particularly the tangential force. The tangential force can be estimated by employing a simple method that involves an inclined plane. In this method, one of the samples should be fixed on the plane. The other sample would be free and experience sliding. The plane angle with respect to the initial position is then increased until siding occurs. The COF of this interface can be known by obtaining the trigonometric *Tangent* of the sliding angle. Friction force can then be calculated by using Eq. (1). This gives an estimated value of the tangential force that should be expected from conducting a test on these surfaces. A simplified explanation of the inclined plane is presented in Fig. 3. 1. This simple approach helped to select a suitable capacity for the tangential force load cell.

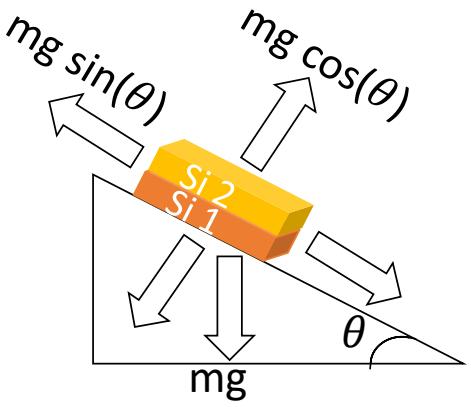

$$\mu = {}^{mg\sin(\theta)}/_{mg\cos(\theta)} = \tan(\theta)$$

Fig. 3. 1. A diagram of the inclined plane showing the forces affecting the interface between the silicon surfaces. The force of gravity is equal to mass (*m*) x gravitational acceleration (*g*), the normal load is represented by *mg cos*(*θ)* and friction force is obtained by *mg sin*(*θ)*.

Having selected the suitable load cells, minimising the contribution of external factors on the measured tangential force should be also considered. Normally in sliding experiments, one surface stays stationary while the other is pulled. The sliding part is obviously experiencing friction with parts not related to the contact zone. Therefore, it is required to attach the sliding surface to rollers that have minimal friction towards their counter objects. This would help have a semi-isolated friction interface from the surrounding, giving rise to a more accurate measurement of the tangential force.

3.3. Final friction rig design

Benefiting from the suggestions that can overcome the challenges associated with the rig design, a customised rig was built to study friction. The rig is similar to the "sled type" friction tests in ASTM D1894 [140]. The rig is adapted to perform friction tests on unidirectional and reciprocating sliding, widening its applicability for a broad range of tests. Fig. 3. 2 illustrates a 3D rendered model of the rig incorporated with an inset schematic showing the contact zone in more detail – the key components are marked with numbers. The blue arrow in the figure indicates the contact interface. The backside of the upper (1) and lower (2) specimens were bonded to upper (3) and lower (4) backing blocks. Compression springs were utilised to apply normal load *P* that is transmitted to the interface by pressing an x-shaped arm (5) attached to a 110 N miniature button load cell (LBS, Interface Force Measurements, UK) (6). This load cell is designed with a spherical tip to optimise the alignment between the upper and lower specimens because the alignment (conformity) is critical for a flat-on-flat interface. The lower backing block experiences the tangential load through a connecting rod (7) attached to a motorised linear stage (8). The moving part of the contact is positioned on a very low

friction linear bearing (9) with uniaxial movement fixed on a base plate (10). The two sides of the rig are joined via a tension/compression load cell (SML, Interface Force Measurements, UK) (11) and are aligned with the connecting rod to measure the tangential load *F*. To prevent the upper specimen movement while sliding, a stopper set (12 and 13) is included to prevent bulk sliding of the upper plate. For the reciprocating sliding, the other side is adapted with placement of a second set of stoppers to prevent any lateral movement from the upper specimen in the opposite direction. It is worth noting that humidity was not monitored in all the experiments performed in this project. It was believed that the lab space used for carrying out the tests was suitable for performing friction tests in ordinary conditions.

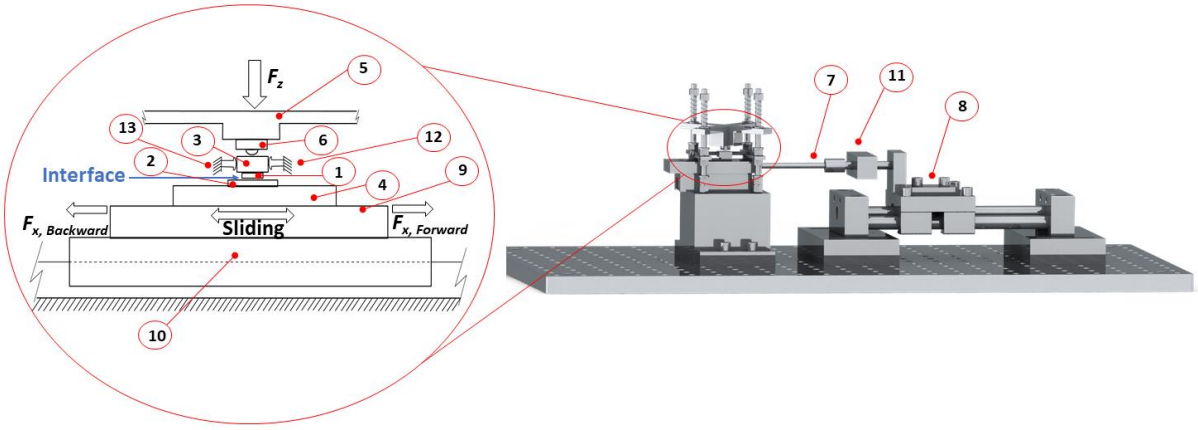

Fig. 3. 2. Schematic of the friction rig setup: (1) Upper specimen, (2) Lower specimen, (3) Upper backing block, (4) Lower backing block, (5) X-shape arm, (6) Button load cell, (7) Connecting rod, (8) Motorised linear stage, (9) Low friction ball bearing, (10) Base plate and (11) Tension/compression load cell (12) and (13) stopper set.

A LabVIEW code was developed to perform unidirectional and reciprocating sliding and simultaneously measure tangential force. The motion control framework is originated from a pre-programmed code designated for "National Instrument" motors using a modulus called "Softmotion". The basis of this code was used to effectively interact with the motor to perform the intended movement. The motion control is incorporated with data acquisition (DAQ) interface for measuring normal load and tangential force from the load cells that are connected to the "National Instruments" DAQ system. The LabVIEW code runs the motion control commands and DAQ interface simultaneously to synchronise displacement with friction data. For reciprocating sliding, the code was optimised to immediately change the sliding direction at end of each stroke. The code also permits assigning waiting time (dwell time) after each stroke, in case the investigation of dwell time is needed. It should be noted that friction and displacement data were post-processed for the experiments performed in Chapters 4 and 5. The friction data were initially obtained as tangential force vs. time. Similarly, the displacement data were coordinated with time. As these two types of data were recorded at the same

time, it was possible to synchronise the friction data (from the tension/compression load cell) with the displacement data (from the motor).

3.4. Further details of friction rig development

The rig has been developed on different occasions through different stages. A decision was made early on to design and build a customised rig that could facilitate the testing needs of the project while being cost-effective. Considerable time was invested in designing and exploring different friction test approaches in the literature. The rig mainly needs to be divided into two parts (right and left). The right side includes the motor and linear guide with other accommodating parts to complete the linear motion. The left side composes of the interface and all parts associated with it, also a way to apply the normal load with ensuring conformity. The components of the left side and some from the right side had to be manufactured in the machine shop, so a time-consuming period was spent carefully designing these components with the proper geometry (shape, dimension, etc) while also considering the vertical height so that both sides matched up. Both sides were placed on a large mounting plate.

The first component to consider was the base plate that accommodates the remaining parts of the left side. The base plate incorporates multiple holes with different drill sizes to achieve flexibility and versatility. The height of the base plate was 50 mm and it has 14 holes (6 x M5, 6 x M4 and 2 x M3). Four of the M5 holes were drilled to attach four threaded posts that determine the four corners of this side. The M3 holes were used for a low friction linear bearing that was sandwiched between the base plate and the lower sample. Two M4 holes were made for an alternative linear bearing to replace the first one. The first linear bearing that we used was not suitable for our application due to its short travel length (13 mm). This was too restricted. As the main aim was to apply a unidirectional sliding, it was established that the 13-mm travel length would be adequate. After preliminary tests, it was realised that the bearing with this short length was not suitable. Additionally, the bearing did not behave properly when there was a moderate normal load and tangential force. An alternative linear bearing with a 38-mm travel length was purchased and fixed on the base plate. This choice was successful as variable test scenarios were performed (slow and high sliding; short and large travel distance) with the presence of normal and tangential loads. The friction of this bearing was tested before performing any friction test on our interface to examine its ultra-low friction feature. It was indeed shown that friction measured by the tangential load cell was too small to be distinguished from the data noise. The datasheet from the manufacturer's website states that the COF is approximately 0.003, which is considered to have a negligible influence on the measured interfacial friction trends. On top of the linear bearing, a lower backing plate was fixed. This plate was made with a hole on the side to act as a meeting point between the two sides. The height of this hole from its centre to the mounting plate is critical because it needs to match the force point on the other side where the

tangential force is applied. One pair of the interface was bonded to the lower backing plate. The lower sample was always unstructured silicon, except for the study of friction and triboelectrification (Chapter 6). The top sample was either structured or unstructured (again except for the study in Chapter 6). The upper backing plate was not fixed to the surrounding parts and it was without holes. The reason for not attaching this plate was to be movable when the normal load is applied to fully transmit the load to the interface. The normal load is measured by a button load cell possessing a spherical tip which allows the load cell to self-align with the interface to ensure conformity. The load cell is bonded to an x-shaped arm that has a hole on each end to be used for the posts. The arm was made with an extruded central region to permit a vertical distance between the arm and the interface. On the arm corners, four compression springs were inserted on top of the outer surface of the arm. The springs were accompanied by two washers and a nut. One washer is inserted between the arm and spring. The other one is put on the other end of the spring. The nut is then placed on the top. These components are repeated on the remaining corners. The load is applied by tightening the nut to compress the spring. This step is critical as the nuts from the four corners should be relatively tightened at the same time (or at least the opposite two sides) otherwise, the load becomes unevenly distributed (causing misalignment). The same procedure should also be applied when de-compressing the springs. This concludes the components involved in the left side of the rig. Engineering drawings of each of the manufactured parts are presented in the Appendices.

The side where the linear motion is initiated had to be altered a few times. Firstly, a bi-axial motorised stage that is originally used as precision positioning for a microscope was utilised for this study. The motorised stage was easily controlled in LabView. It was thought that it would be good to start preliminary experiments to use an existing stage in the lab. However, preliminary experiments showed that this stage was not useful for sliding tests. It was a struggle to achieve smooth movement. It was lagging almost in every sliding test. Then, the process of finding a suitable linear system started by considering some factors such as compatibility with LabView, ease of use and cost-effectiveness. The option chosen was a stepper motor from National Instrument. The manufacturer provides a pre-programmed code in LabView for carrying out simple motion which is applicable to the first topic. The second main element of the linear system was the linear guide. The criteria for such a component were to withstand moderate pulling forces and possess high step resolution (i.e. a high number of steps per revolution of the leadscrew). These two points can be determined by knowing the pitch size (i.e. the periodic distance between the thread) of the leadscrew. Smaller pitch size means more accurate positioning of the stage, but at the expense of less endurance of pulling forces and narrow speed range. This was necessitated for our first and second research topics because it is important to obtain sub-µm step motion of the intended displacement for friction studies that concern static

friction. To elaborate, for a pitch distance of 2 mm, the leadscrew of the linear stage transforms one full rotation to a linear distance of 2 mm. From this value, a motion resolution of 0.0001 mm per step can be maintained. This is crucial as it allows us to observe the friction behaviour in the pre-sliding regime and just before the occurrence of the static peak. It is worth noting that starting the sliding tests with this linear system was not straightforward. Some of the connecting parts between the motor and linear stage were not compatible, so some delays were encountered while new components where procured and installed. Performing the first two studies (Chapters 4 and 5) by using the customised rig was successful. There were not many changes to apply for the LabView code of the unidirectional sliding, but changes were required for the reciprocating tests. To enable reciprocating tests, the code had to be significantly modified (particularly the motion control part) to effectively achieve repeated sliding. The transition from a simple to sophisticated motion control actually was time-consuming because all inputs throughout reciprocating sliding needed to be inserted by the program without user interference. The difference between the two codes can be seen in the Appendices. Having succeeded in establishing a reliable and cost-effective friction rig, it was later used for two final-year projects and one MSc dissertation. The rig also attracted a company based in Ireland to use it for testing friction of their polymer coatings. Their aim for the coatings was to obtain the lowest possible friction. The low friction was required because the coatings were needed for biological devices that need convenient transportation inside the human body such as coatings used for aspiration catheter which helps tackle blood clot more easily.

To facilitate the triboelectrification work in Chapter 6, further significant modifications were needed. Moving from solely studying friction to the study of friction and triboelectrification, it is vital to have a system that is capable of performing high-frequency motion with the presence of normal and tangential loads. It was a challenge to move towards a relatively high sliding speed. Consequently, it was required to ensure that the rig can be used for TENG experiments. Some preliminary experiments were done and it was found that the linear stage cannot keep up with the high speed. After investigating this issue closely, it was realised that the specification of such a linear stage permits only motion with a relatively slow speed of up to 4 mm/s. This speed is too low for observing the triboelectric effect as opposite charges would be neutralised easily via charge induction. To achieve high speed from the linear stage, the pitch size needs to be much larger. After a discussion with the stage manufacturer, it was clear that the pitch size needed to be 50 mm to obtain sliding speeds up to 150 mm/s. The new speed range seems sufficient to investigate the triboelectric effect. After initial tests, the new stage was suitable for performing the TENG experiments. However, there is always a trade-off meaning that attaining the high-speed motion would be at the expense of more precise positioning. The step resolution for this linear stage is 0.01 mm. There is a considerable difference

between the resolution of the former and latter stages. It should be noted that the stroke length for the first two studies (Chapters 4 and 5) was 0.5 mm, so high step resolution is highly needed. The stroke length of the third study (Chapter 6) was 27 mm, thus the 0.01 mm seems reasonable.

3.5. Conclusion

A bespoke friction rig has been successfully built and utilised to carry out different scenarios of friction tests on flat-on-flat contacts. The rig so far is capable of performing unidirectional and reciprocating sliding with a relatively wide range of normal loads. To ensure good conformity of the contacting surfaces, the load cell used to measure normal load has a spherical tip allowing self-alignment of the two surfaces in contact. Additionally, using a low friction linear bearing ensured that the bearing contribution to the measured tangential force was negligible. Test control and force measurement were done using a self-programmed LabVIEW code. After a number of refinements and some troubleshooting, the rig was ready for testing. The rig was also modified to facilitate tests aimed at probing the relationship between friction and triboelectrification. The following three chapters describe the kinds of experimental studies completed using the rig.

Chapter 4: Tailoring the static friction of micropatterned surfaces

4.1. Introduction

The first experimental work to utilise the customised friction rig was to address the static friction of structured interfaces (the 1st research gap). As noted previously, an attempt to move one surface relative to another produces a resistive force tangential to the interface. Its limiting value at the onset of sliding is known as the static fiction force and its value during sliding is often called the sliding friction (or the kinetic or dynamic friction). The friction mechanism is rather complex and affected by multiple factors, including the physical, topographical and chemical properties of surfaces. Due to the many factors that can influence friction, it seems extremely difficult to control or tailor friction. Controlling friction is desirable for many applications, such as friction-damping applications. It can also be utilised in tactile technologies (e.g. touch screens). Despite the complexity around the friction mechanism, Amontons in 1966 [6] managed to deduce rather simple empirical laws for friction (dry friction). Recalling Eqs. (1) and (3) (Section 2.1), friction is linearly proportional to normal load (via the friction coefficient) and dependent on the real area of contact rather than the apparent area. Remarkably, these simple observations are applicable to a wide range of materials and surfaces. Using Bowden and Tabor's theory for sliding contacts $F = \tau_s A_r$ [13], it can at least be pondered that there might be a possibility of tailoring friction by controlling the real area of contact A_r. The hypothesis being: could A_r be controlled in such a way as to tailor friction. One way to achieve this is by structuring one or both of the contacting surfaces.

An extensive literature review on surface texturing has been presented in Chapter 2 (Section 2.3). Briefly, many tribology researchers have directed their efforts towards surface structuring due to its potential for controlling the tribological behaviour of interfaces. The common techniques that have been used in the literature are laser surface texturing (LST) [14, 51, 68-71] and photolithographic etching [75, 76]. There are also less common techniques that have been used such as crystallisation [77, 78] and micro-cutting [79]. Surface texturing has been particularly beneficial for lubricated contacts. It has been shown that it reduces friction by increasing hydrodynamic pressure [141] and increasing lubricant thickness [73]. In the case of the dry friction, it reduces friction by primarily entrapping wear particles in surface troughs [51, 68, 69], moving away these particles from the interface. It should be noted that surface texturing does not always lead to reduced friction. Kang et al. [15] have shown that textured surfaces significantly increased friction compared to their counterparts (untextured). This is attributed to the material pair and contact scenario used in their study. They used a hard metal pressing on a soft polymer which might lead to penetration causing an increase in contact area or interlocking. These two consequences have most probably caused the increase in friction. Despite the promising outcomes of surface texturing of features with nano and microscale on controlling friction, it has been rarely possible to accurately measure/control real area

of contact due to the complexity around the contacting objects. For example, laser texture is not really accurate enough to produce the kind of idealised topography required.

This chapter aims to explore the possibility of tailoring static friction based on manipulating the contact area of structured surfaces. This experimental work is directed to revisit (examine) the dependency of real contact area on friction based on the equation of Bowden and Tabor on the structured surfaces. It is also important to minimise any other dependencies that can directly or indirectly affect friction. For this reason, a contact arrangement of flat-on-flat with minimal surface roughness and high flatness is preferable to ensure better contact conditions with less effect from other influential factors. Benefitting from photolithographic etching, high-fidelity features with minimal surface roughness can be realised. Realising these features by photolithography allows for accurate control of nominal feature contact area. The fabrication was done on commercial silicon wafers with a flatness of less than 1 µm [142] and roughness of sub 1 nm [143]. It is an interesting exercise to investigate the frictional behaviour of these idealised surfaces and determine what friction laws are obeyed.

4.2. Surface fabrication and testing

A square wave pattern was fabricated on silicon surfaces that are in a contact arrangement with flat unstructured silicon surfaces. The pattern was produced on a commercial silicon wafer with a nominal area of 10 x 10 mm^2. The fabrication processes (steps) are summarised in Fig. 4.1. The silicon wafer was coated with a photo-sensitive substance known as a photoresist (S1828). When exposing the photoresist to UV light, the pattern area was protected from the light and other areas were exposed. Chemical bonds of the exposed photoresist were weakened due to the light exposure and it was washed away. Following this, deep reactive ion etching (DRIE) using the Bosch process [144] was used to remove the exposed areas while the remaining parts were protected. The feature depth of 70 µm was produced with near vertical walls. The samples were prepared in five different surface categories to produce feature contact area ratios (A_{nf}/A_n) of 0.2, 0.4, 0.6, 0.8 and 1 where feature contact area ratio is defined as the total nominal feature contact area A_{nf}(Column 3 in Table 4. 2) divided by the nominal area A_n (i.e. the total enclosed planar area of 10 x 10 mm^2). A schematic of the contact arrangement between these structured surfaces and the counter flat surface are illustrated in Fig. 4. 2. The structured surfaces were produced with a constant period of 100 µm and varying feature widths to form the four structure types. After fabrication, the samples were cleaned in an ultrasonic bath with acetone, IPA and RO water. The samples were immersed in these liquids for five minutes and then blow-dried using a nitrogen gun. Surface topography (roughness measurements) was studied using an Icon atomic force microscope (AFM) (Brucker, USA) with a scan size of 500 x 500 μm^2. The

scans were performed at five different locations of the structured and unstructured surfaces before and after friction tests. For the structured ones, the scans were done on top of the feature. Root mean square roughness (*Rq*) obtained from the scans was averaged among the samples with the same feature contact area ratio.

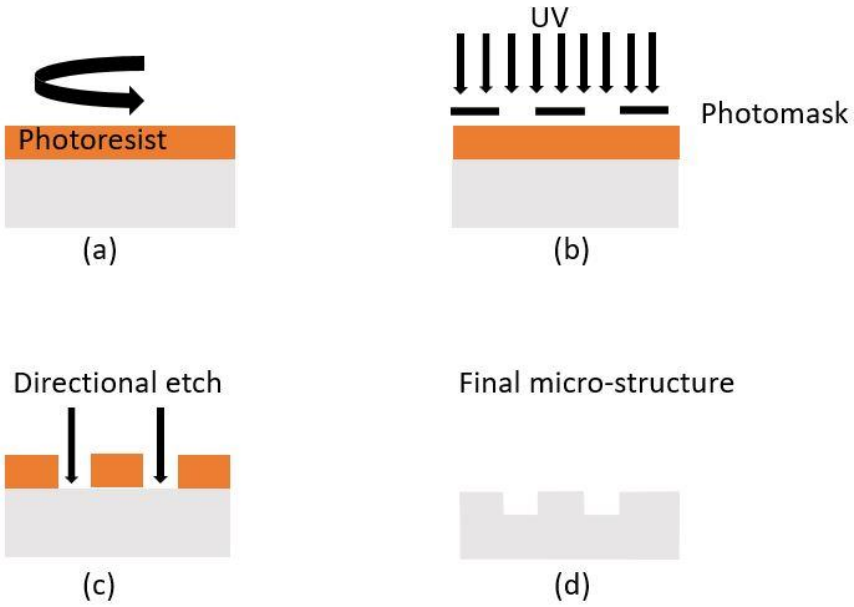

Fig. 4. 1. Photolithographic etching steps for structured surface fabrication.

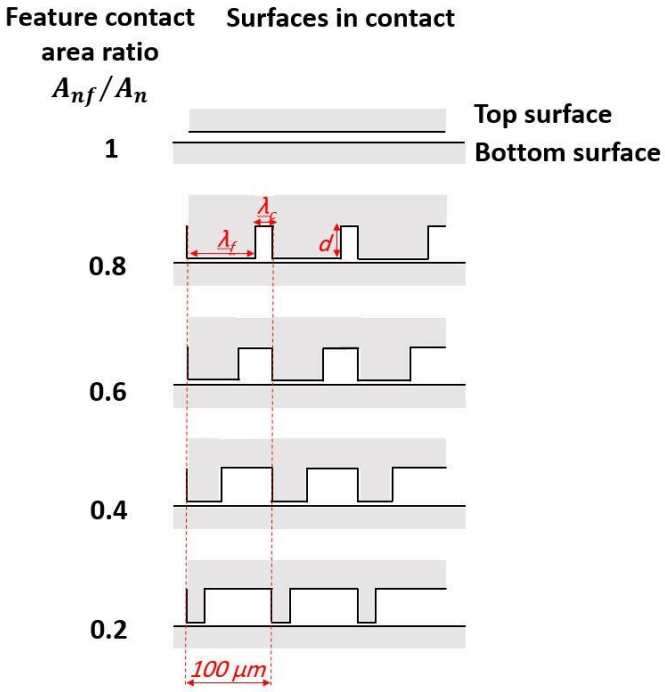

Fig. 4. 2. Schematic representation of feature contact area ratios. Feature contact area ratio $A_{nf}/A_n = \lambda_f/(\lambda_f + \lambda_c)$.

To obtain steady-state friction and minimise frictional instabilities, a running-in protocol [145] was performed for a total sliding distance of 10 mm with applying the maximum load (50 N). The contacting surfaces were then returned to the initial position. For each measurement, an increment of 5 N (normal load) was applied for each 0.5 mm sliding distance. The change in load (from its current value) started at the end position of the 0.5 mm sliding. Nine increments of 5 N were applied, leading to a total distance of 4.5 mm. Five repeats on fresh samples were performed for each feature contact area (0.2, 0.4 0.6 0.8 and 1). The orientation of the structured samples (linear grating) was parallel to the sliding direction (moving out of plane of the drawing in Fig. 4.2). Control of the motorised stage and data logging was done using a LabView program. The program receives amplified signals from the load cells transmitted through a NI-9237 full bridge amplifier (National Instruments, UK). Displacement inputs were passed to the PC through an ethernet cable. The rig setup in this experimental work is slightly different from the schematic presented in Fig. 3.2. The schematic of the unidirectional sliding work is illustrated in Fig. 4. 3. with an inset drawing indicating the key components.

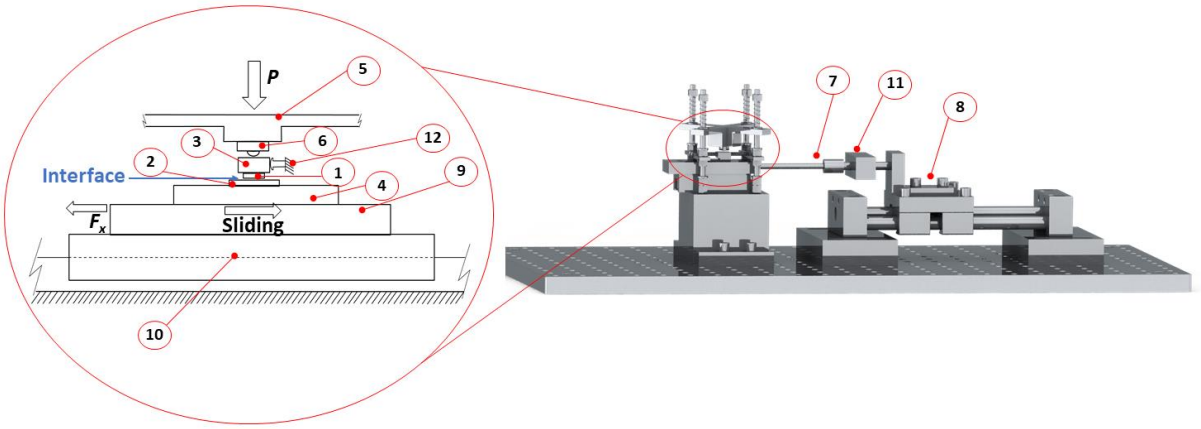

Fig. 4. 3. Schematic of the experimental 'sled type' friction rig: (1) Upper silicon specimen, (2) Lower silicon specimen (always flat), (3) Upper backing plate, (4) Lower backing plate, (5) Upper arm, (6) Miniature button load cell, (7) Connecting rod, (8) Linear bearing, (10) Base plate, (11) Tension/compression load cell and (12) Stoppers.

4.3. Results and discussion

The roughness measurement of pre-and post-test scans is presented in Table 4. 1. The surface roughness of samples before testing was in the range of 1.2 to 3.2 nm, which can be considered the limiting values of the tested samples. Surface roughness parameters (*Rq*, *Ra*, *Rz*, etc) were measured in the AFM by scanning surface heights (surface irregularities) of each horizontal line of the scanned area. The corresponding roughness parameter used in this study was *Rq* (RMS of asperity heights). Roughness measurement after testing was affected by wear experienced during the test (or running-in), causing slightly flattened surface asperities.

Table 4. 1. Mean RMS surface roughness *Rq* before and after testing. Roughness values are the mean of five different scans per sample for each of the five repeat tests (i.e. mean of 25 measurements). Bracketed values are standard deviations.

Feature contact area ratio	RMS Roughness *Rq* (nm)	
	Before	After
0.2	1.8 (0.46)	1.1 (0.51)
0.4	2.1 (1.22)	1.2 (1.33)
0.6	2.3 (0.62)	1.0 (0.46)
0.8	2.1 (0.57)	1.2 (0.18)
1	1.2 (0.89)	0.6 (0.24)

Representative sliding curves of the tested samples are presented in Fig. 4. 4. The figure includes five graphs representing each of the feature contact area ratios. Each graph consists of five sliding curves showing the relationship between the tangential force and sliding displacement. Almost all graphs showed clear static peaks followed by approximately constant sliding friction. Notably, a consistent increase is seen between individual curves for the five normal loads. The consistent step increase in the sliding curves suggests a linear relationship between the normal load and friction force. This is evident in Fig. 4. 5 (a) which shows the linear relationship between the normal load and static friction. The linearity confirms the Amontons' behaviour (1st law, $F = \mu P$) of the tested surfaces (structured and unstructured), despite their nanoscale roughness. This is also confirmed in Fig. 4. 5 (b) showing the independency of COF (μ) on the normal load. To examine the second law of Amontons, Fig. 4. 6 shows the relationship between COF and the feature contact area to inspect the possibility of tailoring friction by manipulating the feature contact area. It can be seen from the graph that COF seems independent of the change in the feature contact area. This is observed in the COF of 0.4, 0.6 and 0.8, resulting almost constant COF of 0.4. The two remaining cases (0.2 and 1) are slightly above and below this value and can be regarded as outliers. Considering the unstructured case, samples in this category were not involved in the fabrication processes, particularly etching. Such processes can form unwanted features (e.g. tiny adhered particles, feature edge effects etc.) that can slightly alter the surface topography. Regarding the 0.2 outliers, it is more likely to be attributed to the small width of the features compared to the other structured samples (all the structured surfaces were fabricated from a single silicon wafer). This might lead to not properly transferring the pattern on the surface. Eventually, it can be concluded that it is difficult to establish a dependency between the feature contact area and friction for our tested surfaces.

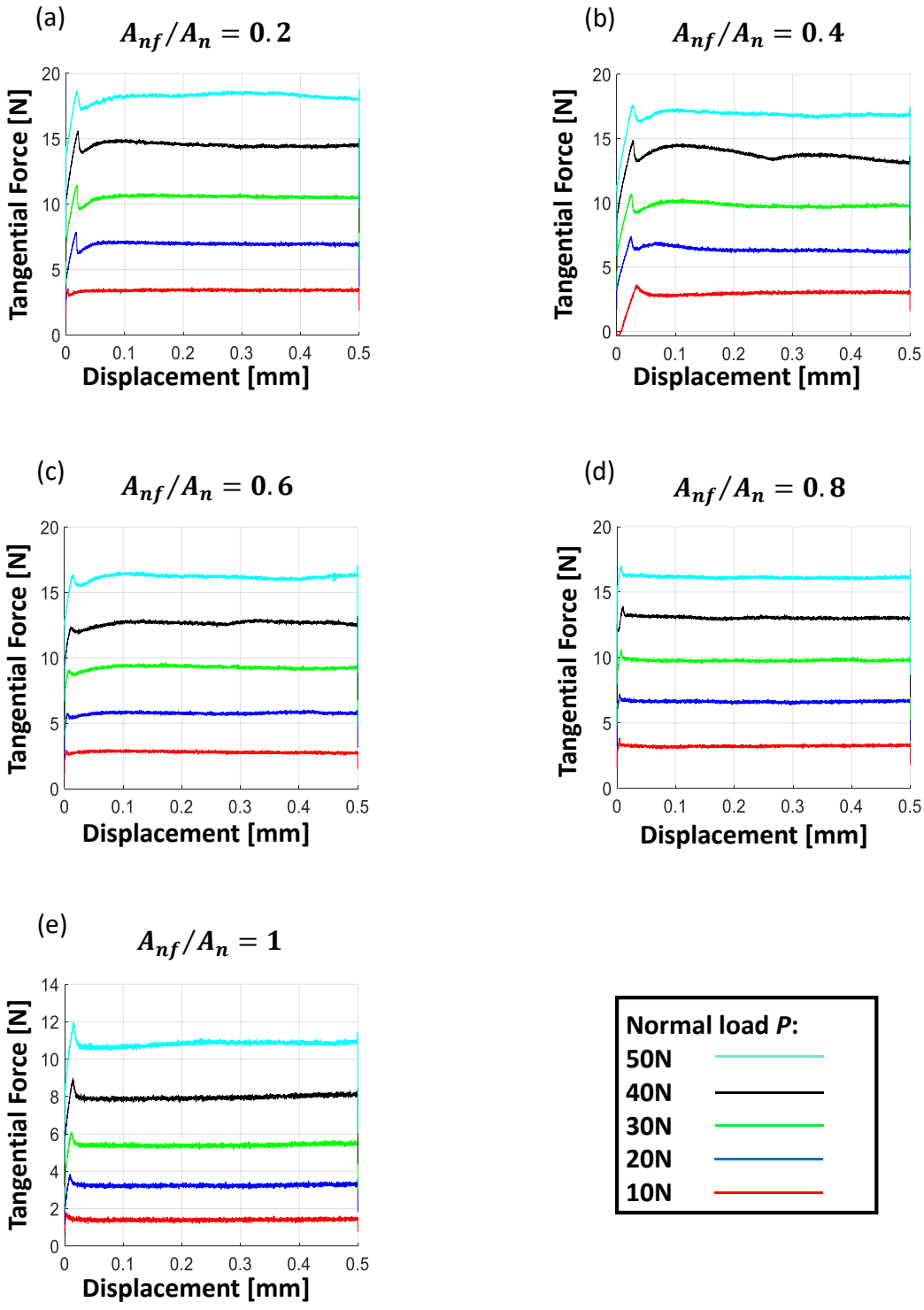

Fig. 4. 4. Representative tangential force versus displacement plots for surfaces having feature contact area ratios (A_{nf}/A_n) of: (a) 0.2, (b) 0.4, (c) 0.6, (d) 0.8 and (e) 1. Each plot shows the effect of varying the normal load *P* (see legend).

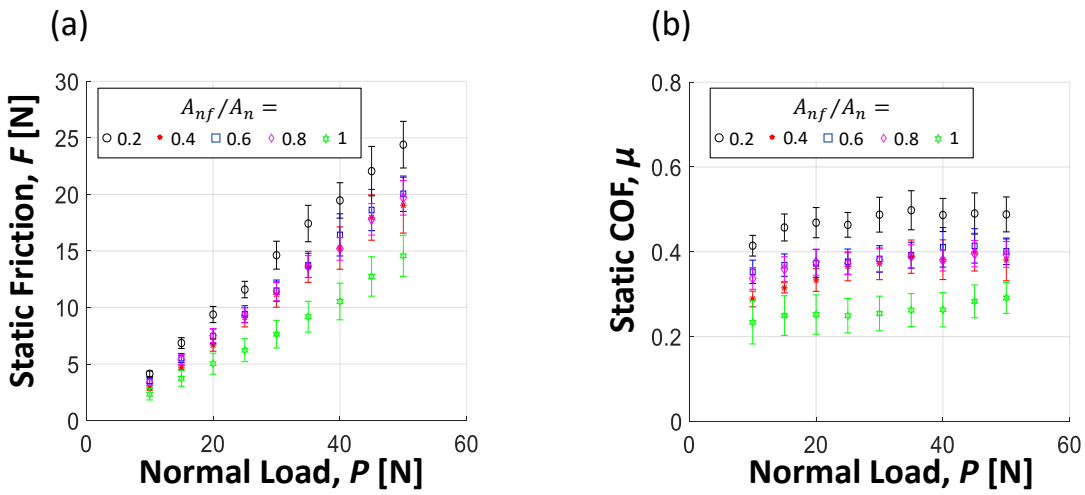

Fig. 4. 5. (a) Static friction force *F* versus normal load *P* (for all feature contact area instances) and (b) coefficient of static friction μ versus normal load *P* (also for all feature contact area instances*).* Feature contact area ratio *(*A_{nf}/A_n*)* is given in the legend.

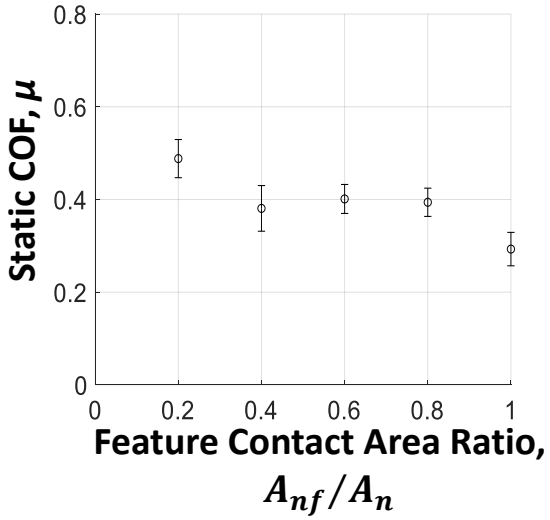

Fig. 4. 6. Coefficient of static friction μversus feature contact area ratio (A_{nf}/A_n).

To expand our discussion about the dependency of friction on feature contact area and relate that to the real contact area (A_r), we should return to the well-known equation of Bowden and Tabor ($F = \tau_s A_r$) where friction is given by multiplying interfacial shear stress by the real contact area. Understanding the behaviour of A_r would provide a more thorough explanation of the resultant friction. It is always challenging to calculate A_r for frictional interfaces, particularly opaque samples. However, it can be estimated by using theoretical approaches accompanied by experimental data on surface roughness. This study has implemented two well-established modelling approaches named the Bush, Gibson and Thomas (BGT) model [146] and the Boundary Element Method (BEM) [147, 148] to estimate the real contact areas. It should be noted that the BGT approach is only valid for contacts

under relatively small contact pressure, similar to the experiments performed in this study where the real contact area constitutes a considerable low fraction of the nominal area (which can be < 1%). It is important to note that the model work was based on the assumption that the contact was between a flat rough surface and a rigid flat surface (i.e. surface roughness was measured and implemented for only one surface). The purpose for such an assumption was to obtain a qualitative comparison between the experiment and model results using a convenient and somehow relevant contact scenario. The BGT model uses an asymptotic solution to find the ratio of the real contact area (A_r) to the nominal contact area (A_n) of rough surfaces at low loads. The formula for calculating the ratio of contact areas is expressed in Eq. (4).

$$\frac{A_r}{A_{nf}} = \frac{\kappa}{\sqrt{\langle|\nabla h|^2\rangle}}\frac{\overline{p}}{E^*} \tag{4}$$

where κ is the proportionality constant equal to $\sqrt{2\pi}$, $\sqrt{\langle|\nabla h|^2\rangle}$ is the root mean square (RMS) of the rough surface gradient calculated from the AFM measurements of only the structured surface (top surface), $\overline{p}$ is the average pressure and E^* is the effective Young's modulus. The main parameter of the BGT model is the root mean square (RMS) of the surface gradient which is calculated directly from the AFM scans. The other parameters are constant, considering using the same materials for all tests. Calculation of A_r from Eq. (4) was done by taking the maximum pressure applied to the contact zone (50 N). As the surfaces differed in their nominal contact area, the nominal pressure was also different. For the structured surfaces, the pressure was calculated by dividing the maximum normal load (50 N) by the feature contact area (A_{nf}). Table 4. 2 includes the nominal area of each feature contact area along with the nominal pressure calculated using $\overline{p}$= *50/*A_{nf}, as well as the RMS surface gradient. The values of $\sqrt{\langle|\nabla h|^2\rangle}$ and $\overline{p}$ for each feature contact area were used to calculate the ratio of the real contact area to the feature contact area in Eq. (4). Values of A_r (obtained from individual scans) for each sample category were then averaged. The mean A_r versus the feature contact area is shown in Fig. 4. 7 (a). A similar approach was performed for the BEM model. This approach implements a surface contact solver (https://contact.engineering) [147, 148] to estimate A_r. This was done by importing the whole surface data to the solver. Five values of A_r resulted from each sample category. These values were then averaged to obtain a single A_r per feature contact area ratio. The resulting A_r against A_{nf}/A_n is plotted in Fig. 4. 7 (b).

Table 4. 2. Input values of the parameters inserted in Eq. (4) to obtain the contact area ratio (E^*= 181 Gpa).

Feature contact area ratio	$\sqrt{\langle \lvert\nabla h\rvert^2 \rangle}$	A_{nf} (m^2)	$\overline{p}$ (N/m^2)
0.2	0.343956	0.00002	2.5 x 10^6
0.4	0.38552	0.00004	1.25 x 10^6
0.6	0.314884	0.00006	0.833 x 10^6
0.8	0.355556	0.00008	0.625 x 10^6
1	0.237276	0.0001	0.5 x 10^6

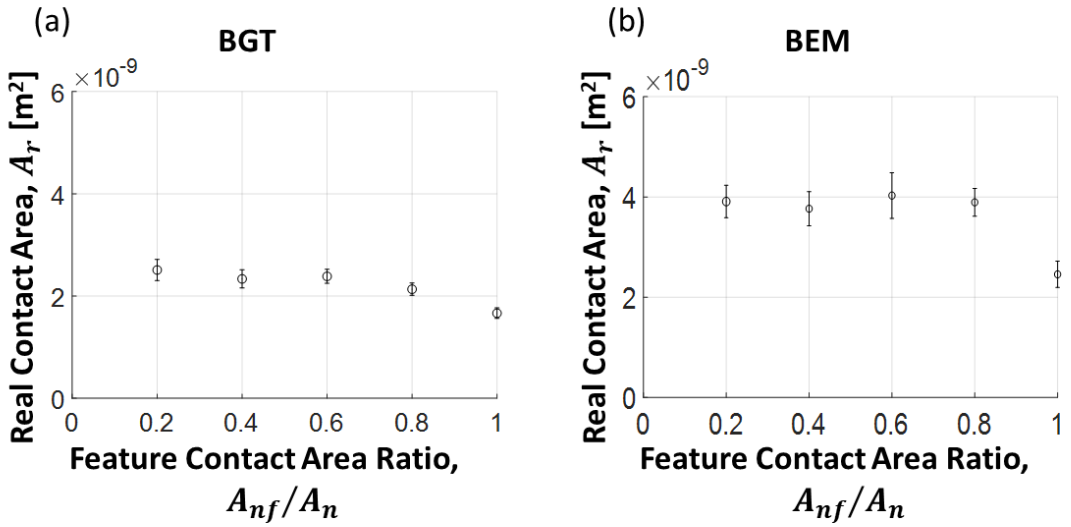

Fig. 4. 7. Predicted real area of contact A_r versus feature contact area ratio (A_{nf}/A_n) as estimated by (a) the BGT model and (b) the BEM method. Normal load P = 50 N. Nominal areas (i.e. 10 x 10 mm^2) and feature areas etc. are the same as for the experimental specimen.

Predictions of resulting A_r from the two modelling approaches showed a very similar trend which is also comparable to the trend in Fig. 4. 6. The analytical solutions that assumed the small contact pressure assured that manipulation of the feature contact area (A_{nf}) does not reflect on A_r and thus no change in friction can be seen. It can be said that manipulating the microscale contact area has the same effect on friction as adjusting the macroscale area (A_n), which means that friction is always independent of A_{nf}. However, Gachot *et al.* [14] have been able to tailor friction by adjusting the feature contact area. It is worth noting that they implemented laser lithography for fabricating the structured surfaces. Using laser for structuring surfaces is more likely to cause surface alterations, resulting in a high difference in surface roughness compared to the original nominal flat surface. The differences in surface topographies will highly alter friction, meaning that the possibilities of altering friction are largely dependent on the surface topographies rather than the feature nominal contact

area. In this study, highly flat silicon samples were structured using photolithography. This lithography technique roughly does not alter the surface topography (i.e. it does not really alter the surface in between the troughs). The structured surfaces were highly idealised square-wave patterns with nanoscale roughness on the tops of the features and the roughness on the feature tops was likely preserved. Consequently, tailoring friction by varying feature widths/contact area of the almost identical surface tops of the features was not possible as the independence of friction from the nominal contact area even holds for nanoscale roughness (or any scale). Therefore, the friction of such surfaces can only be tailored if the roughness is zero and can be done by adjusting the feature contact area according to $F = \tau_s A_r$. However, zero-roughness is practically impossible to exist. It should be noted that the unstructured case ($A_{nf}/A_n = 1$) deviated from the friction results of the structured cases. Interestingly, the experimental (Fig. 4. *6*) and analytical (Fig. 4. 7) results exhibited the same trend. The outlier point suggests that the topographies of the unstructured surfaces are different from the structured ones. This results in the observed difference in friction results between the two cases. The difference in surface topographies is believed to be attributed to the structured surfaces being subjected to the fabrication processes.

4.4. Conclusion

This study investigates the possibility of tailoring contact area and thus friction by producing microscale patterns with nanoscale roughness. The study performs sliding in a dry friction scenario on silicon surfaces that were obtained from commercial silicon wafers possessing high flatness and low roughness. The surfaces were structured using photochemical etching to produce micro square-wave patterns. The contact pair was always structured top samples against unstructured bottom samples, except in one case where the pair was unstructured as a reference. Sliding was initiated by pulling the bottom sample, whereas the top sample was held stationary. The micropatterns were designed by varying widths of the square-wave patterns with keeping the period constant at 100 µm to have different feature contact ratios between 0.2 to 1. Friction results have shown that Amontons' first law of friction (linear load-dependent relation: $F = \mu P$) was obeyed by both the structured and unstructured surfaces. Structuring the surfaces by varying feature contact area in the microscale resulted in the same friction response as changing the macroscale nominal contact area, showing the independence of friction on the feature contact area. This suggests that tailoring friction by manipulating the feature contact area seems to be impossible, indicating that the nanoscale roughness that existed on the unstructured surfaces and on the tops of the features on the structured surfaces was sufficient to confirm the independence of friction from the contact area. This is because surface topography was preserved even after varying the feature contact area. This means that the real area of contact in our contact scenario is only dependent on normal load. The experimental results

were joined with the BGT and BEM approaches to estimate the real contact area based on a fixed normal load and surface roughness measurement. Both approaches confirmed that the real contact area was unchanged with manipulating the feature contact area if the normal contact pressure was sufficiently small. This assures that varying the feature contact area has the same effect on friction as the nominal contact area, obeying Amontons' second law. Interestingly, the structured and unstructured cases still obey Amontons' laws even for nanoscale roughness which demonstrates their applicability on a wide spectrum of roughness length scales.

In conclusion, our highly idealised surfaces ruled out the possibility of altering friction by varying the widths of the features. However, as stated before, a previous study [14] has shown that patterning can adjust friction response. This is most probably attributed to the specific surface topography involved (i.e. if the patterning produces changes in surface roughness and produces changes in topography that lead to changes in real contact area). The friction results of our surfaces can be useful for applications where maintaining a certain friction level and decreasing nominal contact area is needed. This is seen in heat transfer applications where channels are required to dissipate heat from a sliding contact.

This concluded the static friction study on the structured interfaces in the unidirectional sliding. It was an encouraging attempt to examine the reliability of the friction rig which paved the way to expand the study of static friction in reciprocating sliding to fill the gap in knowledge in finding the reason for the disappearance of the static peak in reciprocating sliding. The following chapter will address this topic in detail.

Chapter 5: The static friction peak in reciprocating sliding

5.1. Introduction

Moving from the unidirectional sliding, the disappearance of the static friction peak in reciprocating sliding is a distinctive feature that requires investigating, utilising the same friction rig. In unidirectional sliding, the force required to initiate sliding is often less than the force needed to continue sliding. This gives rise to what we call the static friction peak. However, as was noted in Chapter 2, the static friction peak is generally absent in results from reciprocating sliding tests. Therefore, this chapter explores the question of its existence in reciprocating sliding. Fig. 5. 1 shows a unidirectional sliding curve with a clear static peak. The reason for its absence in published results from reciprocating sliding tests has not really been investigated previously.

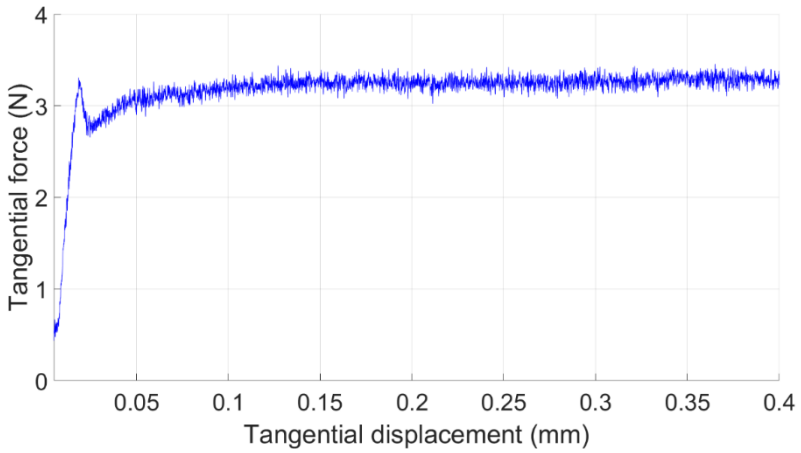

Fig. 5. 1. Unidirectional sliding curve between silicon surfaces under 30 N normal load (Adapted from Bin Jaber et al [149]).

To understand the presence of the static peak in reciprocating sliding, it is vital to firstly discuss the transition from static to kinetic friction in unidirectional sliding. It has been previously suggested in the past chapters that static friction is commonly higher than kinetic friction, giving rise to the so-called "static peak". The higher magnitude of the static friction in some cases can be attributed to the static contact before sliding (frictional ageing) [150]. In this case, more asperities are engaged over time which grows the real contact area causing a higher magnitude of friction [151-153]. Once reaching the maximum resistive force (static friction), the real contact area reduces and thus friction force relaxes to a steady value. Recalling the Bowden and Tabor [13] formula of sliding contact ($F = \tau A_r$), to maintain the steady-state friction, the change in the real area should be accompanied by a change in the strength of the interface. It has been claimed that shear strength during "stick" is higher than the one when "sliding", causing a reduction in friction [154]. This can be correlated to strong chemical bonds formed in the stick stage which are then ruptured in the onset of sliding due to a weakened interface caused by mainly plastic deformation [20]. It has been indeed found by Li *et al* [150] that static contact in a silica-silica interface results in strengthening chemical bonds over time

which requires higher tangential force to overcome the (increased) static friction. This finding of Li *et al* was supported by friction tests between silica-diamond (hydrogen-terminated diamond) and silica-graphite interfaces where there is a very low probability of forming chemical bonds (inert surfaces) in the interface. It resulted that static friction approximately equalled kinetic friction with no observable difference (no static peak). It was argued (for a silica-silica contact) that this phenomenon is clearly observed in a nanoscale single-asperity contact where most of the ambient conditions have a low influence on the fractional interactions [150]. Interestingly, similar findings were obtained from a study performed by Weber *et al* [26]. Their study investigated this assumption experimentally using a polystyrene sphere in contact with molecular pressure-sensitive film coated on a glass plate. They argued that there was not a reduction in the real contact area while sliding takes place indicating that the difference between static and kinetic must be originated from the chemical bond formation in these two stages (i.e. the interface was weakened in the sliding stage). The assumptions that attribute the friction drop on the onset of sliding to the shear-induced reduction in the real contact area or the rupture of chemical bonds seem rational and they may even mutually contribute to the friction drop. In fact, it can be said that the exact explanation of the transition mechanism is dependent on the contact scenario including material pair and ambient conditions etc. Reciprocating sliding test results are usually characterised by frictional hysteresis loops (plots of the tangential force against the relative sliding displacement). Fig. 5. 2 shows typical reciprocating sliding curves obtained from [115] where there is no distinguishable static peak in the loops as is commonly observed in the literature.

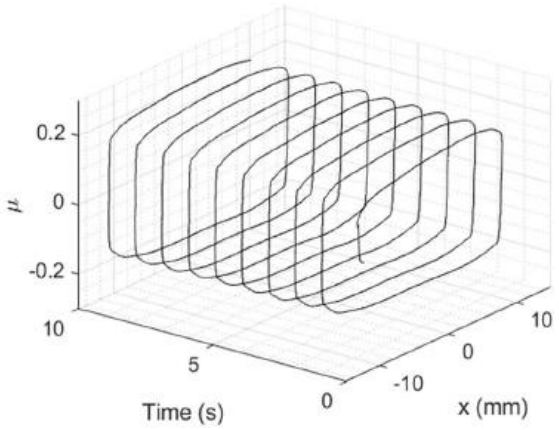

Fig. 5. 2. Representative reciprocating sliding curves of friction between PTFE and PA66 [115].

This chapter concerns the presence of the static peak in the friction hysteresis loops via the gross-slip fretting scenario. The aim of this study is to investigate the reasons for not observing the static peak in reciprocating sliding via experiments performed on smooth silicon samples with nanoscale

roughness (< 1 nm) in combination with an accompanying friction model of the transition from stick to slip developed by Xu *et al.* [155]. The model was implemented to aid in interpreting the experimental results. Indeed, part of the work here is to identify the conditions under which a static friction peak *is* observable in reciprocating sliding. The following sections of this chapter will describe the experimental and modelling approach followed by a detailed discussion of the experiment and model results.

5.2. Experimental procedure

A description of the rig has been presented in detail in Section 3.3 (Refer to Fig.3. 2 for the schematic of the rig). Briefly, the rig was used to investigate the sliding contact of silicon surfaces in a flat-on-flat contact scenario. The silicon surfaces used in this study are identical to the unstructured samples used in Chapter 4. The surfaces possess a high degree of flatness with nanoscale roughness. The contact zone involves top and bottom silicon surfaces that are unstructured and bonded to metal blocks. Dimensions of the top and bottom surfaces are 10 x 10 mm^2 and 15 x 20 mm^2 respectively. The bottom sample was large to gain more freedom in the sliding distance and avoid edge effects. The normal load was applied through compression springs and transmitted through an x-shape arm towards the top sample. Normal and tangential load were measured accurately via a commercial button load cell and a commercial universal tension/compression load cell. Measurement of forces and motion control was done in a LabView program.

The tests were performed on silicon samples that experienced sliding for 100 cycles with a 10 N normal load. The sliding distance for each stroke was 0.5 mm (1 mm full cycle) with a sliding speed of 0.05 mm/s (corresponding frequency is 0.05 Hz). The initial idea to investigate the disappearance of the static peak was to vary the static contact time at the end of each stroke (dwell time). This was inspired by studies carried out in Refs [26] and [150] where the contact time had a direct impact on the magnitude of the static peak. Varying the dwell time was an additional step added to the test parameters stated earlier, except for the number of cycles which was only 10 cycles for each dwell time. The change in sliding direction when reaching the edge of the interface was stalled for some time periods to observe the effect of the static contact time on the static peak. The stalling time was adjusted in the LabView code before sliding takes place, so there was no user interference after running the code. The time range was from zero to 20 seconds. The study was then directed to sliding with no dwell time. The tests were repeated five times on a different sample pair possessing almost identical surface conditions. Prior to testing, silicon samples were cleaned using a cleaning procedure that involves five-minute dipping in Acetone then IPA and finally DI water. The samples were then blown dry by a N_2 gun. Following sample cleaning, surface roughness was measured in an AFM to establish the intact condition of the surface before being affected by wear. The cleaning procedures

were carried out again after surface measurement and before performing the test. These preparation steps were done on the five different silicon sample pairs. After the tests, the tested samples were scanned in the AFM to measure the roughness of the worn surfaces.

5.3. Adhesive friction modelling approach

5.3.1. Theoretical background

A friction model recently developed by Xu *et al.* [155] has been used to help interpret and understand the results. The model assumes that an elastic nominally flat rough surface slides on a rigid flat surface which was the same assumption used in the model work of Chapter 4. The aim again was to qualitatively compare the experimental results with the model via applying a simple contact condition to ease understanding the friction behaviour. The model is developed to predict the evolution of the interfacial friction, F, normal load, F_z, and real contact area, A_r as sliding transitions from full stick to full sliding. It attributes the transition from stick to slip to the fracture on the contacting asperities based on the Papangelo and Ciavarella model [156]. The model explains the interfacial friction at the asperity level as a result of the coupling between the adhesion and tangential load. To implement the prediction at the asperity level into the macroscale contact, the adhesive model assumes a Gaussian distribution of asperity heights (z), which is represented by $\emptyset(z) = \frac{1}{\sqrt{2\,\pi\,\sigma_s^2}} \exp(-\frac{z^2}{2\,\sigma_s^2})$, where $\sigma_s = \sqrt{\langle z^2 \rangle}$ which is the root mean square (RMS) of asperity heights, that follows the classical multi-asperity model. It predicts the macroscale friction, normal load and real contact area (i.e. F, F_z and A_r respectively) by summing the contribution at the asperity level of tangential forces, normal loads, and real contact areas (i.e., T, P, πa^2 respectively). The present model is capable of qualitatively predicting the main characteristics of a friction test, namely static friction peak and reduction in real contact area caused by shear.

The predictions of the macroscale parameters are derived according to the following formulas:

$$F_z(d,\delta_T) = \eta A_n \int_{\delta_2}^{\infty} P_{PC}(\delta,\delta_T)\,\phi(d+\delta)\,d\delta + \eta A_n \int_{\delta_1}^{\delta_2} P_{Hertz}(\delta)\,\phi(d+\delta)\,d\delta \tag{5}$$

$$F(d,\delta_T) = \eta A_n \int_{\delta_2}^{\infty} T_{PC}(\delta,\delta_T)\,\phi(d+\delta)\,d\delta + \eta A_n \int_{\delta_1}^{\delta_2} T_{Hertz}(\delta)\,\phi(d+\delta)\,d\delta \tag{6}$$

$$\begin{aligned} A_r(d,\delta_T) = {} & \eta A_n \int_{\delta_2}^{\infty} \pi a_{PC}^2(\delta,\delta_T)\,\phi(d+\delta)\,d\delta \\ & + \eta A_n \int_{\delta_1}^{\delta_2} \pi a_{Hertz}^2(\delta)\phi(d+\delta)\,d\delta \end{aligned} \tag{7}$$

These formulas are divided into two integral forms that represent the contribution of *P*, *T*, πa^2 at the asperity level in the stick and sliding stages that are governed by Papangelo and Ciavarella (PC), and Hertzian contact theory respectively. The terms δ and δ_T are the asperity displacements in the normal (indentation) and tangential directions. The separation between the surfaces is termed as d. Value of indentation is determined by $\delta = z - d$. The contact pair experiences the tangential displacement in a quasi-static manner (from 0 to 1x 10^{-7} m with 30 steps). The transition between the three sliding stages (non-contact, stick and slip stages) is associated by the integral limits δ_1 and δ_2 which represent the critical indentation depths (see Eqs. (12) and (13)). To integrate these contributions to the macroscale level, the asperity density η is multiplied by the nominal contact area A_n (10 x 10 mm^2). Knowing (δ, δ_T), it is possible to solve the non-linear equations to get a_{PC}, P_{PC}, T_{PC},

$$\delta = \frac{a_{PC}^2}{R} - \sqrt{\frac{2\pi a_{PC} w}{E^*} - \frac{4}{9}\lambda\delta_T^2} \tag{8}$$

$$P_{PC} = \frac{4E^* a_{PC}^3}{3R} - \sqrt{8\pi E^* a_{PC}^3 w - \frac{16}{9}\lambda E^{*2} a_{PC}^2 \delta_T^2} \tag{9}$$

$$T_{PC} = \frac{4}{3}E^* a\ \delta_T \tag{10}$$

Where *R* is mean asperity radius (*R*), *w* is the work of adhesion, E^* is the effective Young's modulus and λ is the mode mixity parameter. All of these values that were used to obtain Eqs. (8) – (10) will be presented in Table 5. 2. The contributions of *P*, *T*, πa^2 in the sliding stage (Hertzian solution) are obtained using the following formulas

$$a_{Hertz} = \sqrt{R\delta}, \quad P_{Hertz} = \frac{4}{3}E^*\sqrt{R}\delta^{3/2}, \quad T_{Hertz} = \pi a^2 \tau_0 \tag{11}$$

The integral limits are determined as follows:

$$\delta_2 = \max(d_{min} - d + \delta_{JKR}^{loading}, \delta_{PC}^{min}) \tag{12}$$

$$\delta_1 = \min(0, \delta_2) \tag{13}$$

where d_{min} is the minimum mean separation at the beginning of the tangential loading stage,

$$\delta_{JKR}^{loading} = -2.641\mu_T^{\frac{3}{7}} \exp\left(-\frac{1}{2\sqrt{\mu_T}}\right) \quad (14)$$

$$\delta_{PC}^{min} = \frac{a_{min}^2}{R} - \sqrt{\frac{2\pi a_{min} w}{E^*} - \frac{4}{9}\lambda\delta_T^2} \quad (15)$$

The a_{min} is the unique real positive root of the following polynomial:

$$\frac{2\pi w}{E^*}a_{min}^3 - \frac{4}{9}\lambda\delta_T^2 a_{min}^2 - \left(\frac{\pi w R}{2E^*}\right)^2 = 0 \quad (16)$$

The term (μ_T) is the Tabor's parameter and is calculated by $\mu_T = (\frac{R\,w^2}{E^{*2}\,\varepsilon^3})^{\frac{1}{3}}$, where ε is the atomic distance, $\varepsilon = 0.2$ nm.

5.3.2. Model input parameters

The AFM scans of the silicon samples were the key parameters of the Xu *et al.* model [155]. The before and after testing scans describe the effects on the surface topography of the silicon samples by the reciprocating sliding. Three key parameters from these scans were extracted to be inserted into the model. They are the root mean (RMS) square of asperity height (σ_s), asperity density (η), and mean asperity radius (R). These values were dependent on the assumption that an asperity is recognised if its summit is higher than the four neighbouring sampling points. To measure the asperity density, the number of asperities (that were identified as the assumption above) was divide by the nominal contact area (A_n)= 10 x 10 mm^2. The mean asperity radius was approximated using: $R = \frac{1}{2}\langle|\partial z^2/\partial^2 x|^{-1} + |\partial z^2/\partial^2 y|^{-1}\rangle$. The parameters extracted from the before-test scans represent the intact condition of the sample surfaces. These parameters were extracted again for the after-test scans to obtain the condition of the affected surface topography. The model assumes σ_s to be the only variable during the friction test. The RMS of asperity height (σ_s) of the before-test scans are assumed to be for Cycle 1 and the values of the after-test scans are for Cycle 100. The cycles in-between were approximated by using linear interpolation to investigate the effect of wear on surface roughness during sliding.

The model also requires inputs of the mechanical properties of the interface. The mechanical parameters required are Young's modulus E, shear strength τ_0, and Poisson's ratio v. These parameters were obtained from the literature [157, 158] as E = 169 GPa, τ_0 = 10 GPa, and v = 0.272. An effective Young's modulus was then calculated as:

$$E^* = E\ /\ (1 - v^2) \quad (17)$$

Additionally, it is important to consider the work of adhesion (surface energy) of the silicon surface before obtaining the model results. The surface free energy is characterised by the state of the equilibrium of the atoms on the surface [159]. It is defined as the required work to produce a new surface of material [159]. There are characteristics that are strongly affected by the surface free energy which are adsorption, wetting and adhesion [159]. Measuring the surface free energy of solids experimentally is rather difficult. Researchers rely on using theoretical approaches incorporating contact angle measurements of an interface between liquids and a solid surface (indirect method) to inspect the interaction at the interface. The interaction at the interface is essentially determined by the properties of the liquids involved and the target solid surface. The surface energy measurement originated from the widely known Young's equation for a liquid-solid interface. The equation includes the influencing components of the interaction. The equation that expresses the liquid-solid interface is as follows:

$$\gamma_l \cos(\theta) = \gamma_s - \gamma_{ls} - \pi_e \tag{18}$$

where γ_l , γ_s and γ_{ls} are the surface tension of the liquid, the surface tension of the solid and interfacial surface tension respectively. The last term (π_e) is the equilibrium film pressure. This term is usually zero when using liquids with higher energy than solids [160]. The higher energy of the liquid can be anticipated if a liquid droplet drops on a solid surface (low-energy surface) and forms a contact angle [160]. This assumption does not apply to solids with high energy such as metals and graphite [160]. The terms that can be determined experimentally in the Young equation are the contact angle (θ) and surface tension of the liquid. Researchers have been able to measure the surface tension of most liquids. Therefore, the contact angle is the only variable that needs measuring. Fig. 5. 3 illustrates the interactions seen on the liquid-solid interface determined by Young's equation. Fowkes [160] modified Young's equation to include the dispersion forces of the system and it is written as:

$$\cos(\theta) = -1 + 2\sqrt{\gamma_s^d}\left(\frac{\sqrt{\gamma_l^d}}{\gamma_l}\right) \tag{19}$$

The γ_s^d and γ_l^d are the dispersion components of surface tension of the solid and liquid respectively. It has been shown that there are two forces (components) namely dispersion and polar (hydrogen bonding; γ_l^p) that form the surface tension of a material [161]. Consequently, the formula was further modified to add both contributions to the equation. The modified (more general) form is:

$$1 + \cos(\theta) = 2\sqrt{\gamma_s^d}\left(\frac{\sqrt{\gamma_l^d}}{\gamma_l}\right) + 2\sqrt{\gamma_s^p}\left(\frac{\sqrt{\gamma_l^p}}{\gamma_l}\right) \quad (20)$$

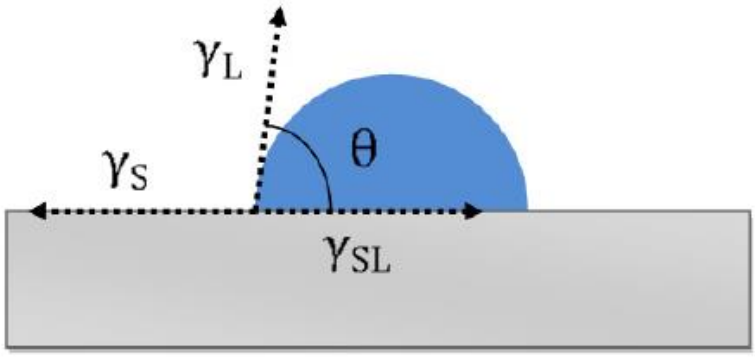

Fig. 5. 3. The components that affect the liquid-solid interface according to Young's equation [159].

In the liquid-solid interface, these two components are the basis of liquid-solid interaction and determine the wettability of the interfacial region [160]. The level of wettability is dependent on the viscosity of the liquid and the surface roughness of the solid [162]. Liquids with a predominant dispersion contribution tend to spread freely on the solid surface [159]. In the liquid-solid interface, a widely known term that was first introduced by Zisman [162] defined as the critical surface tension was determined after an extensive study on different liquid-solid interfaces. The study [162] investigated the cosine of the contact angle against the surface tension of the liquid. It was found that data points from all interfaces can be fit by a linear line with y-intercept at $\cos(\theta)$= 1 (θ = zero). The value of the surface tension where there is no contact angle is considered the critical surface tension of the solid surface. This means that liquids with surface tension less than the critical value are freely spread over the solid surface. It should be noted that the critical value is influenced by the surface composition, thus it needs to be determined experimentally (i.e. it is not a given property). This finding can be used to examine the wettability of a solid surface. Measurement of the surface energy through the contact angle have been applied via multiple theoretical approaches. The most common methods are the method of Zisman [162], the geometric mean (i.e. Owen, Wendt, Rabel and Kaelble) [161] and the harmonic mean [159]. Even though these methods are somehow different in their theoretical approaches, it has been found that similar values of surface energy are obtained [159]. This indicates that choosing one of these three methods should be reliable to obtain surface energy.

The work of adhesion (surface energy) in this work was measured experimentally on the intact silicon surfaces using the Owens, Wendt, Rabel and Kaelble (OWRK) method [161]. The surface energy was calculated by measuring the contact angle of liquid droplets from water, ethanol and ethylene glycol

on the silicon surface. The surface tensions of these liquids were obtained from Refs [159] and [163]. The liquid total surface tension (γ_l), was a summation of two components, dispersive (γ_l^d), and polar (γ_l^p). These values are presented in Table 5. 1. The surface energy was then obtained by fitting a line between points resulting from Eqs. (21) and (22) representing the *x*-and *y*-axis respectively.

$$x\left(\gamma_l^p, \gamma_l^d\right) = \sqrt{\frac{\gamma_l^p}{\gamma_l^d}} \tag{21}$$

$$y\left(\theta, \gamma_l, \gamma_l^d\right) = 0.5 * (1 + \cos(\theta)) * \left(\frac{\gamma_l}{\sqrt{\gamma_l^d}}\right) \tag{22}$$

The surface energy of silicon is the total of the dispersive and polar components which correspond to the slope and *y*-intercept of the fitted line. The components of the linear equation were raised to the power 2 and summed to obtain the total surface energy of silicon.

Table 5. 1. Total surface tension, dispersive surface tension and polar surface tension of the liquids used in the measurement of surface energy obtained from [159] and [163].

Liquids	Surface tension - total (γ_l) (mN/m)	Surface tension - dispersive (γ_l^d) (mN/m)	Surface tension - polar (γ_l^p) (mN/m)
Water	72.8	21.8	51.0
Ethanol	21.4	18.8	2.6
Ethylene glycol	48	29	19

A high-resolution camera was used to capture the droplets from leaving the pipette until they touch the silicon surface. The contact angle was measured from images taken after one second of releasing the droplet and then processed in ImageJ software. Shapes of these droplets (all have the same volume) are shown in Fig. 5. 4. The highest contact angle was obtained from water droplets as they occupied the smallest area on the silicon surface. This is because water possesses the highest surface tension among the other used liquids (as shown in Table 5. 1). Ethanol occupied the largest area on the silicon surface, thus the lowest contact angle was measured from ethanol droplets (i.e. freely spread on the silicon surface). To ensure repeatability, three contact angle measurements were applied on three different silicon samples. The average from these measurements was used to calculate the total average surface energy of the intact silicon surfaces at 42.8 mJ/m^2. As the two surfaces were almost identical, the work of adhesion was multiplied by 2 (i.e. w = 85.6 mJ/m^2). By

knowing the surface energy of the silicon surface and comparing it with the surface tension of the liquids in Table 5. 1, it can be understood why the droplets of liquids were in different shapes. The large difference in the contact angle seen in the liquid-solid interfaces followed the suggestion obtained from Fowkes [160] where the contact angle is determined by the relative relationship between the surface tension of the liquid and the surface energy of the solid. A good representation of this relationship was illustrated by Prakash and Prasanth [164] and is shown in Fig. 5. *5*. For example, when relating the surface tension of ethanol with silicon, the small contact angle can be anticipated due to having a liquid with low surface tension and relatively high surface energy of solid.

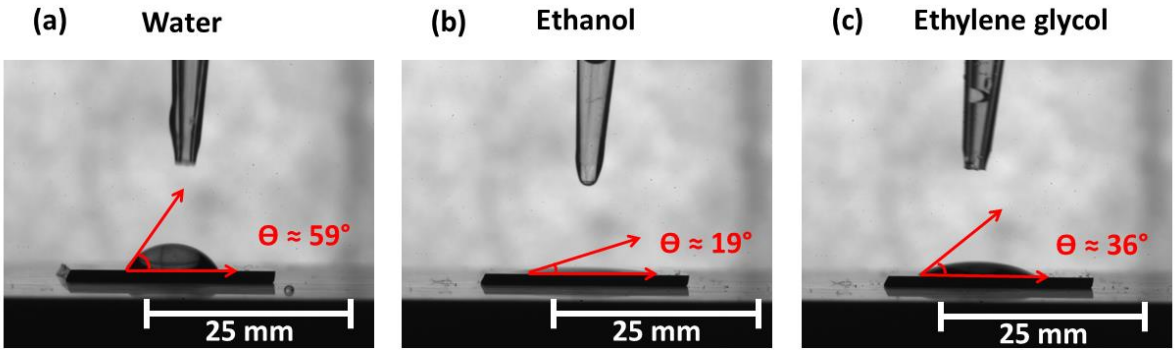

Fig. 5. 4. Contact angle measurements on silicon samples performed to calculate the surface energy of the silicon surface.

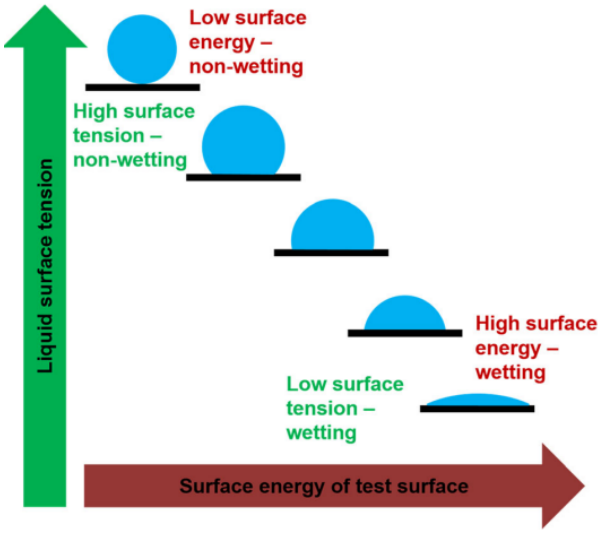

Fig. 5. 5. The relative relationship between the liquid surface tension and the surface energy of a solid [164].

Having managed to explain the model approach and provide the necessary formulas, a table of inputs (see Table 5.2) should be inserted to ease understanding the parameters usage in the model. The table involves the parameters that were dependent on the sliding cycles, surface conditions etc. (e.g σ_s, η, and R). It is worth saying again that the only variable to obtain the results in the model for the different

samples was σ_s. The constants (e.g. E^*, τ_0, ν) that were used for all the model results are presented in the caption of the table.

Table 5. 2. Roughness inputs used to extract the model results. These parameters were accompanied with a list of constants as follows: E^*= 181 GPa, τ_0= 10 GPa, ν= 0.272, w= 85.6 x 10^{-6} mJ/mm^2, $\lambda = 0.22$ and $\varepsilon = 0.2$ nm.

No. of samples	Roughness parameters						Tabor's parameter (μ_T)
	Cycle 1			Cycle 100			
	σ_s (x10^{-6} mm)	η (x10^8 mm^{-2})	R (x10^{-6} mm)	σ_s (x10^{-6} mm)	η (x10^8 mm^{-2})	R (x10^{-6} mm)	
1st	0.118	1.28	0.559	26.9	1.28	0.559	2.50
2nd	0.221	1.33	0.802	35.4	1.33	0.802	2.82
3rd	1.09	1.14	0.586	27.2	1.14	0.586	2.54
4th	0.473	1.14	0.394	28.3	1.14	0.394	2.25
5th	0.361	1.03	0.672	22	1.03	0.672	2.66

5.4. Results and discussion

A waiting time after each stroke was introduced to inspect whether the contact time has an impact on the static peak. Initially, it was considered that the disappearance of the static peak in the literature on reciprocating sliding might be attributed to insufficient contact time to form the bonds between the opposing surfaces. The idea was to force the surfaces to relax for a specific time and then allow them to slide again. The tests started with carrying out sliding with no dwell time to mark the sliding curves of this condition as a reference. The dwell time was increased from 2 to 20 seconds. The sliding curves with varying dwell time are presented in Fig. 5. 6. It is noticeable that the static peak was seen in almost all the sliding cycles. Static friction was always higher than kinetic friction. This can be correlated to a weakened interface at the onset of sliding (gross slip), or a reduction in the real contact area when the sliding regime transited to the gross slip. This will be discussed in detail later in this section. It was suggested that chemical bonds are formed during the static contact (keeping the surfaces in contact with no sliding) leading to increase the static friction from its original value [150]. In our study, the static peak seems to maintain its magnitude throughout sliding regardless of the waiting time. The magnitude of the static peak even reduced slightly in the later cycles of the 20-second dwell time test. It is interesting to note that the sliding curves were uniform throughout the reciprocating sliding (for the forward and backward sliding). The kinetic region of the sliding curve was stable, which might indicate that wear did not evidently contribute to the frictional behaviour. The

existence of the static peak in all cycles is worth investigating as this was not observed in the literature on reciprocating sliding. Realising that there was not a clear impact of the contact time on the static peak on the tested surfaces, the study was re-directed to further investigate the existence of the static peak by applying a high number of sliding cycles with no dwell time. It was found that imposing the interface for 100 sliding cycles seemed reasonable and can provide adequate details of the silicon frictional behaviour in the reciprocating sliding. The insensitivity to dwell time may be due to the fact that silicon is not a material noted for any appreciable creep behaviour (therefore real contact area is not expected to increase with time) and also, the timescales needed to fully establish bonds are likely to have been far less than the range of dwell times considered here.

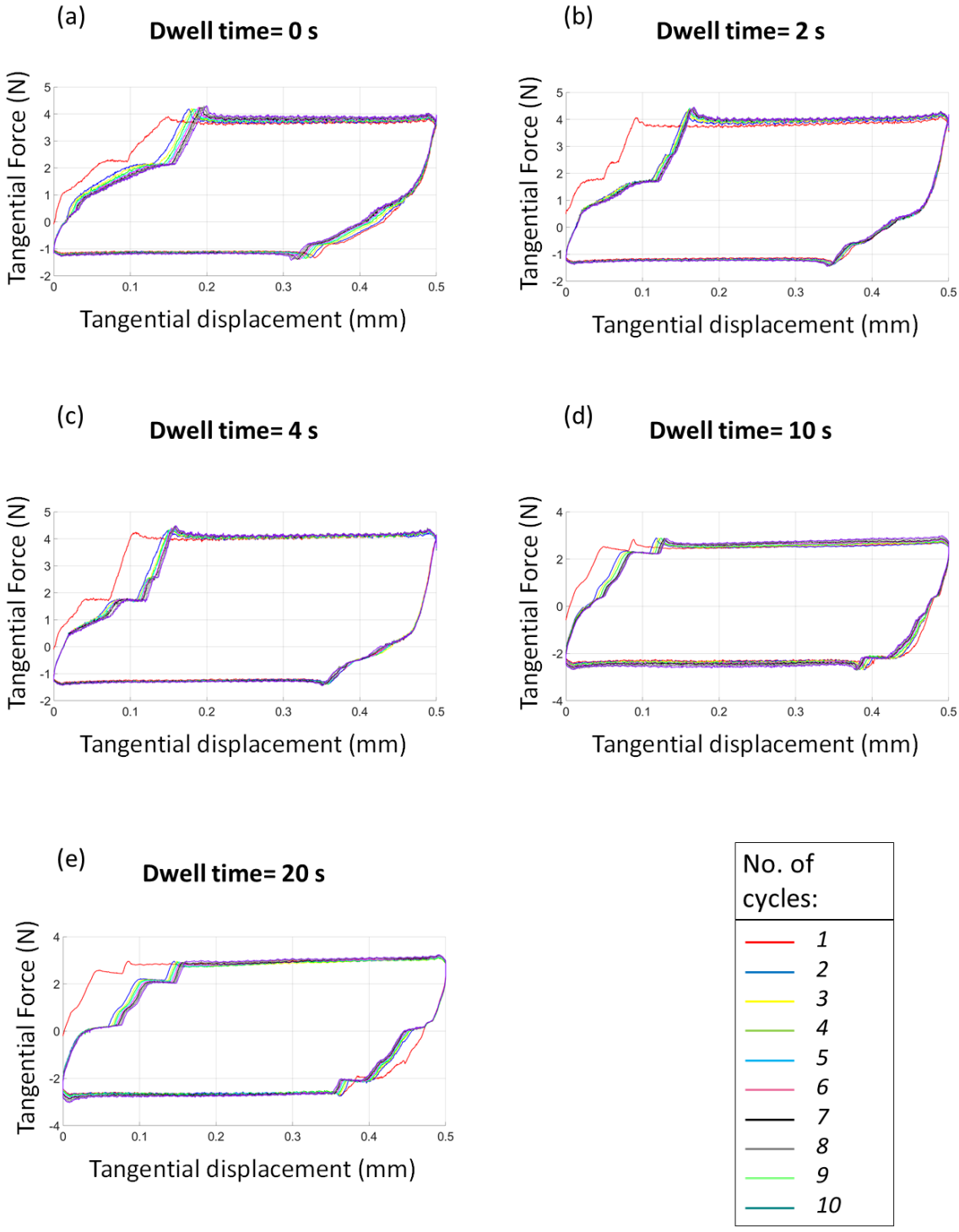

Fig. 5. 6. Experimental sliding curves with varying dwell time: (a) no dwell time, (b) Dwell time = 2 seconds, (c) Dwell time = 4 seconds, (d) Dwell time = 10 seconds and (e) Dwell time = 20 seconds. The legend shows the colours that represent the number of cycles. The dwell time refers to the time for which the contact is held static at the end of each sliding stroke.

To correlate the surface condition of the tested samples with friction results, roughness measurement of the silicon samples performed before and after testing is presented in Table 5. 3. The prior-test

values are the lowest limit of the mean RMS roughness (*Rq*) and RMS asperity height (σ_s) that the samples can attain. It is noticeable that there is some variation in *Rq* and σ_s among samples in the prior test scans. This is more likely to be related to how the samples were initially prepared before scanning. It can be also seen that there is a considerable difference between the pre-test and post-test scans. This is most probably attributed to wear sustained during the reciprocating sliding. Wear tracks were evident on the surfaces after detaching them. Wear appears to have increased the roughness to significantly high values compared to the before-test scans. The post-test scans are in the range between 28 to 35 nm, whereas the maximum *Rq* in the pre-test scans is 0.64 nm (i.e. the after-test scans are almost 50 times higher). Roughness values after testing indicate that the samples experienced a similar level of wear. It is also noteworthy that the standard deviation of *Rq* after the test is remarkably high. The significant variation of *Rq* in a single surface indicates that some areas were severely damaged, whereas others were almost unaffected.

Table 5. 3. Average RMS roughness *Rq* and average RMS asperity peak height σs for silicon samples before and after 100 cycles of reciprocating sliding (bracketed values are standard deviations).

No. of samples	RMS Roughness *Rq* (nm)		RMS asperity peak height σ_s (nm)	
	Before	After	Before	After
1st	0.16 ±0.004	28.9 ±42.0	0.12 ±0.003	26.9 ±44.4
2nd	0.17 ±0.07	35.8 ±48.9	0.22 ±0.20	35.4 ±51.6
3rd	0.64 ±0.44	29.1 ±52.8	1.09 ±0.9	27.2 ±52.8
4th	0.32 ±0.04	31.3 ±47.1	0.47 ±0.07	28.3 ±48.1
5th	0.31 ±0.27	27.8 ±43.8	0.36 ±0.30	22.01 ±39.8

Fig. 5. 7 (a) shows representative curves of the forward sliding of friction hysteresis loops from the experiment. The forward sliding of the loops was only presented in the figure because it is preferable to focus on one sliding direction to help investigate the static peak. Full sliding curves are shown in Fig. A 23 in the appendix. To better investigate the appearance of the static peak, curves of cycles up to 12 with 0.25 mm sliding displacement were selected. These cycles aid in highlighting the static peak appearance throughout cycling. The peak was distinguishable from Cycle 1 until a few subsequent cycles. The static friction then reduced towards kinetic friction leading to the absence of the static peak (i.e. static Friction ≈ kinetic friction) with no notable change in the sliding curves towards the end. Sliding curves have exhibited a slight shift with cycles before transitioning from pre-slip to gross slip. This is believed to be caused by a limitation in the experimental setup. The curves also showed temporary suspension of the linear increase in the tangential force in the partial slip stage starting

from Cycle 6. The reason for the suspension is not yet clear. However, these two events did not affect the results of the loops. Noticeably, all curves showed the typical relaxation of the tangential force to a stable value (kinetic friction, F_k).

The almost identical curves (i.e. the decay of the peak was the only distinctive feature) of the loops suggesting that wear could be the key element responsible for decaying the static peak. For this reason, the wear-dependent surface roughness was inserted in the model for each cycle to validate the assumption of the wear effect on the corresponding cycles. Sliding curves of silicon surfaces from the model are shown in Fig. 5. 7 (b). They are based on roughness data and mechanical properties of the same sample shown in Fig. 5. 7 (a). It should be noted that roughness parameters were the only variable for the sliding curves of the model. The model shows similar results to the experiment concerning the static peak appearance and static friction reduction. The figure confirms the appearance of a prominent static peak in the early sliding cycles. It is observed that the peak also reduced rapidly with cycles, as shown in the experiments. Also, the kinetic friction level for the experiment and model at Cycle 1 both were at 3 N suggesting that the value of τ and the prediction of A_r in the model are probably accurate. This is supported by recalling the well-known sliding friction equation of Bowden and Tabor ($F = \tau A_r$) [13]. However, this was not the case for the subsequent model cycles. Here, it is suggested that the experimental interfacial shear strength might be changing with cycles to maintain F_k as shown by Rabinowicz [52]. Therefore, it can be said that the experimental τ and A_r were altering with cycles to keep F_k constant. A_r is commonly known to reduce with increasing surface roughness [92, 116]. The interfacial shear strength is believed to increase with cycles due to a strengthened interface. In the model, F_k was the result of the decrease in A_r without considering the change in τ with cycles which results in the reduction in F_k. This is probably the cause for the difference between the model and the experiment for curves after Cycle 1. It can be noticed that the magnitude of static friction (F_s) is also decreasing with cycles. This occurred in the experiment until a certain limit (F_k), whereas F_s in the model kept decreasing with cycles as observed in F_k. The large difference between the experiment and model in F_s might be attributed to the complexity of the multi-asperity approach on fracture at the asperity level which makes it difficult to obtain accurate implementation in the macroscale interaction.

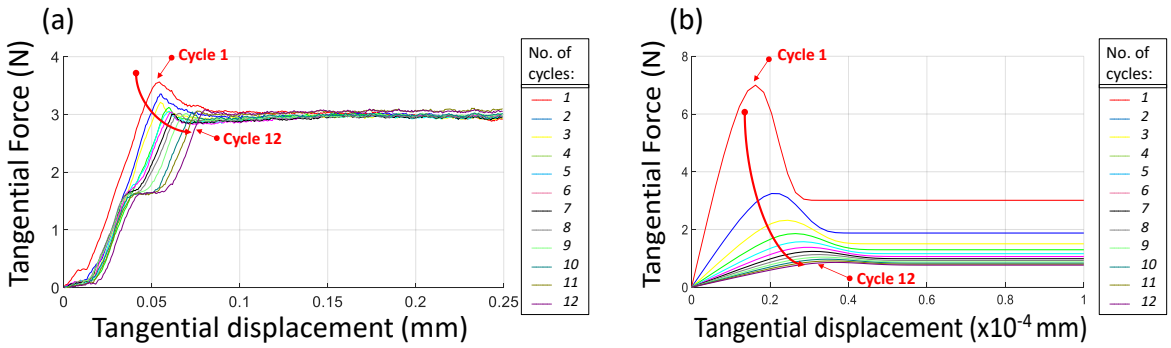

Fig. 5. 7. Representative sliding curves from (a) experiment and (b) model prediction illustrate the static peak evolution with cycles. The experiment graph shows only the forward direction to help compare with the model prediction. The sliding curves of the model were obtained using the same constants presented in the caption Table 5.2 in addition to $\mu_T \approx 2.50$, $\eta = 1.28 \times 10^8$ mm^{-2}, $R = 0.559 \times 10^{-6}$ mm (related to the 1st sample in Table 5.2). The values of σ_s were dependent on the cycle number (e.g. σ_s for cycle 1 was 0.18 x10^{-6} mm, while σ_s for cycle 12 was 3.1 x 10^{-6} mm) and they were altered accordingly.

To quantify the magnitude of the static peak from the experiment results, the difference between F_s and F_k was divided by F_k (relative difference) and then plotted against cycles (Fig. 5. 8 (a)). Obtaining the relative difference helps to inspect the peak magnitude relative to F_k (i.e. how the static peak is fading with cycles). Data points of this relationship are joined with the best-fitted exponential curve to present the trend. The equation of the fitted curve is inserted in the figure. All samples follow an exponential decay with a higher difference in the first cycles, reflecting the higher peaks. The static and kinetic friction started to be equal from about Cycle 15 for almost all samples corresponding to the beginning of the static peak disappearance. The different behaviour of the samples in the early stage of sliding might be attributed to a different reaction from samples in the running-in stage. After approximately 30 cycles, all samples converge to the zero-difference stage where similar sliding curves with no static peaks were observed. The average of $\Delta F/F_k$ is plotted versus cycles in Fig. 5. 8 (b) with a maximum average peak magnitude of 20% of F_k.

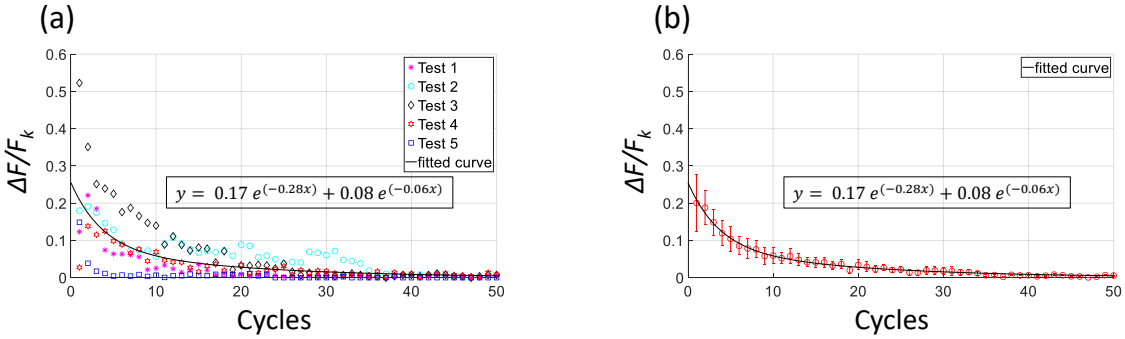

Fig. 5. 8. The relative friction difference (ΔF/Fk) versus cycles for (a) the five tests and (b) the average. The inset equation is for the best-fitted curve.

Once more, $\Delta F/F_k$ was obtained to explore the trend for the model results. This is shown in Fig. 5. 9 (a). The figure involves the results of selected cycles in which a distinction between F_s and F_k can be observed. The results after cycle 20, where $F_s = F_k$, are included to show how the trend proceeds towards the end. From the graph, the difference in Cycle 1 between individual samples is high compared to the other cycles. This indicates different responses from the samples at the beginning of sliding. From Cycle 5, the samples started to converge to the same ratio until they are all in the zero-difference. It can also be seen that the model results follow the exponential decrease similar to the experiments, but with a better agreement between samples results. To have a clearer idea of the difference between the model and empirical results, averages of the ratio from both phases were plotted against cycles in Fig. 5. 9 (b). Encouragingly, ratios from the model started to coincide with those of the experiments from Cycle 5 towards the end assuring the friction behaviour observed in the experiment.

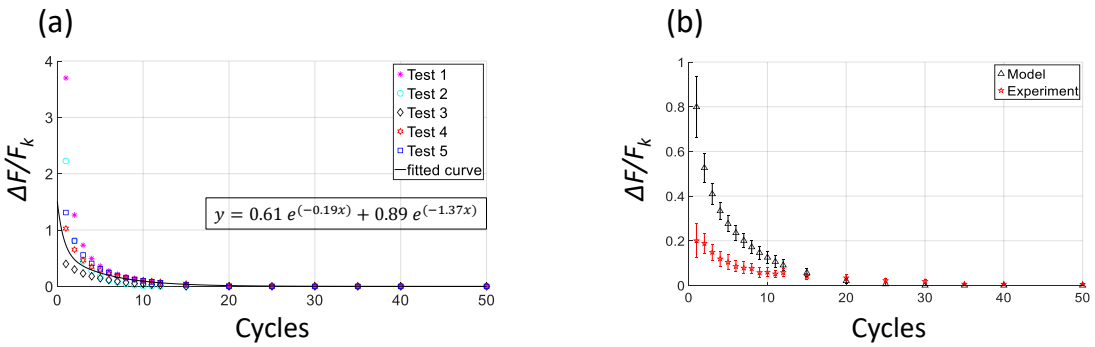

Fig. 5. 9. Predictions of the model of the relative friction difference (ΔF/Fk) versus cycles for (a) individual samples and (b) a comparison between experimental and model averages.

To obtain more explanation of the sliding curves, particularly the friction drop (F_s to F_k) in Fig. 5. *7*, the prediction of real contact area (A_r) was acquired from the present model. Here, the model explains the friction drop as a result of a reduction in the real contact area due to the increase in surface roughness (see Table 5. 3). Fig. 5. 10 shows the evolution of real contact at Cycle 1 on one of the contacting pairs. The figure illustrates the contribution of the stuck and sliding regions on the total A_r (Eq (5)). They mutually contribute to the total real contact area. The summation of their contributions gives rise to the frictional behaviour observed in Fig. 5. *7* (b). As the sliding displacement initially increases, the real contact area in the stuck regions is dominant and high, corresponding to the higher static friction, which is followed by a decrease, marking the transition from stick to slip at around 0.2 x 10^{-4} mm. This reduction continues until the entire interface slips (gross slip), where the slip regions become dominant leading to lower kinetic friction. The reduction in the real contact area during sliding explains the friction drop. The model also attributes the higher static friction to the rupture of the stuck asperity junctions. This means that high work of adhesion of the interface would result in

stronger junctions, thus higher static peak as suggested in Xu et al. [155]. To investigate the reduction in F_s, the average real contact area in the stuck regions is plotted against cycles in Fig. 5. 11 (a). The graph shows an exponential decrease in the real contact area in the stuck regions with cycles, resulting in a reduction in F_s with cycles also as shown in Fig. 5. 11 (b). Interestingly, the reduction of F_s is in good agreement with the experimental data in Fig. 5. *7* (a), indicating that when surfaces are roughened, less static friction results due to a reduction in the real contact area.

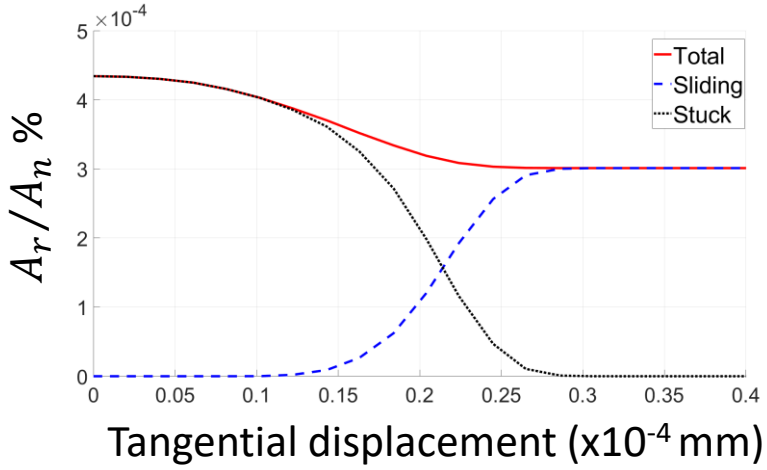

Fig. 5. 10. Normalised real contact area versus tangential displacement illustrating the stuck contribution (black :) and sliding contribution (blue --) to the total of the real contact area (red -). The graph shows the evolution of the real contact area at Cycle 1 of the sample results presented in Fig. 5. 7.

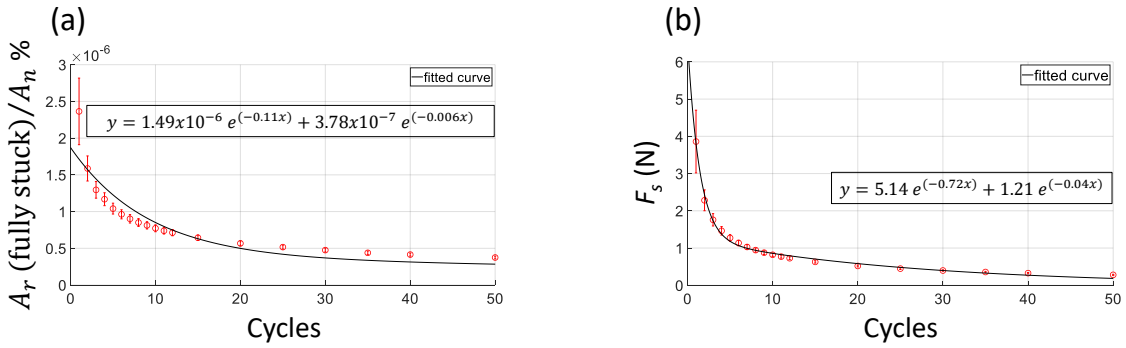

Fig. 5. 11. Averages of (a) real contact area in stuck stage normalized by the nominal contact area versus cycles and (b) static friction versus cycles as predicted from the present model with a fitted curve equation inserted.

Another plausible explanation for the reduction in F_s is the removal of third-body layers (molecules) from the interface. It is suggested that these molecules are formed when gases in the atmosphere are bonded to containment molecules on the interface such as H_2O [150, 165]. The existence of the third-body molecules can lock the contacting asperities, requiring higher tangential force to overcome the static friction. When the surfaces are rubbing each other, third-body layers that exist between the surfaces are ruptured and moved away from the interface. This is believed to be more pronounced in

the early stage of sliding. The following sliding cycles would wear away these molecules, resulting in lower static friction. The distinctive static peak from Cycle 1 to Cycle 12 suggests that wear-reduced real contact area and third-body removal are more likely to be the main reasons for the reduction in F_s, giving rise to 'burying' the static peak. It can be concluded that the static peak is obsecured after several cycles due to the reasons discussed above. This is probably the reason for not observing the static peak in the literature on the frictional hysteresis loops – as the reported loops are generally those that occur well after the initial running-in cycles (i.e. significant wear and layer removal may have occurred by then).

5.5. Conclusions

The question of the existence of the static friction peak in reciprocating sliding has been investigated in this chapter. It is widely observed in the literature that the static friction peak is generally absent in published fictional hysteresis loops (e.g. from gross slip fretting tests), but why? To investigate this behaviour, silicon samples with nanoscale roughness (up to 0.64 nm) were used to carry out the reciprocating sliding tests. The samples experienced reciprocating sliding for 100 cycles to inspect the effect of cycling on the static peak. It was found that a prominent static friction peak is present in the initial cycles of reciprocating sliding (i.e. first 12 cycles), but that it decays relatively quickly thereafter and has mostly disappeared by about 30 cycles. Therefore, the reason the peak is often absent may be because hysteresis loops are often reported for cycles well after the initial cycles (due to running-in periods etc.). As the sliding cycles are nominally identical, the decaying static friction peak can be attributed to wear processes. In the experiments, the reduction in the friction peak took the form of static friction reducing with cycles with the kinetic friction level remaining roughly constant. Results also showed that surface roughness increased significantly with cycles of testing. Two main explanations are advanced for the wear-induced decay. The first is that significant increases in roughness during the test lead to reduction in the fully stuck real contact area (with cycles); thereby, producing a corresponding reduction in the static friction force. Applying the Xu et al. multi-asperity friction model [14] to the test surfaces, it has been shown that implementing the measured roughness reduction in the model predicts a similar static friction peak decay.

Another possible explanation is that of the breaking of chemical bonds (or removal of initial layers) formed due to interface exposure to air. These chemical bonds/layers are believed to lock the interface in the initial cycles. It is possible that a few cycles of sliding is sufficient to remove or alter these layers, leading to lower friction levels being required to initiate sliding. As Silicon is a brittle single crystal material, creep induced growth of the contact area is an unlikely explanation for the static friction peak here. This is also confirmed by the appearance of the peak in cycles following the first cycle (such as Cycle 2) where time available for junction growth (of the real contact area) is

insufficient as the reciprocating contact reverses direction in milli-seconds. It may be that both surface roughness changes and molecular layer removal both contribute to the behaviour. However, the exact origin of the friction peak decay observed here in reciprocating sliding requires more investigation. However, we can confidently conclude that the rapid delay in the static friction peak is a wear induced phenomenon.

Having succeeded in reaching meaningful conclusions in the studies of static friction in unidirectional and reciprocating sliding, it was necessary to widen our understanding of friction by investigating the role of kinetic friction in triboelectrification. This will be discussed in the next chapter.

Chapter 6: The effect of friction on triboelectrification

6.1. Introduction:

To acquire a better understanding of friction between sliding contacts, it was important to transit from static friction where slow speed is often applied to high sliding speed to inspect the role of kinetic friction in a sophisticated device. Frictional interfaces are usually associated with contact electrification caused by an energetically favourable transfer of electrons between the contacting materials. When the surfaces are in physical contact, opposite charges will form on each side of the interface. The periodic separation of these oppositely charged surfaces establishes a potential difference. The existence of surface charges has long been undesirable in many applications, particularly those that involve polymers. This is because polymers accumulate and preserve charges so easily on their surfaces [18, 22, 103]. The continuous movement of parts that involve polymers can give rise to excessive heat causing operation failure [18]. With small particles, the phenomenon can cause agglomeration which then blocks up pipes and equipment (particularly in the pharmaceutical industry). The contact charges, on the other hand, can also be used to advantage – this is a more recent development. In 2012, a device known as a triboelectric nanogenerator (or TENG) was invented to do just this. The clever innovation was the structure: the use of thin dielectric layers (about 100 to 500 μm) to mirror the charges onto backing electrodes by electrostatic induction. Current then flows between the two electrodes during separation and approach. TENGs are efficient (at low frequencies), flexible and low cost energy harvesters. Although their power output is higher than that of piezoelectric nanogenerators, they produce a comparatively low output (<500 W/m^2). However, they would appear to be ideal for supplying low powered small-scale devices (such as LEDs and self-powered sensors [104]).

The link between friction and contact charges can be observed in metal-polymer or polymer-polymer interfaces. Friction is correlated with contact charges due to the impact of Van der Waals, Coulomb forces and chemical bonds on charge formation [21, 106, 107]. The correlation between friction and charges has been widely studied in the literature [18-22]. These studies have been successful in identifying a direct correlation between friction and surface charges. It has been found that simultaneous fluctuations were observed in the frictional and electrical signals, indicating that they originate from the same source [107]. Friction interactions namely “stick-slip” events have an immediate impact on the charge transfer between the contacting surfaces [19, 20]. It has been observed that the charge transfer occurs in the slip events when the bonds that are formed during the stick events are ruptured [20]. This was evident in the coinciding increases in the charge transfer when the interface was in the slipping phase [20]. However, it should be noted that these observations were seen at a slow sliding speed (< 1 mm/s) which is not the case for TENG devices. There has been a lack of studies in the TENG context, specifically sliding mode, that correlate friction with electrical output.

The role of friction in the sliding mode TENG needs to be carefully considered. There are numerous interesting questions: does frictional sliding enhance charge transfer (as compared to the normal contact mode) and how do changes in friction effect charge transfer and TENG output. Likewise, there is the question of how electrical charges can affect friction.

It is worth recalling the review of TENGs briefly after discussing the correlation between contact electrification and friction. The idea for the TENG was put forward in 2012 by Prof Zhong Lin Wang and his group in 2012 [105, 124-126]. TENG modes have been essentially categorised into two main modes; namely, the contact separation (CS-TENG) and sliding (S-TENG) modes. The structure of TENGs began with a simple design using two dielectric layers with electrodes placed on the backside of the insulators. TENG research was initially directed toward contact (vertical) separation due to its simplicity. The mechanism has evolved into a variety of structures to reflect daily life activities. The structures that have been commonly used in the literature are single electrodes [133, 134] and two electrodes with a gap between them (free-standing) [127, 133, 135] in contact with a dielectric layer.

This chapter aims to explore the role of friction in triboelectrification via the sliding mode TENG. To achieve this, the rig designed in Chapter 3 and adapted in Chapter 5 (to facilitate reciprocating sliding) was further modified to perform freestanding sliding mode tests. PET in contact with copper were used as the core triboelectric pair for the study. The sliding mode has been promising due to its high and stable electrical output [127, 135]. However, the tribological behaviour of the triboelectric layers in the sliding mode TENG has not been studied adequately in S-TENG literature. In particular, the role of friction and wear have not been comprehensively considered. Additionally, in many of the published S-TENG papers, accurate and controlled experimental designs to implement sliding are absent (particularly in the early papers). For example, some sliding TENG tests were carried out by hand with no accurate control over sliding speed, stroke length and normal load and often no concurrent measurement of friction force. It should be noted that there has actually been some recent progress in realising more accurate testing of S-TENGS. For example, Armitage et al. [115] have implemented an S-TENG testing approach in a commercial tribometer (Bruker UMT Tribolab) and have successfully been able to measure electrical output concurrently with tangential force. In this chapter, an investigation of the frictional and electrical behaviour of the PET-Cu interface will be presented. The chapter aims also to present a systematic comparison between CS-TENG and S-TENG using the same materials and experiential parameters. Since bulk sliding is absent in the CS-TENG, this direct comparison should allow some identification of the role that friction plays. While there are observations in the literature comparing sliding mode with normal contact mode (e.g. in review papers), these are mostly from tests with vastly different parameters (e.g. different layer thicknesses, different materials, different device sizes, different structures, different normal loads and frequencies

etc.). This study aims to produce a careful comparison where as many as possible of the many variables are kept the same between both test types.

6.2. Experimental procedure:

The friction rig described in Chapter 3 was adapted with electrical measurements to investigate the frictional behaviour (friction and wear) and electrical properties of the triboelectric surfaces. The experimental setup is similar to the one shown in Chapter 5. Tribological parameters (i.e. normal load and tangential force) were measured using the button load cell (LBS, Interface Force Measurements, UK) for normal load and the tension/compression load cell for tangential force (SML, Interface Force Measurements, UK). Electrical measurements were first performed via oscilloscope (RSMSO-2202EA, RS Components Ltd, UK) to measure the output voltage. This study also measured the electrical power of the TENG. The rig was combined with an electrometer (6517B, Tektronix, Inc, USA) for measuring voltage and a preamplifier (SR570, Stanford Research Systems, USA) connected to the oscilloscope to measure the current. The schematic of the rig is shown in Fig. 6. 1 (the numbers indicate the main components). The inset shows the contact zone in a close-up view. The normal load is applied by compression springs which is transmitted through the x-shaped arm to the interface through the button load cell. The button load cell has a spherical tip to allow the top surface to self-align with the bottom surface. The top surface is Polyethylene terephthalate (PET) bonded to an acrylic block. Dimension of PET is 20x25 mm^2. The top part was constrained from movement by stoppers in either direction. The bottom sample is composed of two strips of copper (Cu) with a 5-mm gap between them and dimensions of 20 x 30 mm^2 each, producing a “free-standing” mode arrangement. They were placed on a glass plate (to provide a smooth and highly flat backing surface). The bottom part is positioned on a metal block that is placed on an ultra-low friction bearing. The motion was initiated by pulling/pushing the metal block via a stepper motor (NEMA 23, Lin Engineering, USA). Tangential force and electrical signal were measured simultaneously at the first instance of movement. Motion control and force measurement were carried out using a LabView program. The signal from the load cells was transmitted to the user interface via a full-bridge amplifier (NI-9237, National Instruments, USA).

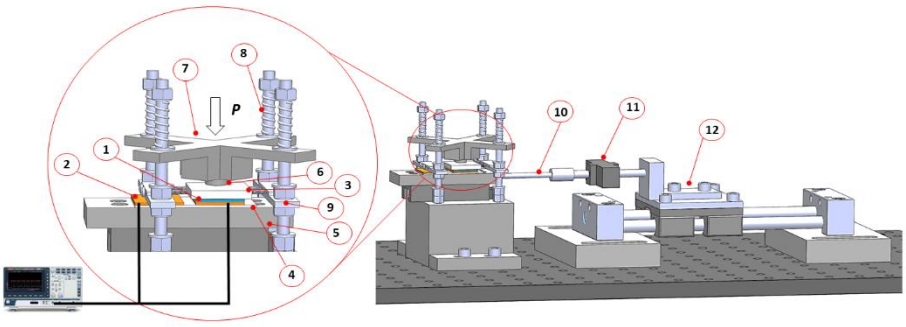

Fig. 6. 1. Synchronous friction-voltage test rig of freestanding TENG: (1) PET layer, (2) Copper strips, (3) Acrylic backing plate, (4) Glass plate, (5) Moving metal plate, (6) Button load cell, (7) x-shaped arm, (8) Springs, (9) Stoppers, (10) Connecting rod, (11) Tension/compression load cell, (12) Motorised linear stage,

The investigation of the tribological and electrical behaviour of the PET-Cu interface was carried out to study the effect of friction and wear on the electrical performance of the triboelectric interface. In all tests, the start position of the pair was adjusted to achieve a full overlap between the PET surface and the first electrode. Sliding then started until the PET fully aligned with the second electrode and returned to the initial position to complete one cycle. The electrical measurements involved measuring the output voltage and electrical power. The output voltage measurement was performed by varying the sliding speed on each normal load. The normal load range was from 2 to 10 N with a 2-N increment. For each normal load, the speed range started from 5 mm/s to 125 mm/s with a 30-mm/s difference. At the same time, friction curves were generated to inspect friction throughout sliding. The electrical power measurement was done by applying the maximum speed and normal load (i.e. 125 mm/s and 10 N respectively) and connecting the interface with a wide range of resistors to inspect the optimal resistance value that results in the highest power. This was performed by multiplying voltage across each resistor by current passing through it to generate the power curve. The wear study was also performed by applying the maximum speed and normal load. The surfaces experienced 2 hours of sliding constituting 13 x 10^3 cycles. To inspect the impact of wear qualitatively, the copper surfaces were scanned in an optical profilometer (InfinteFocus G4, Alicona, Austria) before and after tests. While the previously developed rig was used for the sliding mode tests, an electrodynamic mechanical test machine (Instron E3000, UK) was used to perform the normal contact separation tests (using the same materials, device dimensions and experiment parameters). The mechanism of this TENG configuration was to force the upper surface (PET) to fully contact (conformal contact) the lower surface (Cu) and then release the force to permit the upper surface to return to its original position, forming a single cycle. This movement was repeated with different normal loads and motion frequency to mirror the mechanism performed in the sliding mode.

6.3. Results and discussion

The working mechanism of the free-standing TENG is shown in Fig. 6. 2 The figure illustrates the relative movement between the triboelectric layers in four stages showing the corresponding friction and voltage curves for each stage. At Stage 1, charges with opposite polarities are formed in the interface. Negative charges are distributed on the PET surface whereas positive charges are formed on the copper surface due to the electrical induction. The polarity of charges is determined by the positions of these two materials in the triboelectric series [128]. It is known that PET is more electronegative than Cu (i.e. PET has more tendency to accept electrons), which means that PET would be negatively charged when contacting Cu. The motion is initiated at this stage. The bonded surfaces start to detach (i.e. PET leaves Electrode 1) as soon as the tangential force overcomes the static friction. The output voltage at this stage is almost zero as there is no charge movement between the electrodes. The motion continues forcing the charges to move from Electrode 1 to Electrode 2 to neutralise the interface (Stage 2). This initiates potential differences between the electrodes. The output voltage reaches the maximum once the PET surface is at almost the midpoint of the stroke where the interface achieves the optimal charge separation. Following this, the PET surface reaches the end of the stroke (Stage 3), mirroring the condition of Stage 1. Before returning to the initial position, the output voltage gradually reaches the peak value (Stage 4) – approximately at the same voltage value as Stage 2. The PET then reaches the initial position, completing a full cycle. Subsequently, the interface experiences the same stages again for the following cycles.

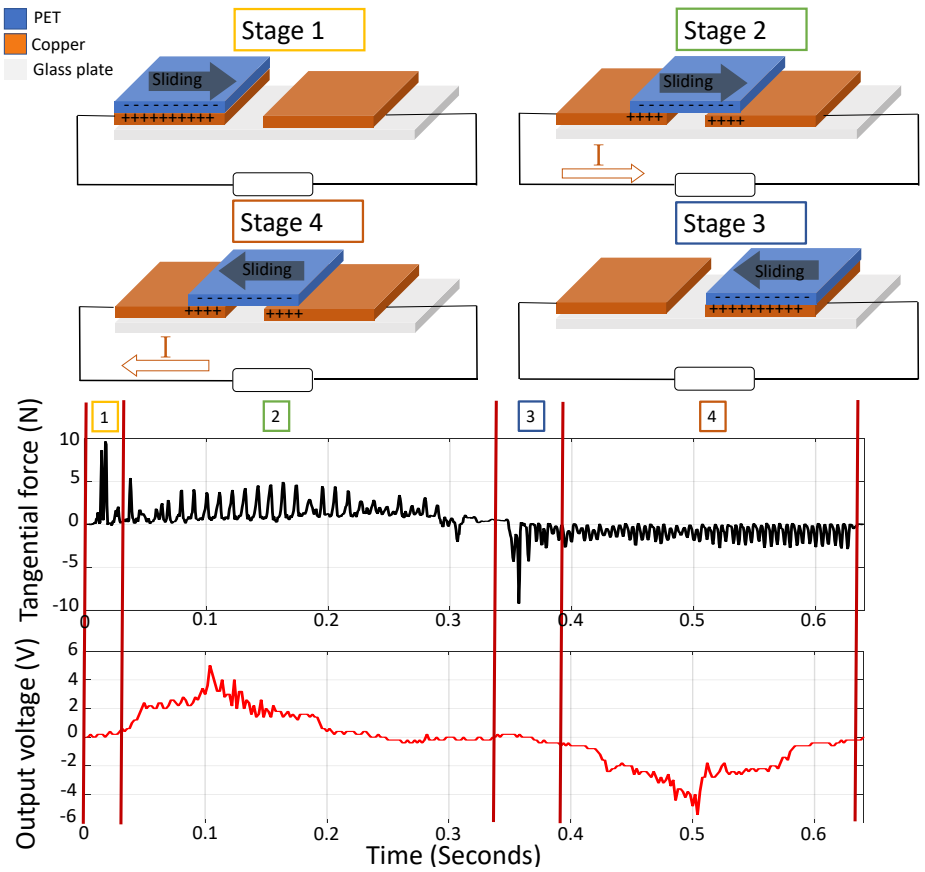

Fig. 6. 2. Illustration of the S-TENG test mechanism showing the relative movement between the triboelectric layers and corresponding curves of friction and voltage.

The relationship between the output voltage and sliding speed with varying normal loads is shown in Fig. 6. 3 This relationship is significant in investigating the electrical performance of the triboelectric layers. The figure shows the expected linear increase between the output voltage and speed toward a maximum averaged value of approximately 6 V. The low voltage at the slow speed is attributed to the sufficient time available to neutralise the interface. In contrast, the frequent contact separation at high speed forces the surface charges to continuously move between the electrodes, resulting in a faster pumping of charge (i.e. $I = dQ/dt$). It can also be seen that there is an increase in the output voltage with the normal load. This is believed to be correlated to the increase in real contact area with contact pressure which is essentially due to the way in which rough surfaces deform when pressed together [103, 114]. This contact force dependence has been extensively identified and studied for the normal contact separation mode TENG [112, 113, 116]. The effect of normal load on the output voltage showed no further increase after 4 N. Similar findings were obtained from Yang *et al.* [114] where there was no increase in voltage for contact pressures higher than 7.5 kPa. This contact pressure is comparable to the pressure applied on the interface in this study for the 4 N normal load

which is around 8 kPa. This suggests that there was little growth in the real contact area (i.e. A_r approaches the nominal contact area) when the load was higher than 4 N. It has been shown that, for polymers in contact with metals, if the pressure is lower than the plastic flow stress of the polymer, there would be a linear increase between the pressure and real contact area, corresponding to the elastic deformation regime [47]. Once the pressure exceeds the plastic flow stress, the asperities would be all plastically deformed leading to no further growth in the real contact area [47]. The output voltage obtained in this study is comparable to the voltage acquired by Yang et al. [114] which ranges between 8 to 14 for their different contact arrangements.

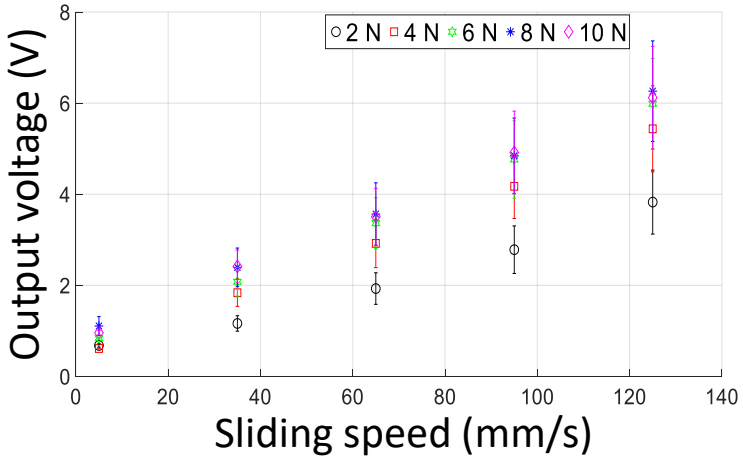

Fig. 6. 3. The output voltage versus the sliding speed with applying different normal loads.

The frictional behaviour was also studied to investigate whether the output voltage can be correlated with friction. Here, the dynamic friction was plotted in Fig. 6. 4 (a) against the sliding speed with the different normal loads. There does appear to be a gradual increase in friction with sliding speed. As expected, the dynamic friction force increases in step with the normal load. In line with the literature, it would be expected that the interactions that dictate the real contact area (i.e. deformation of asperities) are the responsible element that directly influences the electrical and frictional behaviour. This is also seen in the force ratio (i.e. coefficient of friction (COF)) required to maintain steady movement (Fig. 6. 4 (b)). The COF during the elastic deformations, at relatively low loads, decreases exponentially with the normal load from around 0.5 to 0.2. This is commonly observed in polymers experiencing sliding friction as shown in Refs. [44, 47, 166]. It is worth saying that the COF resulted from the polymer-metal interface in this study was similar to those obtained from the S-TENG literature in Armitage et al [115] and Zhang et al. [132], where an average value of around 0.4 was obtained. The decreasing of the COF trend in Fig. 6. 4 is attributed to the so-called “power law” that governs the relationship between the real contact area (A_r) and normal load (P) stating that $A_r \propto P^n$ where n lies between 0.74 and 0.96 [44, 166]. As the load increases, the exponent n reaches the unity

(*n = 1*), resulting in the independency of COF on the normal load [47]. This is observed in the COF of the loads higher than 4 N.

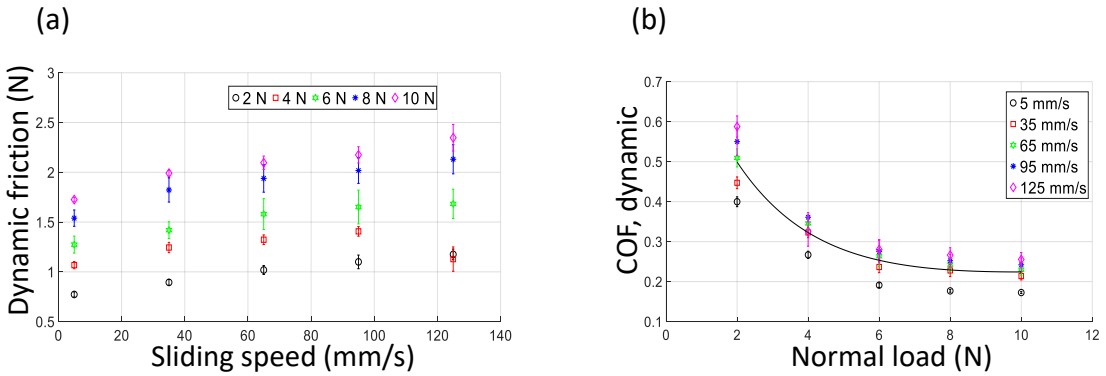

Fig. 6. 4. Frictional behaviour of the triboelectric layers showing: (a) Dynamic friction versus sliding speed and (b) COF against normal load.

Deviating from the sliding mode, the PET-Cu interface was also studied using the vertical contact separation mode (CS-TENG) to inspect the electrical performance of the pair in this mode and compare it with the performance obtained from the sliding one. The tests were performed by varying the contact-separation frequency and changing the normal load. Fig. 6. 5 shows the output voltage versus the frequency for the PET-Cu interface under different normal loads. The range of the frequency was chosen depending on the corresponding frequency of the maximum speed set in S-TENG which is around 1.8 Hz. It is seen that the output voltage increases as the frequency increases which has the same effect as increasing the speed in the S-TENG (i.e. increasing frequency leads to a higher $I = dQ/dt$). Notably, the output voltage is directly proportional to the normal load for the whole range of the applied loads. In the CS-TENG case, it seems that the asperity deformations did not transit from the elastic regime where the real contact area is increasing with the normal load giving rise to a higher voltage. To apply a clear comparison between S-TENG and CS-TENG, the output voltage of 2 Hz was compared with the output voltage of 125 mm/s (corresponding to 1.8 Hz) for the full range of the normal load in Fig. 6. 6. It is noticed that there is a large difference in the voltage magnitude between these two modes. The figure shows that the output voltage of S-TENG was far higher than CS-TENG for the whole range of the normal load (with all other parameters equal). This is an indicator that the frictional sliding contributes directly to boosting tribocharge transfer and electrical output. Even though the output voltage was increasing with load in the CS-TENG, the maximum voltage (peak-to-peak) for this frequency (≈ 4 V) was far lower than the one from S-TENG (≈ 8.5 V). In is likely that sliding brings more area into contact and thereby allows for more charge transfer. It should be noted that the output voltage in the CS-TENG of this study was notably less than the one obtained in Kumar et al.

[116] which was in the range between 10 to 20 V. This can be attributed to the materials used in Kumar's study. They used mica in contact with PVS. The mica was believed to have high dielectric strength which was beneficial for the charge induction [116].

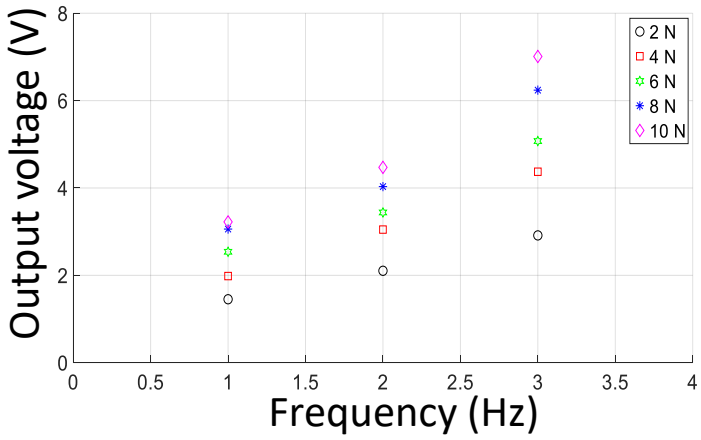

Fig. 6. 5. The relationship between the output voltage and frequency with different normal loads of a CS-TENG test.

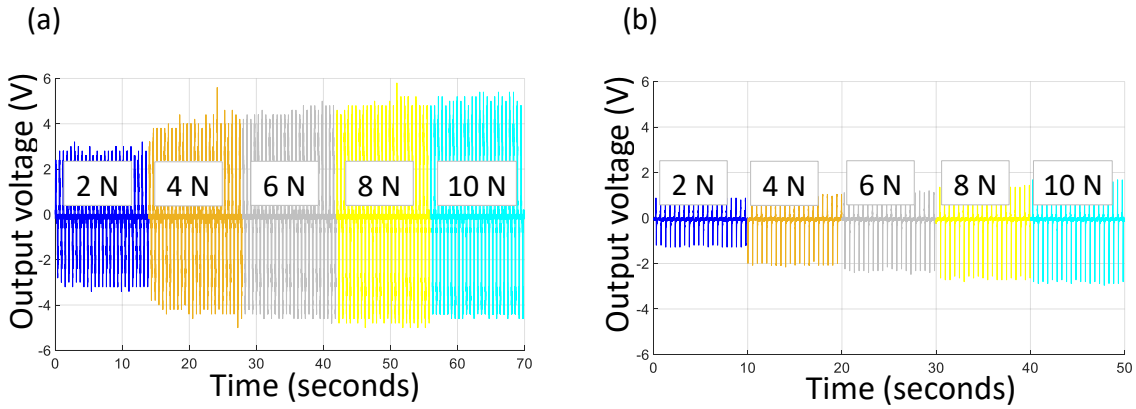

Fig. 6. 6. The voltage signals for (a) S-TENG and (b) CS-TENG tests experiencing different normal loads.

Another significant criterion to assess the electrical performance of a TENG device is the power generated from the mechanical movement. To obtain the power curve of the device, a wide range of resistors were connected to measure voltage and current resulting from individual resistors. Fig. 6. 7 (a) and (b) present the variation of current and voltage. As expected, the maximum currents were obtained from the lowest resistance value that allows 0.98 µA and 0.21 µA to pass through the resistor in the S-TENG and CS-TENG respectively. The voltage values, in contrast, were at their maximum when the highest resistor was connected to the circuit. The open circuit voltages for the S-TENG and CS-TENG were 90 V and 2 V respectively. It is observed that the S-TENG generated considerably high voltage and current compared to the CS-TENG. Therefore, the generated power is also much higher

when the triboelectric layers are set for sliding mode. This is seen in the large difference in power between these modes in the power curves presented in Fig. 6. 7 (c) and (d). The significant difference in the electrical output between the normal and sliding contact was also observed in Ref [135] where the output from sliding was over 100 times larger. The optimal power values were 63 µW obtained from the S-TENG and 0.15 µW from the CS-TENG. The optimal power was obtained from resistance values of 1 GΩ and 0.1 GΩ for S-TENG and CS-TENG, respectively.

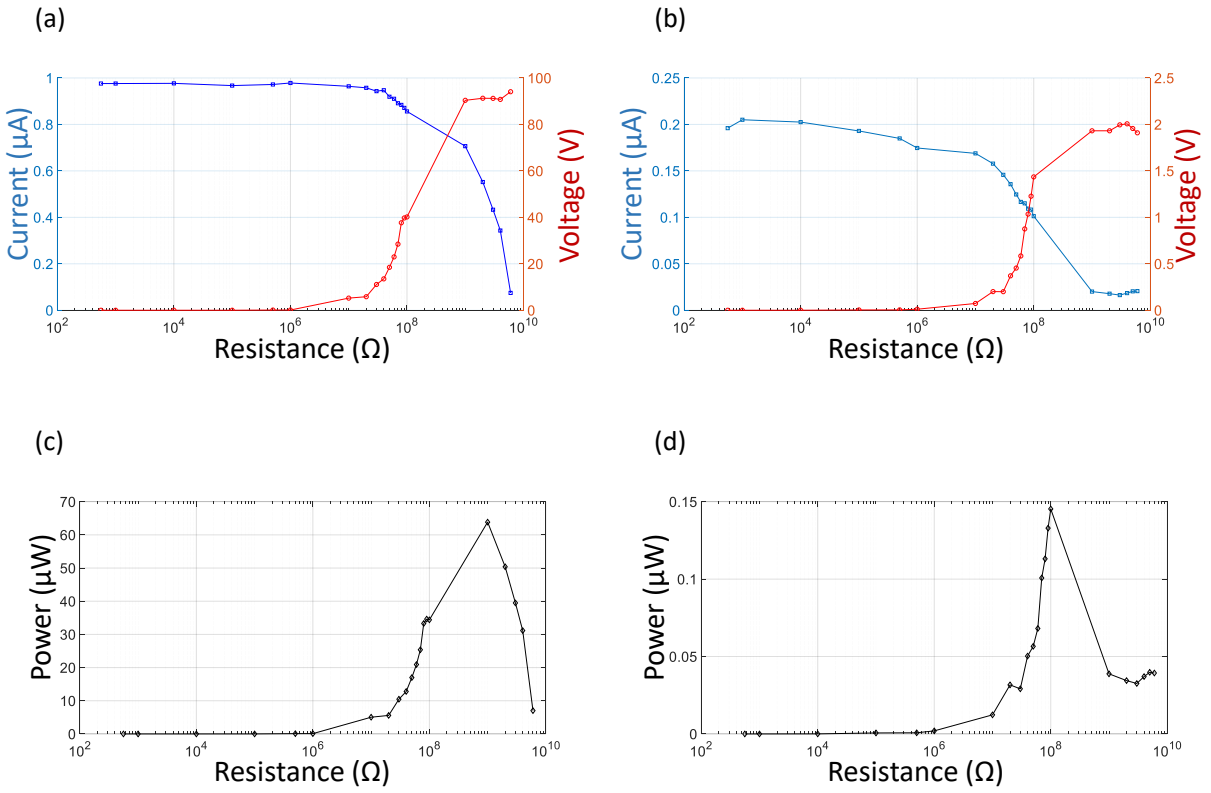

Fig. 6. 7. Current and voltage measurements of: (a) S-TENG and (b) CS-TENG. Multiplication of these measurements provide the electrical power of (c) S-TENG and (d) CS-TENG.

Having shown the superiority of the S-TENG, it is crucial to assess its stability and durability to examine its performance with time. One potential disadvantage of the S-TENG might be suseptibility to higher wear rates than the CS-TENG. The stability of the S-TENG was assessed by running the device for 1500 cycles under 10 N with a sliding speed of 125 mm/s. The output voltage for the full duration of sliding is shown in Fig. 6. 8. It is encouraging to note that the output voltage was almost stable throughout the test which took 14 minutes of continuous sliding. This is important because it indicates that the devices can generate the same electricity for relatively long periods. This can power tens of LEDs for a long time. The durability is another important aspect of assessing the S-TENG performance. The test was done by applying 13 x 10^3 cycles using 10 N for the normal load and 125 mm/s for the sliding speed to inspect the impact of wear qualitatively. The effect of the sliding on the triboelectric layers

was investigated only on the copper surface. This is because the PET surface was transparent which requires specialised equipment for characterisation. Fig. 6. 9 illustrates the impact of wear by comparing optical images of the Cu surface of the before and after test scans. İt is evident that the Cu surface was severely worn after the test. The worn surface suffered from wear tracks, material transfer from PET and presumably the presence of external particles. To inspect the effect of these artefacts on the output voltage, the voltage was recorded for the full duration of the test. The output voltage of the initial cycles was approximately 8.5 V which was then dropped (just before two hours of sliding) to 5 V. It has been suggested that these artefacts affect the mechanism of the original charge transfer due to new interfaces introduced throughout sliding, lowering the possibilities of the formation of the triboelectric charges [115]. Even though triboelectric layers in THE S-TENG can generate relatively higher output than their counterparts in CS-TENG, the wear effect is considerable and this reduces the lifetime of the decives.

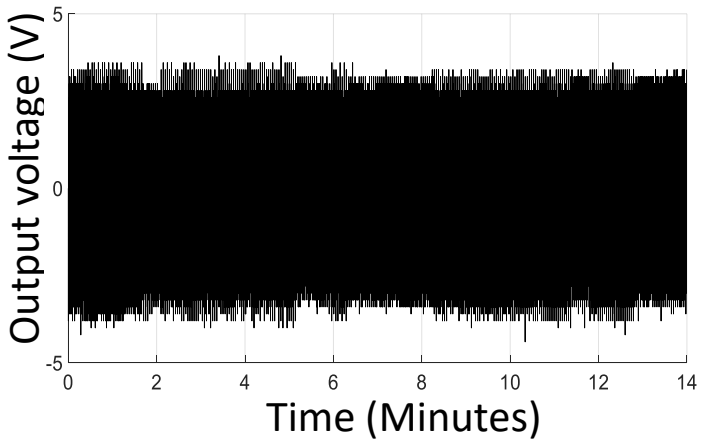

Fig. 6. 8. The stability of the output voltage for an S-TENG device experiencing 1500 cycles with 10 N normal load and 125 mm/s sliding speed.

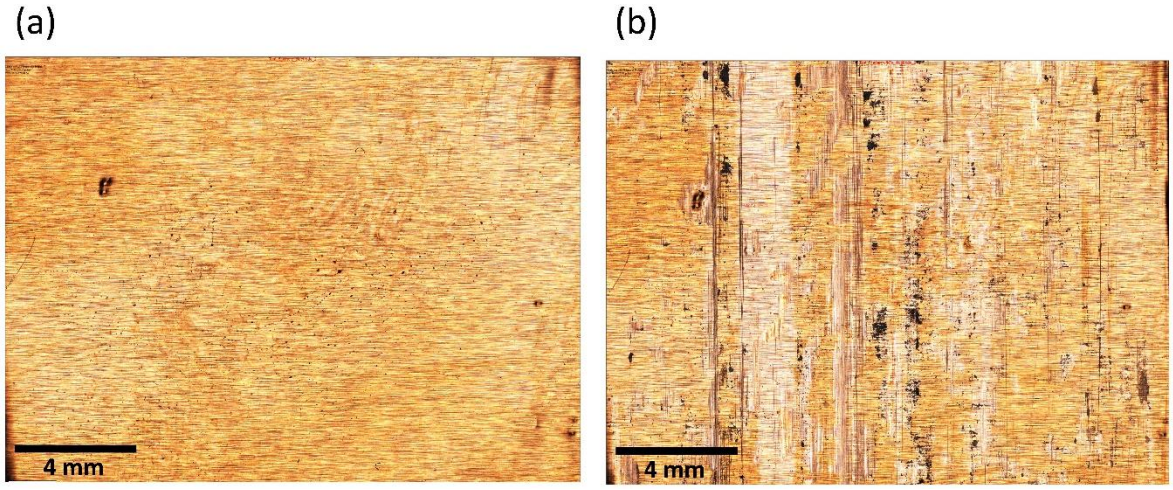

Fig. 6. 9. Optical images of the Cu surface before (a) and after (b) testing.

6.4. Conclusion

This chapter has explored the role of friction in triboelectrification. The key test was a comparison of electrical results from the sliding mode TENG (S-TENG) with the contact seperation mode TENG (CS-TENG) while holding as many device parameters as possible constant (i.e layer thicknesses, device size, materials, contact pressure etc.). The important difference being that the S-TENG experiences gross sliding, while the CS-TENG does not. The materials used in this study were PET and Cu. The friction rig was combined with electrical instrumentation to investigate the behaviour of these layers. The new set-up of the rig enabled concurrent measurement of voltage and friction force. The rig also provides a robust system for applying and measuring normal and tangential loads. The tests initially started by varying the sliding speed and normal load to inspect the response of the triboelectric layers to these changes. The experiments showed the expected increase in the output voltage with both sliding speed and normal load. The relationship between the friction force and normal load behaved similarly to the output voltage and normal load trend. This indicates that they both were influenced by the same source which is the real contact area. The S-TENG produced a considerabley higher ouput compared to the CS-TENG. This is in line with current consensus in the literature (where less appropriate test results –with differing parameters - were used to make a comparison). One reason for this might be the fact that sliding brought more area into contact and hence produced more opportunities for charge transfer. Aother possibility (via the flexoelectric effect) might be the action of the frictional traction which is likley to increase the strain gradients in the asperities. To obtain a more meaningful illustration of the comparison between these modes, electrical power plots were created against electrical resistance. The measurement was done by measuring voltage and current across a wide range of resistors to obtain optimal electrical power. The final stage of the experiment was to assess the stability and durability of the S-TENG device. It was encouraging to observe that the output voltage was stable at around 8 V for a continuous sliding of 14 minutes. This voltage should be enough to illuminate tens of LEDs for a relatively long time. Even though the S-TENG device generates higher electricity, it can suffer from wear decreasing its output over time and reducing the lifetime of materials – indeed, the tested S-TENG samples showed evidence of significant wear after the tests.

This work was the last experimental work that was applied in the customised friction rig. Three major research topics were addressed using the rig. These topics were good indications of the applicability of the friction rig in performing different contact scenarios and succeeding in achieving meaningful conclusions. The next chapter will present the main conculsions of these three research topics along with identifying future recommendations inspired by limitations encountered while performing the tests.

Chapter 7: Conclusion and future recommendations

7.1. Conclusion

This thesis has investigated some key aspects and ideas on static and sliding friction. It began with the design and assembly of an adaptable friction rig for implementing flat-on-flat linear sliding and then proceeded to study three major aspects: the tailoring of friction using micropatterned surfaces, the existence of the static friction peak in reciprocating sliding and finally, the role of friction in triboelectrification. The main aim of the project was to tackle the research gaps associated with these three major aspects. The first gap was the uncertainty about the explicit impact of structuring techniques on tailoring static friction. After surveying the literature on friction of the structured surfaces, it was observed that there have been indecisive conclusions on the effect of structuring techniques on friction. Therefore, it was advantageous to examine the effectiveness of manipulating surface topography on tailoring static friction on idealised materials with nanoscale roughness and high flatness to attain a deeper understating of such a contact mechanism. To expand the study of static friction, the focus was directed to the static friction peak in the reciprocating sliding. The absence of the static friction peak in the reciprocating sliding needs investigating. This motivated studying the transition from static friction to kinetic friction in the reciprocating sliding. Having succeeded in studying static friction in the unidirectional and reciprocating sliding, it was vital to widen our understanding of friction by investigating the role of friction in triboelectrification, particularly in a TENG device. The impact of friction in S-TENG was not considered adequately in the literature. This topic is still immature and requires a thorough investigation.

Studying friction of structured interfaces was the first experimental topic of this project. One of the novel techniques applied in tribology is surface modifications using light-based structuring such as laser surface texturing (LST) and photochemical etching (PCT). These techniques have been implemented in the friction literature to inspect the possibility of controlling friction. LST has been successful in obtaining a rough level of control over the frictional interactions of contacting surfaces. However, structuring surfaces by LST is susceptible to chemical modifications on the structured surfaces and has accuracy limitations, affecting the frictional behaviour of the surfaces. To mitigate these impacts, PCT is considered a good alternative that can produce high-fidelity structured surfaces with high productivity. Implementing such a technique as a means for controlling friction via surface structuring seems worthy of study. This aspect was the first topic to be investigated in this project; namely, the possibility of tailoring the static friction of structured silicon samples patterned using photochemical etching (photolithography). The dry friction of these Si surfaces with nanoscale roughness and the possibility of using micropatterning to tailor friction by manipulating contact area was investigated. Square wave patterns produced on samples from silicon wafers (and their unstructured equivalent) were slid against unstructured silicon counter surfaces. The width of the

square wave features was adjusted to vary the apparent feature contact area. The existence of nanoscale roughness was sufficient to ensure Amontons' first law ($F = \mu P$) on both structured & unstructured samples. Somewhat counterintuitively, friction was independent of the apparent feature contact area making it difficult to tailor friction via the feature contact area. This occurred because, even though the apparent feature contact area was adjusted, the surface roughness and nominal flatness at the contact interface were preserved ensuring that the real contact area and thereby the friction, were likewise preserved. Thus, the adjustments to the feature nominal contact area amounted to the same behaviour as altering the nominal contact area of a fixed mass of material (i.e. friction is generally independent of the nominal area as captured in the Amontons-Coloumb law). This is an interesting special case, but not universally applicable: friction can indeed be adjusted by structuring provided the intervention leads to a change in *real* contact area (or interlocking)– and this depends on the specific surface geometry and topography.

The second aspect of friction investigated was the apparent absence of the static friction peak in the reciprocating sliding literature. Studies on frictional hysteresis loops were reviewed in an attempt to find the reason for the absence, but to the authors knowledge, there were no previous studies looking into this interesting observation. Here, reciprocating sliding tests were conducted on ultra-smooth silicon surfaces (equivalent to the unstructured samples in the previous work). The tests were done for 100 cycles with 10 N normal load and 0.05 mm/s sliding speed. A prominent static friction peak was present in the initial cycles. However, a rapid decay in the static friction peak occurred after the first cycle with the peak being mostly absent by about 30 cycles. The existence of the peak in the first cycles and then its disappearance in the subsequent cycles suggest that wear is most probably the cause for the disappearance. Two possible explanations are proposed for the wear-induced decay: (1) that increasing surface roughness (with cycles) reduces the fully stuck contact area and (2) that wear reduces the bonding strength of the stuck interface by removing third body contaminant molecules. Predictions from a multi-asperity friction model are used to support these arguments. The argument based on surface roughness proceeds as follows: sliding roughens the surface (higher roughness) thereby reducing the real contact area. Recalling the theory of Bowden and Tabor for sliding contacts, one might assume that this reduction in the real contact area might lead to a decrease in the static friction level resulting in less difference between static and kinetic friction. To verify the assumption of the wear effect on roughness, the roughness data was inserted in the adhesive contact model. It should be noted that the roughness parameters were the only variable in the model. The model results showed the same behaviour observed in the experiments; namely, that the roughness-induced reduction in the real contact area reproduces or predicts the decay of the static friction peak. Further study is required to confirm the exact mechanism of the wear induced decay.

The final topic of investigation concerned the role of sliding friction in triboelectrification. It was apparent in the literature review, that there are few studies where tribological aspects such as friction and wear are studied in relation to the sliding mode TENG (S-TENG). In addition, many S-TENG studies lack a sufficiently accurate and repeatable testing approach. It is acknowledged that friction has a pronounced impact on the formation of triboelectric charges. This is observed in contacting surfaces moving at slow speeds to accurately capture the correlation between friction and contact charges. With high-speed motion (typical speed in TENG), it might be difficult to correlate friction with the electrical output in the S-TENG. Thus, it is worth investigating this correlation in a TENG device. A key area of interest is the direct comparison between sliding TENG results and normal contact mode results. The normal contact mode has no gross sliding, while the sliding mode does – the idea being that a comparison could help isolate the role of frictional sliding. Loose comparisons had been made in the literature, but between TENG constructions that were vastly different (i.e. different layer thicknesses, different device sizes, different materials and different contact pressures and frequencies). The study in this thesis conducts a careful comparison of S-TENG and CS-TENG output while keeping as many device parameters as possible constant. Electrical instrumentation was incorporated into the friction rig to simultaneously measure friction and electrical outputs. In line with the presumptions in the literature, the S-TENG was found to have a significantly higher output compared to the CS-TENG. The maximum power output from the S-TENG was more than 400 times higher. The key reason for the difference would appear to be the frictional sliding in the S-TENG. It is likely that gross sliding introduces more mutual contact area between the two surfaces compared to the normal mode where there were no fresh regions to contribute to the contact area; thereby giving extra opportunities for charge transfer. It is also possible that the frictional traction induces higher strain gradients and, via the flexoelectric effect, this may lead to greater charge densities at the interface. It is clear that the physics of the role that sliding plays here will require further study. Finally, even though the output voltage of the S-TENG is higher, wear is likely to severely affect the contacting surfaces as shown in the experiments in Chapter 6.

7.2. Future recommendation

1- The first research topic focused on investigating the feasibility of tailoring static friction via structuring surfaces. The study assured that the structured surfaces (and the unstructured surfaces with nanoscale roughness) still obey the known friction laws (i.e. COF is independent of normal load and feature contact area). To widen our investigation on the structured surfaces, a wear study on these surfaces would be valuable to assess the impact of surface structuring in another frictional interaction. It has been suggested that channels between the micro-features might be useful to trap wear particles eliminating them from the interface [8, 82]. This could potentially reduce the impact

of wear on the interface and mitigate the contribution of ploughing on friction. Due to time restriction and limited facilities, this project was not able to perform a full-scale wear study to inspect whether the channels can be utilised to reduce wear. Additionally, it would be a good approach to implement the surface structuring on materials used highly in engineering, such as polymers or even metals. 3D printing might be used to generate these kinds of structured surfaces much more rapidly in a wide range of materials (as its resolution is constantly improving).

2- The investigation of the static peak in reciprocating sliding was successful in finding the reason for the disappearance of the peak – i.e. wear. However, it was not possible to definitively confirm whether the mechanism was due to a wear-induced roughening of the surface or a wear-induced rubbing away of surface layers that tended to bond the surfaces with higher strength before being rubbed away after just a few cycles. On a more technical note, it was noticed that the experimental sliding curves showed a slight rigid body shift for some cycles. The cause for this is believed to be related to the stoppers used to constrain the top sample from movement. The stoppers could not be tightened against the upper backing plate from each side as this would absorb some of the applied normal load; thus, a tiny gap had to be felt in place resulting in the displacement shift during motion reversal. Even though the friction results were not affected by these features (which occur before the static friction point), designing more robust stoppers would help obtain more accurate results. It was also observed that the experiments and model results were not in full agreement. This is because the model predicts the interfacial shear strength to be constant throughout sliding which contradicts with some experimental studies. This gave rise to an observable difference between the experiment and model results. Consequently, a model that allows the interfacial shear strength to be changing with cycles would be beneficial.

3- Studying the tribological and electrical behaviour of triboelectric layers was necessary to understand how the frictional response affects the electrical output. This study focused more on friction to inspect its impact on TENG output. The results showed that frictional sliding does appear to increase electrical output (as compared to the normal contact mode TENG). However, the reason why sliding boosts electrical output is not fully clear and this warrants further study. It should be noted that the triboelectric layers suffer a high degree of wear in the sliding mode. As stated earlier, this project did not have time to perform a thorough wear study to analyse the impact of wear on the triboelectric layers. A comprehensive wear study is needed for sliding mode TENGs – this is very important as many TENG constructions in the literature use very soft or fragile materials as surface layers (such as electrospun nano-fibrous layers). Additionally, it would be useful to optimise S-TENG output based on the variable parameters such as the geometric ratios involving the gap distance, the overlap lengths etc.

Bibliography

[1] G. W. Stachowiak and A. W. Batchelor, "Engineering Tribology," in *Engineering Tribology (Fourth Edition)*, G. W. Stachowiak and A. W. Batchelor, Eds., Fourth Edi ed. Boston: Butterworth-Heinemann, 2014, p. iii.

[2] S. M. Rubinstein, G. Cohen, and J. Fineberg, "Detachment fronts and the onset of dynamic friction," *Nature,* vol. 430, pp. 1005-1009, 2004.

[3] I. M. Hutchings, "Tribology: Friction and Wear of Engineering Materials," 1992.

[4] S. Zucca, C. M. Firrone, and M. Gola, "Modeling underplatform dampers for turbine blades: A refined approach in the frequency domain," *JVC/Journal of Vibration and Control,* vol. 19, pp. 1087-1102, 2013.

[5] A. Khamlichi, M. Bezzazi, and A. Jabbouri, "Optimizing friction behavior of clutch facings using pin- on-disk test," *International Journal of Physical Sciences,* vol. 3, pp. 65-70, 2008.

[6] G. Amontons, "De la résistance causée dans les machines," *Mémoires de l'Académie Royale A,* pp. 257-282, 1699.

[7] N. P. Suh and H. C. Sin, "The genesis of friction," *Wear,* vol. 69, pp. 91-114, 1981.

[8] Z. Wang, C. W. Wang, M. Wang, and Q. Z. Zhao, "Manipulation of tribological properties of stainless steel by picosecond laser texturing and quenching," *Tribology International,* vol. 99, pp. 14-22, 2016.

[9] E. S. Yoon *et al.*, "Tribological properties of bio-mimetic nano-patterned polymeric surfaces on silicon wafer," *Tribology Letters,* vol. 21, pp. 31-37, 2006.

[10] W. R. Chang, I. Etsion, and D. B. Bogy, "Static Friction Coefficient Model for Metallic Rough Surfaces," *Journal of Tribology,* vol. 110, no. 1, pp. 57-63, 1988.

[11] N. P. Suh, H. C. Sin, M. Tohkai, and N. Saka, "Surface Topography and Functional Requirements for Dry Sliding Surfaces," *CIRP Annals - Manufacturing Technology,* vol. 29, pp. 413-418, 1980.

[12] E. Rabinowicz, *Friction and wear of materials*. New York: Wiley, 1965.

[13] F. P. Bowden and D. Tabor, *The Friction and Lubrication of Solids*. Clarendon Press, 1950.

[14] C. Gachot *et al.*, "Dry friction between laser-patterned surfaces: Role of alignment, structural wavelength and surface chemistry," *Tribology Letters,* vol. 49, pp. 193-202, 2013.

[15] M. Kang, Y. M. Park, B. H. Kim, and Y. H. Seo, "Micro- and nanoscale surface texturing effects on surface friction," *Applied Surface Science,* vol. 345, pp. 344-348, 2015.

[16] Y. Bai, "Modification of adhesion and friction by surface structuring," ed, 2014, p. 185.

[17] I. Etsion, "Improving tribological performance of mechanical components by laser surface texturing," *Tribology Letters,* vol. 17, pp. 733-737, 2004.

[18] K. Sayfidinov, S. D. Cezan, B. Baytekin, and H. T. Baytekin, "Minimizing friction, wear, and energy losses by eliminating contact charging," *Science Advances,* vol. 4, no. 11, p. eaau3808, 2018.

[19] G. Ananthakrishna and J. Kumar, "Correlation between stick-slip frictional sliding and charge transfer," *Physical Review B,* vol. 82, no. 7, p. 075414, 08/13/ 2010.

[20] R. Budakian and S. J. Putterman, "Correlation between Charge Transfer and Stick-Slip Friction at a Metal-Insulator Interface," *Physical Review Letters,* vol. 85, no. 5, pp. 1000-1003, 07/31/ 2000.

[21] P. M. McGuiggan, "Stick Slip Contact Mechanics between Dissimilar Materials: Effect of Charging and Large Friction," *Langmuir,* vol. 24, no. 8, pp. 3970-3976, 2008/04/01 2008.

[22] T. A. L. Burgo, C. A. Silva, L. Balestrin, and F. Galembeck, "Friction coefficient dependence on electrostatic tribocharging," *Scientific reports,* vol. 3, no. 1, pp. 1-8, 2013.

[23] E. Rabinowicz, "The Nature of the Static and Kinetic Coefficients of Friction," *Journal of Applied Physics,* vol. 22, no. 11, pp. 1373-1379, 1951/11/01 1951.

[24] J. Chen, C. Zang, B. Zhou, and E. P. Petrov, "A study of friction microslip modeling for dynamic analysis of bladed discs with root joints," *Proceedings of the Institution of Mechanical Engineers, Part C: Journal of Mechanical Engineering Science,* vol. 233, no. 8, pp. 2599-2614, 2019/04/01 2018.
[25] Y. Xu, N. Gadegaad, and D. Mulvhll, "Statistical model of adhesive friction between two elastic nominally at rough surfaces," 2021.
[26] B. Weber, T. Suhina, A. M. Brouwer, and D. Bonn, "Frictional weakening of slip interfaces," *Science Advances,* vol. 5, no. 4, p. eaav7603, 2019.
[27] O. Jin and S. Mall, "Shear force effects on fretting fatigue behavior of Ti-6Al-4V," *Metallurgical and Materials Transactions A,* vol. 35, no. 1, pp. 131-138, 2004/01/01 2004.
[28] D. M. Mulvihill, M. E. Kartal, D. Nowell, and D. A. Hills, "An elastic-plastic asperity interaction model for sliding friction," *Tribology International,* vol. 39, pp. 185-198, 2017.
[29] H. L. Costa and I. M. Hutchings, "Some innovative surface texturing techniques for tribological purposes," *Proceedings of the Institution of Mechanical Engineers, Part J: Journal of Engineering Tribology,* vol. 229, pp. 429-448, 2014.
[30] F. P. Bowden, D. Tabor, and G. I. Taylor, "The area of contact between stationary and moving surfaces," *Proceedings of the Royal Society of London. Series A. Mathematical and Physical Sciences,* vol. 169, no. 938, pp. 391-413, 1939.
[31] A. I. Bennett *et al.*, "Contact Measurements of Randomly Rough Surfaces," *Tribology Letters,* vol. 65, no. 4, p. 134, 2017/09/02 2017.
[32] C. P. Hendriks and M. Visscher, "Accurate Real Area of Contact Measurements on Polyurethane," *Journal of Tribology,* vol. 117, no. 4, pp. 607-611, 1995.
[33] L. E. Helseth, "Optical force sensing principle based on transparent elastomer with a rough surface," *Sensors and Actuators A: Physical,* vol. 263, pp. 667-676, 2017/08/15/ 2017.
[34] J. F. Archard, "Elastic Deformation and the Laws of Friction," *Source: Proceedings of the Royal Society of London. Series A, Mathematical and Physical Sciences,* vol. 243, pp. 190-205, 1957.
[35] N. Axén, S. Jacobson, and S. Hogmark, "Friction and Wear Measurement Techniques," in *Modern Tribology Handbook* vol. 1, ed: CRC Press, 2001, pp. 493-510.
[36] K. Miyoshi and D. H. Buckley, "Friction, Deformation and Fracture of Single-Crystal Silicon Carbide," *A S L E Transactions,* vol. 22, no. 1, pp. 79-90, 1979/01/01 1979.
[37] D. E. Kim and N. P. Suh, "Frictional behavior of extremely smooth and hard solids," *Wear,* vol. 162-164, pp. 873-879, 1993/04/13/ 1993.
[38] N. P. Suh, M. Mosleh, and P. S. Howard, "Control of friction," *Wear,* vol. 175, pp. 151-158, 1994.
[39] D. Marchetto, A. Rota, L. Calabri, G. C. Gazzadi, C. Menozzi, and S. Valeri, "Hydrophobic effect of surface patterning on Si surface," *Wear,* vol. 268, pp. 488-492, 2010.
[40] S. T. r. Oktay and N. P. Suh, "Wear Debris Formation and Agglomeration," *Journal of Tribology,* vol. 114, no. 2, pp. 379-393, 1992.
[41] K. H. Zum Gahr, "Sliding wear of ceramic-ceramic, ceramic-steel and steel-steel pairs in lubricated and unlubricated contact," *Wear,* vol. 133, no. 1, pp. 1-22, 1989/09/01/ 1989.
[42] D. H. Buckley and K. Miyoshi, "Friction and wear of ceramics," *Wear,* vol. 100, no. 1, pp. 333-353, 1984/12/01/ 1984.
[43] J. R. Whitehead and F. P. Bowden, "Surface deformation and friction of metals at light loads," *Proceedings of the Royal Society of London. Series A. Mathematical and Physical Sciences,* vol. 201, no. 1064, pp. 109-124, 1997/01/01 1997.
[44] M. W. Pascoe, D. Tabor, and F. P. Bowden, "The friction and deformation of polymers," *Proceedings of the Royal Society of London. Series A. Mathematical and Physical Sciences,* vol. 235, no. 1201, pp. 210-224, 1956/04/24 1956.
[45] K. Miyoshi and D. H. Buckley, "Correlation of Tensile and Shear Strengths of Metals with Their Friction Properties," *A S L E Transactions,* vol. 27, no. 1, pp. 15-23, 1984/01/01 1984.

[46] R.-M. Wang, S.-R. Zheng, and Y.-P. Zheng, "11 - Other properties of polymer composites," in *Polymer Matrix Composites and Technology*, R.-M. Wang, S.-R. Zheng, and Y.-P. Zheng, Eds.: Woodhead Publishing, 2011, pp. 513-548.
[47] V. Quaglini and P. Dubini, "Friction of Polymers Sliding on Smooth Surfaces," *Advances in Tribology,* vol. 2011, p. 178943, 2011/12/14 2011.
[48] K. Miyoshi, D. H. Buckley, and M. Srinivasan, "Tribological properties of sintered polycrystalline and single crystal silicon carbide," 1982.
[49] F. P. Bowden, T. P. Hughes, and C. H. Desch, "The friction of clean metals and the influence of adsorbed gases. The temperature coefficient of friction," *Proceedings of the Royal Society of London. Series A. Mathematical and Physical Sciences,* vol. 172, no. 949, pp. 263-279, 1997/01/01 1939.
[50] D. A. Rigney and J. P. Hirth, "Plastic deformation and sliding friction of metals," *Wear,* vol. 53, no. 2, pp. 345-370, 1979/04/01/ 1979.
[51] Y. Xing, J. Deng, X. Feng, and S. Yu, "Effect of laser surface texturing on Si3N4/TiC ceramic sliding against steel under dry friction," *Materials & Design,* vol. 52, pp. 234-245, 2013.
[52] E. Rabinowicz, "Autocorrelation Analysis of the Sliding Process," *Journal of Applied Physics,* vol. 27, no. 2, pp. 131-135, 1956/02/01 1956.
[53] D. C. Evans and J. K. Lancaster, "The Wear of Polymers," in *Treatise on Materials Science & Technology*, vol. 13, D. Scott, Ed.: Elsevier, 1979, pp. 85-139.
[54] J. Denape and J. Lamon, "Sliding friction of ceramics: Mechanical action of the wear debris," *Journal of Materials Science,* vol. 25, no. 8, pp. 3592-3604, 1990/08/01 1990.
[55] D. M. Mulvihill, O. Smerdova, and M. P. F. Sutcliffe, "Friction of carbon fibre tows," *Composites Part A: Applied Science and Manufacturing,* vol. 93, pp. 185-198, 2017.
[56] F. P. Bowden and L. Leben, "The nature of sliding and the analysis of friction," *Proceedings of the Royal Society of London A: Mathematical, Physical and Engineering Sciences,* vol. 169, pp. 371-391, 1939.
[57] C. Gachot, "Laser interference metallurgy of metallic surfaces for tribological applications," in *Universität des Saarlandes*, ed, 2012.
[58] A. R. Mojdehi, "Experimental and Theoretical Studies of Friction and Adhesion of Elastomeric Materials," ed, 2017.
[59] N. Axén, L. Kahlman, and I. M. Hutchings, "Correlations between tangential force and damage mechanisms in the scratch testing of ceramics," *Tribology International,* vol. 30, pp. 467-474, 1997.
[60] A. Ovcharenko, G. Halperin, I. Etsion, and M. Varenberg, "A novel test rig for in situ and real time optical measurement of the contact area evolution during pre-sliding of a spherical contact," *Tribology Letters,* vol. 23, pp. 55-63, 2006.
[61] C. Gachot, A. Rosenkranz, S. M. Hsu, and H. L. Costa, "A critical assessment of surface texturing for friction and wear improvement," *Wear,* vol. 372-373, pp. 21-41, 2017.
[62] N. Prodanov, C. Gachot, A. Rosenkranz, F. Mücklich, and M. H. Müser, "Contact Mechanics of Laser-Textured Surfaces," *Tribology Letters,* vol. 50, pp. 41-48, 2013.
[63] U. Pettersson and S. Jacobson, "Influence of surface texture on boundary lubricated sliding contacts," *Tribology International,* vol. 36, pp. 857-864, 2003.
[64] L. S. Martz, "Preliminary Report of Developments in Interrupted Surface Finishes," *Proceedings of the Institution of Mechanical Engineers,* vol. 161, pp. 1-9, 1949.
[65] Y. G. Schneider, "Formation of surfaces with uniform micropatterns on precision machine and instruments parts," *Precision Engineering,* vol. 6, pp. 219-225, 1984.
[66] P. Pavliček and E. Mikeska, "White-light interferometer without mechanical scanning," *Optics and Lasers in Engineering,* vol. 124, p. 105800, 2020/01/01/ 2020.
[67] F. Gao, R. K. Leach, J. Petzing, and J. M. Coupland, "Surface measurement errors using commercial scanning white light interferometers," *Measurement Science and Technology,* vol. 19, no. 1, pp. 13-13, 2008.

[68] A. Borghi, E. Gualtieri, D. Marchetto, L. Moretti, and S. Valeri, "Tribological effects of surface texturing on nitriding steel for high-performance engine applications," *Wear,* vol. 265, no. 7, pp. 1046-1051, 2008/09/20/ 2008.
[69] Q. Sun, T. Hu, H. Fan, Y. Zhang, and L. Hu, "Dry sliding wear behavior of TC11 alloy at 500°C: Influence of laser surface texturing," *Tribology International,* vol. 92, pp. 136-145, 2015/12/01/ 2015.
[70] A. Rosenkranz, L. Reinert, C. Gachot, and F. Mücklich, "Alignment and wear debris effects between laser-patterned steel surfaces under dry sliding conditions," *Wear,* vol. 318, no. 1, pp. 49-61, 2014/10/15/ 2014.
[71] I. Etsion "State of the Art in Laser Surface Texturing," *Journal of Tribology,* vol. 127, no. 1, pp. 248-253, 2005.
[72] L. Hao, Y. Meng, and C. Chen, "Experimental investigation on effects of surface texturing on lubrication of initial line contacts," *Lubrication Science,* vol. 26, pp. 363-373, 2014.
[73] H. L. Costa and I. M. Hutchings, "Hydrodynamic lubrication of textured steel surfaces under reciprocating sliding conditions," *Tribology International,* vol. 40, pp. 1227-1238, 2007.
[74] J. Zhang and Y. Meng, "A study of surface texturing of carbon steel by photochemical machining," *Journal of Materials Processing Technology,* vol. 212, pp. 2133-2140, 2012.
[75] J. Echávarri Otero, E. de la Guerra Ochoa, I. Bellón Vallinot, and E. Chacón Tanarro, "Optimising the design of textured surfaces for reducing lubricated friction coefficient," *Lubrication Science,* vol. 29, no. 3, pp. 183-199, 2017/04/01 2017.
[76] Y. Xu *et al.*, "Characterization of the Tribological Behavior of the Textured Steel Surfaces Fabricated by Photolithographic Etching," *Tribology Letters,* vol. 66, no. 2, p. 55, 2018/03/01 2018.
[77] M. Zou, L. Cai, H. Wang, D. Yang, and T. Wyrobek, "Adhesion and Friction Studies of a Selectively Micro/Nano-textured Surface Produced by UV Assisted Crystallization of Amorphous Silicon," *Tribology Letters,* vol. 20, no. 1, pp. 43-52, 2005/09/01 2005.
[78] R. P. Nair and M. Zou, "Surface-nano-texturing by aluminum-induced crystallization of amorphous silicon," *Surface and Coatings Technology,* vol. 203, no. 5, pp. 675-679, 2008/12/25/ 2008.
[79] J. Shimizu *et al.*, "Friction characteristics of mechanically microtextured metal surface in dry sliding," *Tribology International,* p. 105634, 2019/03/06/ 2019.
[80] A. F. Lasagni *et al.*, "Direct laser interference patterning, 20 years of development: from the basics to industrial applications," in *SPIE. Photonics West* vol. 10092, U. Klotzbach, K. Washio, and R. Kling, Eds., ed. San Francisco: International Society for Optics and Photonics, 2017, p. 1009211.
[81] C. Yu, H. Yu, G. Liu, W. Chen, B. He, and Q. J. Wang, "Understanding topographic dependence of friction with micro- and nano-grooved surfaces," *Tribology Letters,* vol. 53, pp. 145-156, 2014.
[82] Y. Xing, J. Deng, Z. Wu, and F. Wu, "High friction and low wear properties of laser-textured ceramic surface under dry friction," *Optics and Laser Technology,* vol. 93, pp. 24-32, 2017.
[83] J. Perris, Y. Xu, M. E. Kartal, N. Gadegaard, and D. M. Mulvihill, "Tailorable and Repeatable Normal Contact Stiffness via Micropatterned Interfaces," *Tribology Letters,* vol. 69, no. 3, p. 106, 2021/07/17 2021.
[84] A. Hamilton, J. Perris, N. Convery, D. M. Mulvihill, and N. Gadegaard, "Flexible Inserts for Injection Molding of Complex Micro-Structured Polymer Components," *Macromolecular Materials and Engineering,* https://doi.org/10.1002/mame.202100223 vol. 306, no. 9, p. 2100223, 2021/09/01 2021.
[85] A. Hamilton, Y. Xu, M. E. Kartal, N. Gadegaard, and D. M. Mulvihill, "Enhancing strength and toughness of adhesive joints via micro-structured mechanical interlocking," *International Journal of Adhesion and Adhesives,* vol. 105, p. 102775, 2021/03/01/ 2021.

[86] A. Hamilton, Y. Xu, M. E. Kartal, S. Kumar, N. Gadegaard, and D. M. Mulvihill, "Optimisation of interlocking microstructured adhesive joints via finite element modelling, design of experiments and 3D printing," *International Journal of Adhesion and Adhesives,* vol. 120, p. 103292, 2023/01/01/ 2023.
[87] H. Lee and S. Mall, "Fretting behavior of shot peened Ti–6Al–4V under slip controlled mode," *Wear,* vol. 260, no. 6, pp. 642-651, 2006/03/10/ 2006.
[88] N. M. Everitt, J. Ding, G. Bandak, P. H. Shipway, S. B. Leen, and E. J. Williams, "Characterisation of fretting-induced wear debris for Ti-6Al-4 V," *Wear,* vol. 267, no. 1, pp. 283-291, 2009/06/15/ 2009.
[89] S. Fouvry, P. Duó, and P. Perruchaut, "A quantitative approach of Ti–6Al–4V fretting damage: friction, wear and crack nucleation," *Wear,* vol. 257, no. 9, pp. 916-929, 2004/11/01/ 2004.
[90] A. Fantetti *et al.*, "The impact of fretting wear on structural dynamics: Experiment and Simulation," *Tribology International,* vol. 138, pp. 111-124, 2019/10/01/ 2019.
[91] N. Ohmae and T. Tsukizoe, "The effect of slip amplitude on fretting," *Wear,* vol. 27, no. 3, pp. 281-294, 1974/03/01/ 1974.
[92] M. Bazrafshan, M. B. de Rooij, and D. J. Schipper, "The effect of adhesion and roughness on friction hysteresis loops," *International Journal of Mechanical Sciences,* vol. 155, pp. 9-18, 2019/05/01/ 2019.
[93] O. Vingsbo and S. Söderberg, "On fretting maps," *Wear,* vol. 126, no. 2, pp. 131-147, 1988/09/01/ 1988.
[94] D. M. Mulvihill, M. E. Kartal, A. V. Olver, D. Nowell, and D. A. Hills, "Investigation of non-Coulomb friction behaviour in reciprocating sliding," *Wear,* vol. 271, no. 5, pp. 802-816, 2011/06/22/ 2011.
[95] S. R. Pearson, P. H. Shipway, J. O. Abere, and R. A. A. Hewitt, "The effect of temperature on wear and friction of a high strength steel in fretting," *Wear,* vol. 303, no. 1, pp. 622-631, 2013/06/15/ 2013.
[96] J. Hintikka, A. Lehtovaara, and A. Mäntylä, "Normal displacements in non-Coulomb friction conditions during fretting," *Tribology International,* vol. 94, pp. 633-639, 2016/02/01/ 2016.
[97] J. Hintikka, A. Lehtovaara, and A. Mäntylä, "Fretting-induced friction and wear in large flat-on-flat contact with quenched and tempered steel," *Tribology International,* vol. 92, pp. 191-202, 2015/12/01/ 2015.
[98] G. X. Chen and Z. R. Zhou, "Study on transition between fretting and reciprocating sliding wear," *Wear,* vol. 250, no. 1, pp. 665-672, 2001/10/01/ 2001.
[99] M. Long and H. J. Rack, "Friction and surface behavior of selected titanium alloys during reciprocating-sliding motion," *Wear,* vol. 249, no. 1, pp. 157-167, 2001/04/01/ 2001.
[100] E. Riedo, F. Lévy, and H. Brune, "Kinetics of Capillary Condensation in Nanoscopic Sliding Friction," *Physical Review Letters,* vol. 88, no. 18, p. 185505, 04/18/ 2002.
[101] Z. L. Wang and A. C. Wang, "On the origin of contact-electrification," *Materials Today,* vol. 30, pp. 34-51, 2019/11/01/ 2019.
[102] J. V. Escobar, A. Chakravarty, and S. J. Putterman, "Effect of anodic oxidation of single crystal boron doped diamond on tribocurrent and macroscopic friction force with metals," *Diamond and Related Materials,* vol. 36, pp. 8-15, 2013/06/01/ 2013.
[103] N. Luo *et al.*, "Controlling the tribological behavior at the friction interface by regulating the triboelectrification," *Nano Energy,* vol. 87, p. 106183, 2021/09/01/ 2021.
[104] R. Hinchet, W. Seung, and S.-W. Kim, "Recent Progress on Flexible Triboelectric Nanogenerators for SelfPowered Electronics," *ChemSusChem,* https://doi.org/10.1002/cssc.201403481 vol. 8, no. 14, pp. 2327-2344, 2015/07/20 2015.
[105] F.-R. Fan, Z.-Q. Tian, and Z. Lin Wang, "Flexible triboelectric generator," *Nano Energy,* vol. 1, no. 2, pp. 328-334, 2012/03/01/ 2012.
[106] G. Horn Roger and T. Smith Douglas, "Contact Electrification and Adhesion Between Dissimilar Materials," *Science,* vol. 256, no. 5055, pp. 362-364, 1992/04/17 1992.

[107] T. A. L. Burgo and A. Erdemir, "Bipolar tribocharging signal during friction force fluctuations at metal–insulator interfaces," *Angewandte Chemie,* vol. 126, no. 45, pp. 12297-12301, 2014.
[108] J. Lowell and A. C. Rose-Innes, "Contact electrification," *Advances in Physics,* vol. 29, no. 6, pp. 947-1023, 1980/12/01 1980.
[109] T. J. Fabish and C. B. Duke, "Molecular charge states and contact charge exchange in polymers," *Journal of Applied Physics,* vol. 48, no. 10, pp. 4256-4266, 1977/10/01 1977.
[110] C. Xu *et al.*, "On the Electron-Transfer Mechanism in the Contact-Electrification Effect," *Advanced Materials,* https://doi.org/10.1002/adma.201706790 vol. 30, no. 15, p. 1706790, 2018/04/01 2018.
[111] S. Li, Y. Zhou, Y. Zi, G. Zhang, and Z. L. Wang, "Excluding Contact Electrification in Surface Potential Measurement Using Kelvin Probe Force Microscopy," *ACS Nano,* vol. 10, no. 2, pp. 2528-2535, 2016/02/23 2016.
[112] G. Min, Y. Xu, P. Cochran, N. Gadegaard, D. M. Mulvihill, and R. Dahiya, "Origin of the contact force-dependent response of triboelectric nanogenerators," *Nano Energy,* vol. 83, p. 105829, 2021/05/01/ 2021.
[113] Y. Xu, G. Min, N. Gadegaard, R. Dahiya, and D. M. Mulvihill, "A unified contact force-dependent model for triboelectric nanogenerators accounting for surface roughness," *Nano Energy,* vol. 76, p. 105067, 2020/10/01/ 2020.
[114] S. Yang, H. Zhang, and S. Sang, "An In-Plane Sliding Triboelectric Nanogenerator with a Multielectrode Array for Self-Powered Dynamic Addressing and Trajectory Tracking," *Energy Technology,* https://doi.org/10.1002/ente.202000155 vol. 8, no. 6, p. 2000155, 2020/06/01 2020.
[115] J. L. Armitage, A. Ghanbarzadeh, M. G. Bryant, and A. Neville, "Investigating the Influence of Friction and Material Wear on Triboelectric Charge Transfer in Metal–Polymer Contacts," *Tribology Letters,* vol. 70, no. 2, p. 46, 2022/04/07 2022.
[116] C. Kumar *et al.*, "Multiscale in-situ quantification of the role of surface roughness and contact area using a novel Mica-PVS triboelectric nanogenerator," *Nano Energy,* vol. 107, p. 108122, 2023/03/01/ 2023.
[117] M. D. Hogue, C. R. Buhler, C. I. Calle, T. Matsuyama, W. Luo, and E. E. Groop, "Insulator–insulator contact charging and its relationship to atmospheric pressure," *Journal of Electrostatics,* vol. 61, no. 3, pp. 259-268, 2004/07/01/ 2004.
[118] M. D. Hogue, E. R. Mucciolo, and C. I. Calle, "Triboelectric, corona, and induction charging of insulators as a function of pressure," *Journal of Electrostatics,* vol. 65, no. 4, pp. 274-279, 2007/04/01/ 2007.
[119] T. A. L. Burgo, T. R. D. Ducati, K. R. Francisco, K. J. Clinckspoor, F. Galembeck, and S. E. Galembeck, "Triboelectricity: Macroscopic Charge Patterns Formed by Self-Arraying Ions on Polymer Surfaces," *Langmuir,* vol. 28, no. 19, pp. 7407-7416, 2012/05/15 2012.
[120] A. E. Kovalev and S. N. Gorb, "Charge Contribution to the Adhesion Performance of Polymeric Microstructures," *Tribology Letters,* vol. 48, no. 1, pp. 103-109, 2012/10/01 2012.
[121] N. E. Stork, "Experimental analysis of adhesion of Chrysolina polita (Chrysomelidae: Coleoptera) on a variety of surfaces," *Journal of Experimental Biology,* vol. 88, no. 1, pp. 91-108, 1980.
[122] M. M. Apodaca, P. J. Wesson, K. J. M. Bishop, M. A. Ratner, and B. A. Grzybowski, "Contact electrification between identical materials," *Angewandte Chemie International Edition,* vol. 49, no. 5, pp. 946-949, 2010.
[123] Z. L. Wang, "Triboelectric nanogenerators as new energy technology and self-powered sensors – Principles, problems and perspectives," *Faraday Discussions,* 10.1039/C4FD00159A vol. 176, no. 0, pp. 447-458, 2014.

[124] F.-R. Fan, L. Lin, G. Zhu, W. Wu, R. Zhang, and Z. L. Wang, "Transparent Triboelectric Nanogenerators and Self-Powered Pressure Sensors Based on Micropatterned Plastic Films," *Nano Letters,* vol. 12, no. 6, pp. 3109-3114, 2012/06/13 2012.
[125] G. Zhu *et al.*, "Triboelectric-Generator-Driven Pulse Electrodeposition for Micropatterning," *Nano Letters,* vol. 12, no. 9, pp. 4960-4965, 2012/09/12 2012.
[126] S. Wang, L. Lin, and Z. L. Wang, "Nanoscale Triboelectric-Effect-Enabled Energy Conversion for Sustainably Powering Portable Electronics," *Nano Letters,* vol. 12, no. 12, pp. 6339-6346, 2012/12/12 2012.
[127] W.-Z. Song *et al.*, "Sliding mode direct current triboelectric nanogenerators," *Nano Energy,* vol. 90, p. 106531, 2021.
[128] H. Zou *et al.*, "Quantifying the triboelectric series," *Nature communications,* vol. 10, no. 1, pp. 1-9, 2019.
[129] P. Vasandani, Z.-H. Mao, W. Jia, and M. Sun, "Relationship between triboelectric charge and contact force for two triboelectric layers," *Journal of Electrostatics,* vol. 90, pp. 147-152, 2017/12/01/ 2017.
[130] J. Perris *et al.*, "3D Printing and Rapid Replication of Advanced Numerically Generated Rough Surface Topographies in Numerous Polymers," *Advanced Engineering Materials,* https://doi.org/10.1002/adem.202200832 vol. 25, no. 1, p. 2200832, 2023/01/01 2023.
[131] J. Shao *et al.*, "Studying about applied force and the output performance of sliding-mode triboelectric nanogenerators," *Nano Energy,* vol. 48, pp. 292-300, 2018/06/01/ 2018.
[132] W. Zhang, D. Diao, K. Sun, X. Fan, and P. Wang, "Study on friction-electrification coupling in sliding-mode triboelectric nanogenerator," *Nano Energy,* vol. 48, pp. 456-463, 2018/06/01/ 2018.
[133] W. He *et al.*, "Boosting output performance of sliding mode triboelectric nanogenerator by charge space-accumulation effect," *Nature Communications,* vol. 11, no. 1, p. 4277, 2020/08/26 2020.
[134] Y. Yang *et al.*, "Human Skin Based Triboelectric Nanogenerators for Harvesting Biomechanical Energy and as Self-Powered Active Tactile Sensor System," *ACS Nano,* vol. 7, no. 10, pp. 9213-9222, 2013/10/22 2013.
[135] I.-W. Tcho *et al.*, "Disk-based triboelectric nanogenerator operated by rotational force converted from linear force by a gear system," *Nano Energy,* vol. 50, pp. 489-496, 2018/08/01/ 2018.
[136] S. Wang, L. Lin, Y. Xie, Q. Jing, S. Niu, and Z. L. Wang, "Sliding-triboelectric nanogenerators based on in-plane charge-separation mechanism," *Nano letters,* vol. 13, no. 5, pp. 2226-2233, 2013.
[137] J. L. Armitage, A. Ghanbarzadeh, C. Wang, and A. Neville, "An investigation into the influence of tribological parameters on the operation of sliding triboelectric nanogenerators," *Tribology International,* vol. 155, p. 106778, 2021/03/01/ 2021.
[138] J. Wu, Y. Xi, and Y. Shi, "Toward wear-resistive, highly durable and high performance triboelectric nanogenerator through interface liquid lubrication," *Nano Energy,* vol. 72, p. 104659, 2020/06/01/ 2020.
[139] L. Zhou *et al.*, "Simultaneously Enhancing Power Density and Durability of Sliding-Mode Triboelectric Nanogenerator via Interface Liquid Lubrication," *Advanced Energy Materials,* https://doi.org/10.1002/aenm.202002920 vol. 10, no. 45, p. 2002920, 2020/12/01 2020.
[140] *Standard Test Method for Static and Kinetic Coefficients of Friction of Plastic Film and Sheeting*, 2014.
[141] I. Etsion and L. Burstein, "A Model for Mechanical Seals with Regular Microsurface Structure," *Tribology Transactions,* vol. 39, no. 3, pp. 677-683, 1996/01/01 1996.
[142] S. t. S. Technologies. (22/04/2020). *Silicon wafer specifications*. Available: https://www.siltronix-st.com/en/silicon-wafer/silicon-wafer-specifications

[143] C. Teichert, J. F. MacKay, D. E. Savage, M. G. Lagally, M. Brohl, and P. Wagner, "Comparison of surface roughness of polished silicon wafers measured by light scattering topography, soft-x-ray scattering, and atomic-force microscopy," *Applied Physics Letters,* vol. 66, no. 18, pp. 2346-2348, 1995/05/01 1995.
[144] W. I. Wu, P. Rezai, H. H. Hsu, and P. R. Selvaganapathy, "1 - Materials and methods for the microfabrication of microfluidic biomedical devices," in *Microfluidic Devices for Biomedical Applications*, X. Li and Y. Zhou, Eds.: Woodhead Publishing, 2013, pp. 3-62.
[145] S. Dillavou and S. M. Rubinstein, "Nonmonotonic Aging and Memory in a Frictional Interface," *Phys. Rev. Lett.,* vol. 120, p. 224101, 2018.
[146] A. W. Bush, R. D. Gibson, and T. R. Thomas, "The elastic contact of a rough surface," *Wear,* vol. 35, no. 1, pp. 87-111, 1975/11/01/ 1975.
[147] I. A. Polonsky and L. M. Keer, "A numerical method for solving rough contact problems based on the multi-level multi-summation and conjugate gradient techniques," *Wear,* vol. 231, no. 2, pp. 206-219, 1999/07/01/ 1999.
[148] L. Pastewka, T. A. Sharp, and M. O. Robbins, "Seamless elastic boundaries for atomistic calculations," *Physical Review B,* vol. 86, no. 7, p. 075459, 08/27/ 2012.
[149] S. B. Jaber, A. Hamilton, Y. Xu, M. E. Kartal, N. Gadegaard, and D. M. Mulvihill, "Friction of flat and micropatterned interfaces with nanoscale roughness," *Tribology International,* vol. 153, p. 106563, 2021/01/01/ 2021.
[150] Q. Li, T. E. Tullis, D. Goldsby, and R. W. Carpick, "Frictional ageing from interfacial bonding and the origins of rate and state friction," *Nature,* vol. 480, no. 7376, pp. 233-236, 2011/12/01 2011.
[151] T. Baumberger, P. Berthoud, and C. Caroli, "Physical analysis of the state- and rate-dependent friction law. II. Dynamic friction," *Physical Review B,* vol. 60, no. 6, pp. 3928-3939, 08/01/ 1999.
[152] N. V. Gitis and L. Volpe, "Nature of static friction time dependence," *Journal of Physics D: Applied Physics,* vol. 25, no. 4, pp. 605-612, 1992/04/14 1992.
[153] J. H. Dieterich, "Modeling of rock friction: 1. Experimental results and constitutive equations," *Journal of Geophysical Research: Solid Earth,* https://doi.org/10.1029/JB084iB05p02161 vol. 84, no. B5, pp. 2161-2168, 1979/05/10 1979.
[154] A. E. Filippov, J. Klafter, and M. Urbakh, "Friction through Dynamical Formation and Rupture of Molecular Bonds," *Physical Review Letters,* vol. 92, no. 13, p. 135503, 03/30/ 2004.
[155] Y. Xu, J. Scheibert, N. Gadegaard, and D. M. Mulvihill, "An asperity-based statistical model for the adhesive friction of elastic nominally flat rough contact interfaces," *Journal of the Mechanics and Physics of Solids,* vol. 164, p. 104878, 2022/07/01/ 2022.
[156] A. Papangelo and M. Ciavarella, "On mixed-mode fracture mechanics models for contact area reduction under shear load in soft materials," *Journal of the Mechanics and Physics of Solids,* vol. 124, pp. 159-171, 2019/03/01/ 2019.
[157] J. J. Wortman and R. A. Evans, "Young's Modulus, Shear Modulus, and Poisson's Ratio in Silicon and Germanium," *Journal of Applied Physics,* vol. 36, no. 1, pp. 153-156, 1965/01/01 1965.
[158] Y. Umeno and T. Kitamura, "Ab initio simulation on ideal shear strength of silicon," *Materials Science and Engineering: B,* vol. 88, no. 1, pp. 79-84, 2002/01/02/ 2002.
[159] J. M. Schuster, C. E. Schvezov, and M. R. Rosenberger, "Analysis of the Results of Surface Free Energy Measurement of Ti6Al4V by Different Methods," *Procedia Materials Science,* vol. 8, pp. 732-741, 2015/01/01/ 2015.
[160] F. M. Fowkes, "ATTRACTIVE FORCES AT INTERFACES," *Industrial & Engineering Chemistry,* vol. 56, no. 12, pp. 40-52, 1964/12/01 1964.
[161] D. K. Owens and R. C. Wendt, "Estimation of the surface free energy of polymers," *Journal of Applied Polymer Science,* vol. 13, no. 8, pp. 1741-1747, 1969/08/01 1969.

[162] W. A. Zisman, "Influence of constitution on adhesion," *Industrial & Engineering Chemistry,* vol. 55, no. 10, pp. 18-38, 1963.
[163] M. Tokuda, T. Shindo, and H. Minami, "Preparation of Polymer/Poly(ionic liquid) Composite Particles by Seeded Dispersion Polymerization," *Langmuir,* vol. 29, no. 36, pp. 11284-11289, 2013/09/10 2013.
[164] C. G. Jothi Prakash and R. Prasanth, "Approaches to design a surface with tunable wettability: a review on surface properties," *Journal of Materials Science,* vol. 56, no. 1, pp. 108-135, 2021/01/01 2021.
[165] G. He, M. H. Müser, and M. O. Robbins, "Adsorbed Layers and the Origin of Static Friction," *Science,* vol. 284, no. 5420, pp. 1650-1652, 1999/06/04 1999.
[166] H. G. Howell and J. Mazur, "AMONTONS' LAW AND FIBRE FRICTION," *Journal of the Textile Institute Transactions,* vol. 44, no. 2, pp. T59-T69, 1953/02/01 1953.

Appendices

A. Engineering drawings of the friction rig components

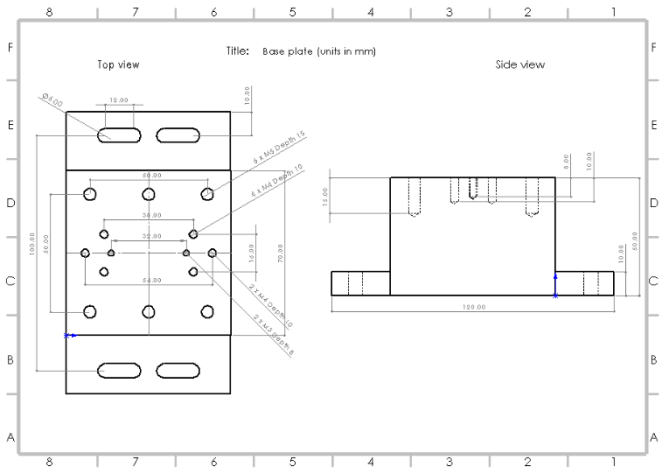

Fig. A 1. Drawing of the base plate that is the base for all the parts on the left side of the rig.

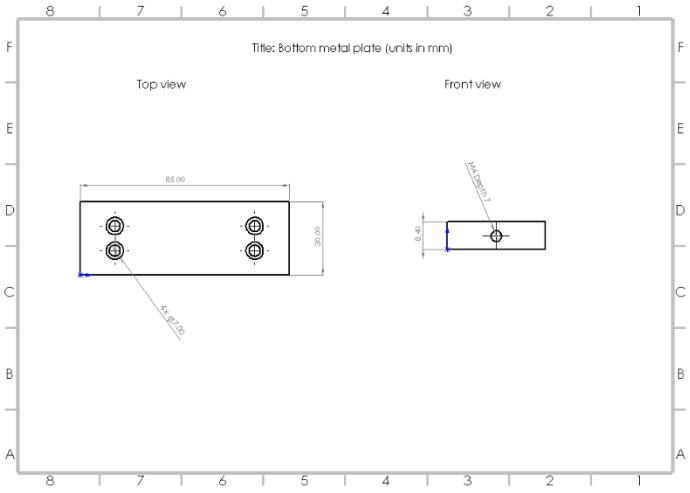

Fig. A 2. The Bottom metal block that is used to place the bottom sample. This part has a hole on one side to connect to either side of the rig.

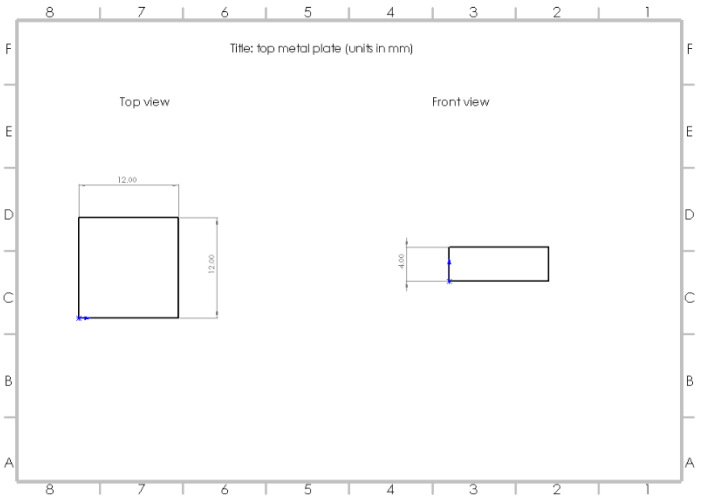

Fig. A 3. The top metal block that is used to place the top sample. The normal load transits through this part

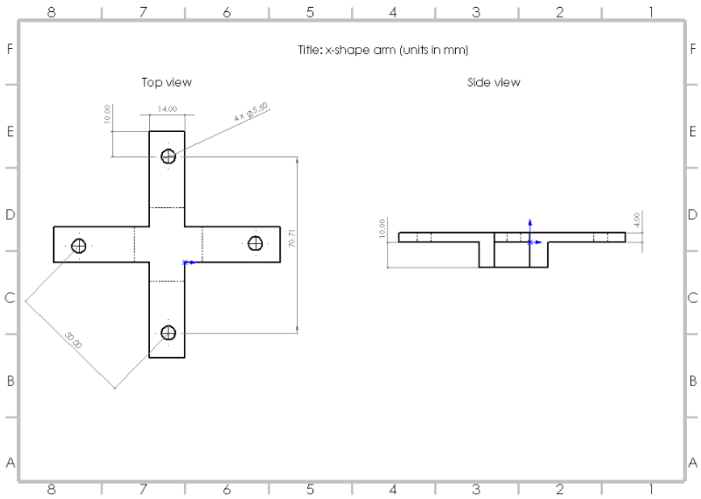

Fig. A 4. The x-shape arm to transmit the load from the compression springs toward the interface.

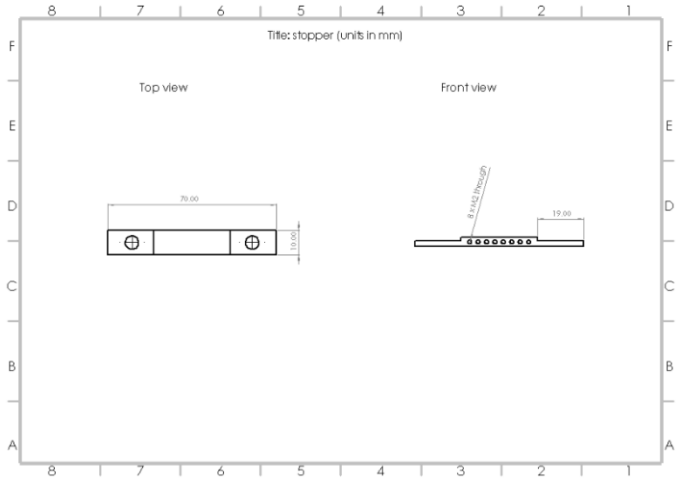

Fig. A 5. The stoppers to constrain the top sample from movement while sliding is taking place. The different holes were drilled to insert small screws at different locations to accommodate a variety of top sample dimensions.

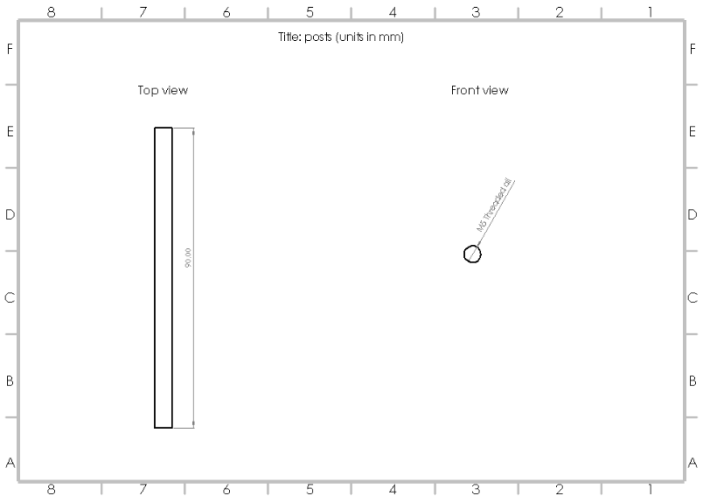

Fig. A 6. The posts to hold the x-shape and stoppers.

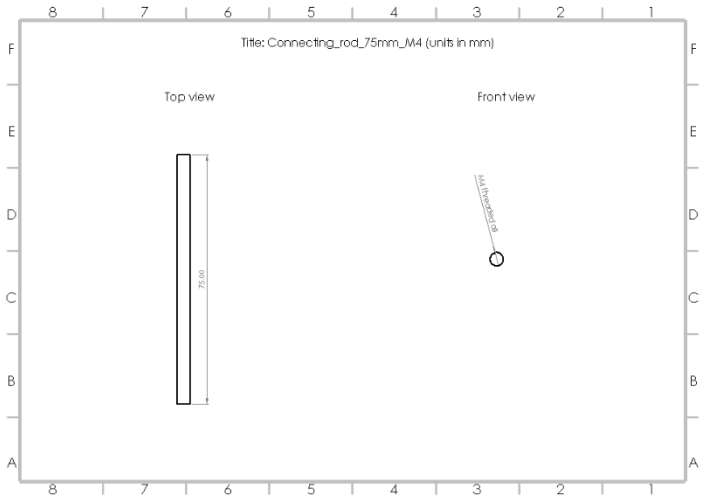

Fig. A 7. The connecting rod between the bottom metal block and connecting cylinder.

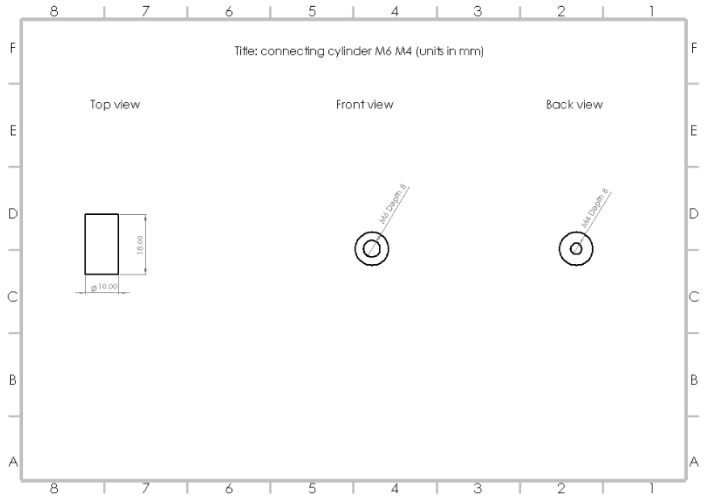

Fig. A 8. The connecting cylinder to switch the M4 connector to the M6 (the one that fits the tension load cell).

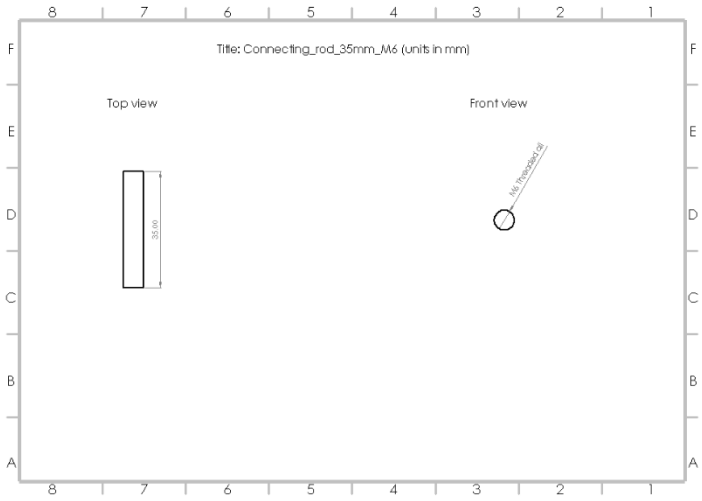

Fig. A 9. The connecting rod with a shorter length to connect the left side of the rig with the right through the tension/compression load cell.

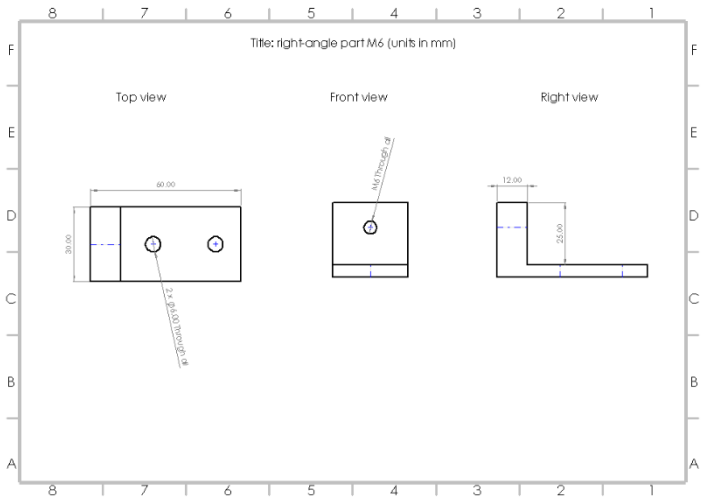

Fig. A 10. The right-angle part to transmit the tangential load from the motor to the interface.

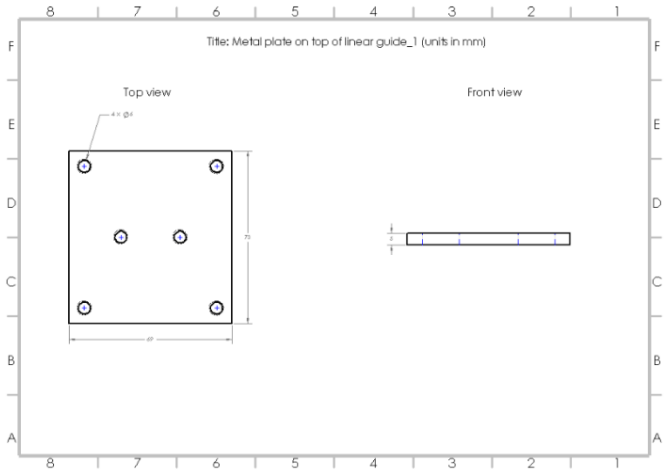

Fig. A 11. The spacer between the right-angle part and linear guide to meet the connecting line.

B. LabView code

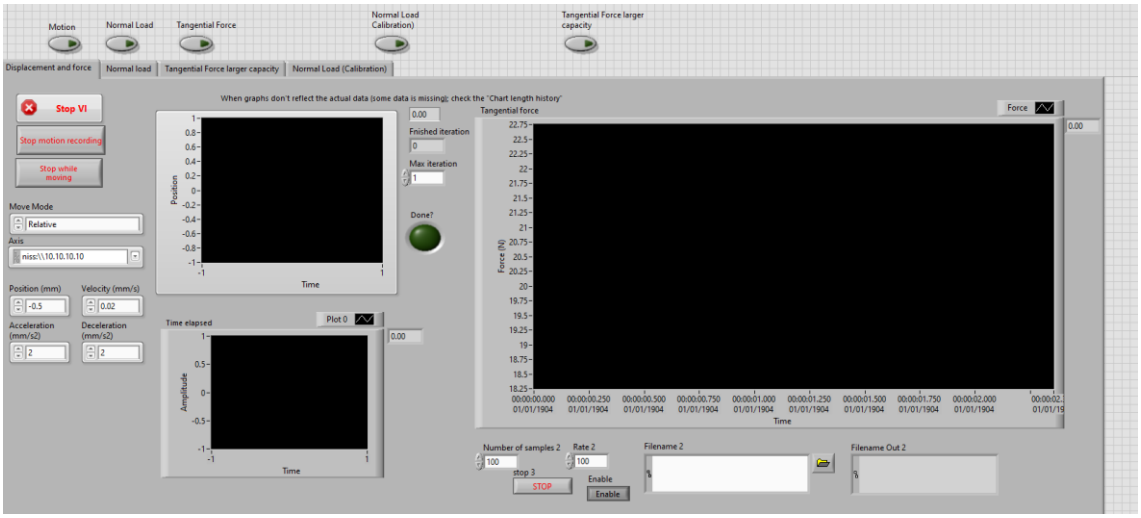

Fig. A 12. The user interface of the unidirectional sliding experiments.

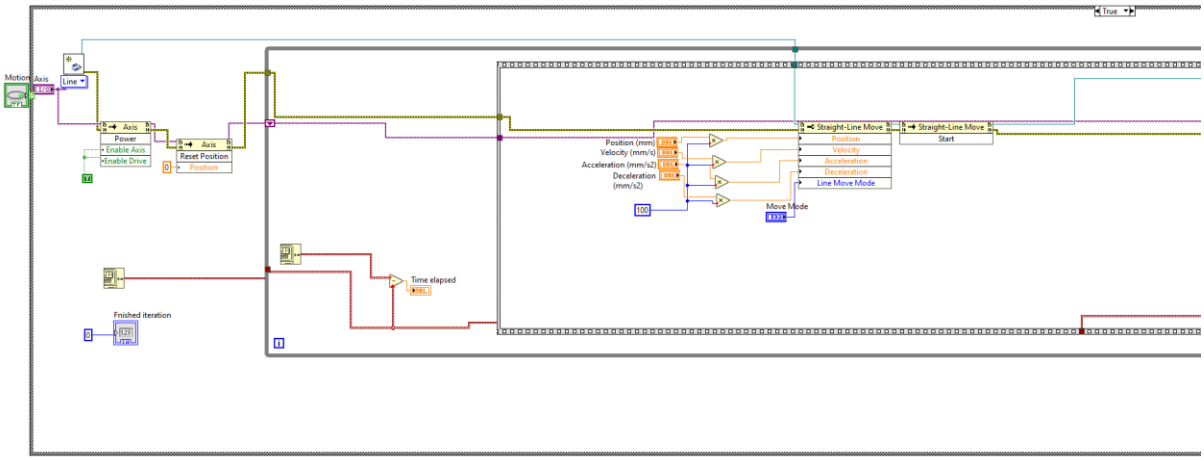

Fig. A 13. The Block diagram of the unidirectional code for the motion control (No. 1).

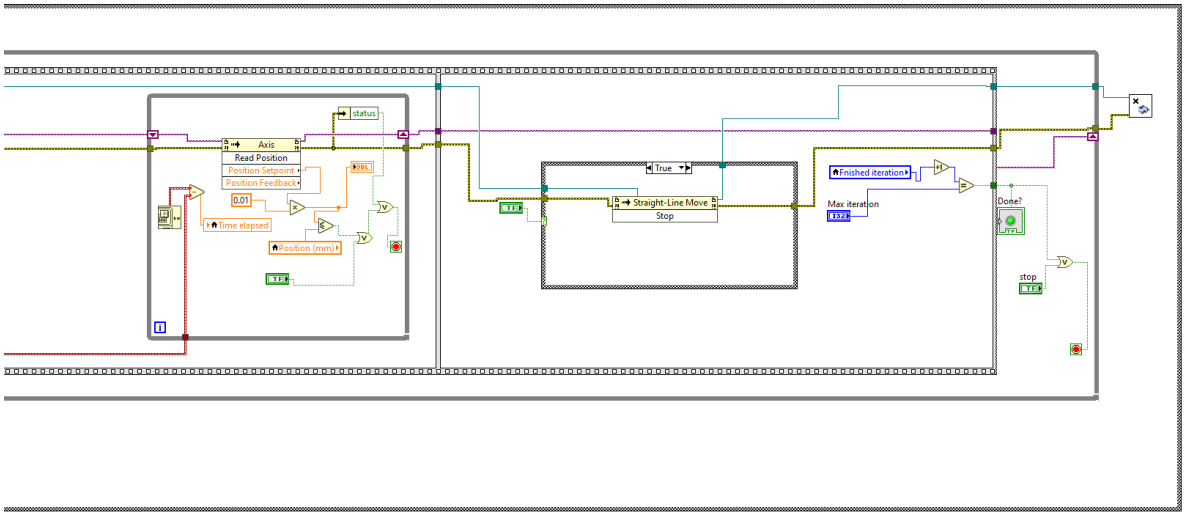

Fig. A 14. The Block diagram of the unidirectional code for the motion control (No. 2).

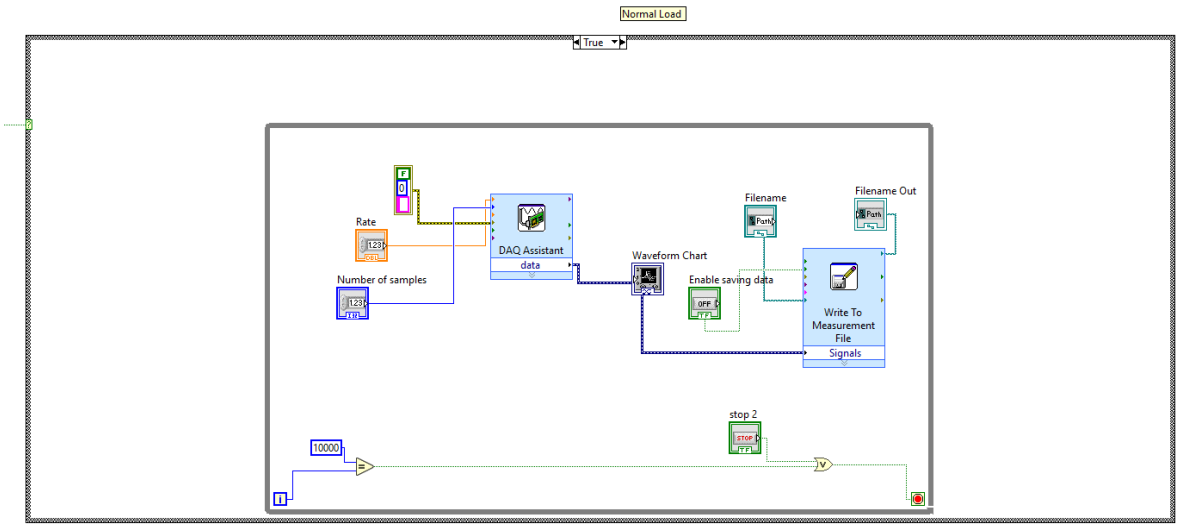

Fig. A 15. The Block diagram of the unidirectional code for the normal load measurement.

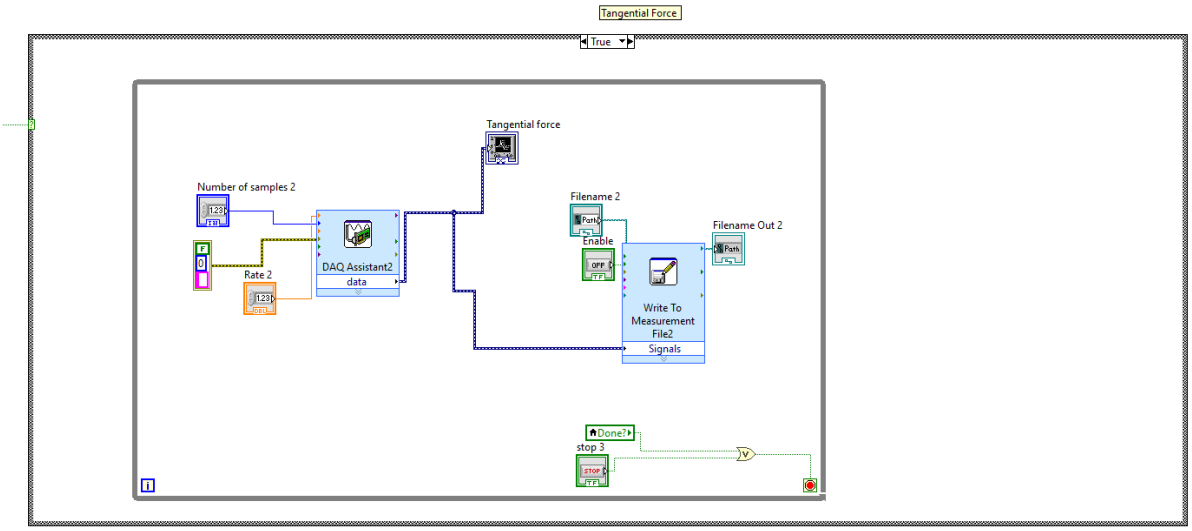

Fig. A 16. The Block diagram of the unidirectional code for the tangential force measurement.

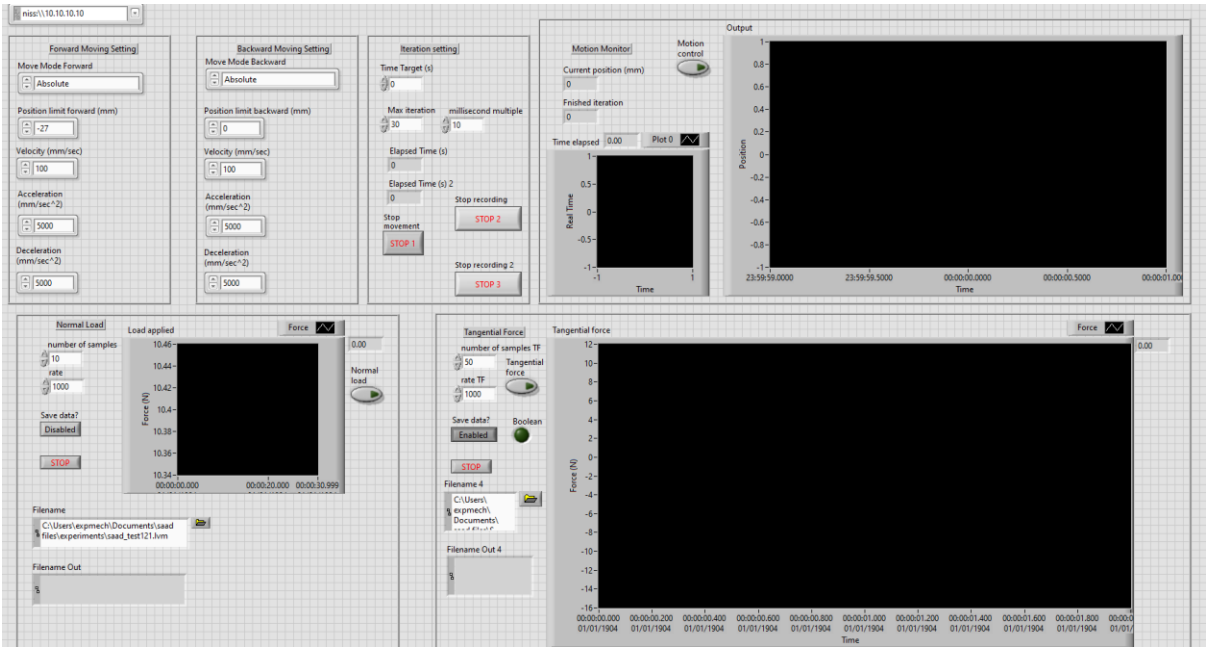

Fig. A 17. The user interface of the reciprocating sliding experiments.

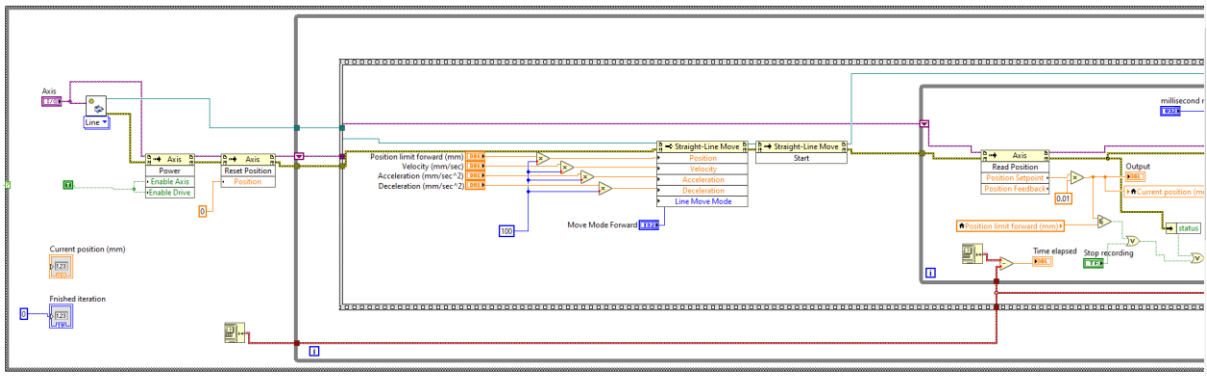

Fig. A 18. The Block diagram of the reciprocating code for the motion control (No. 1).

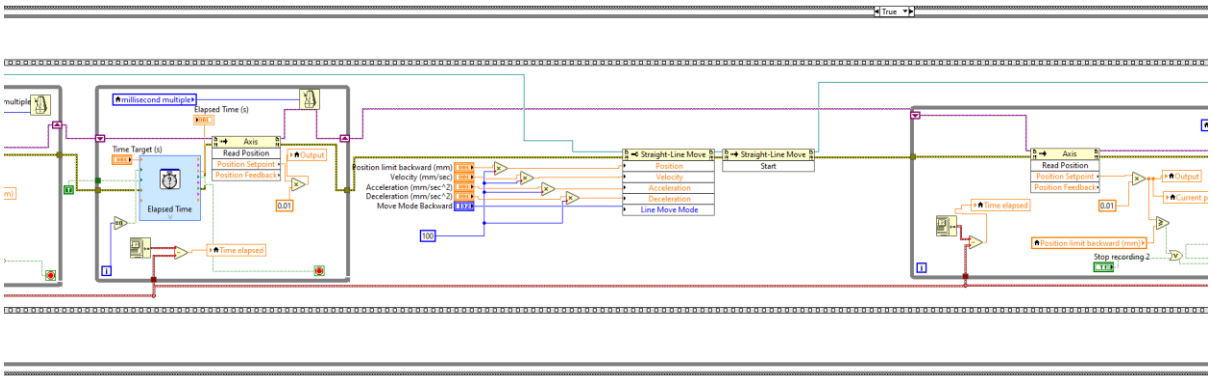

Fig. A 19. The Block diagram of the reciprocating code for the motion control (No. 2).

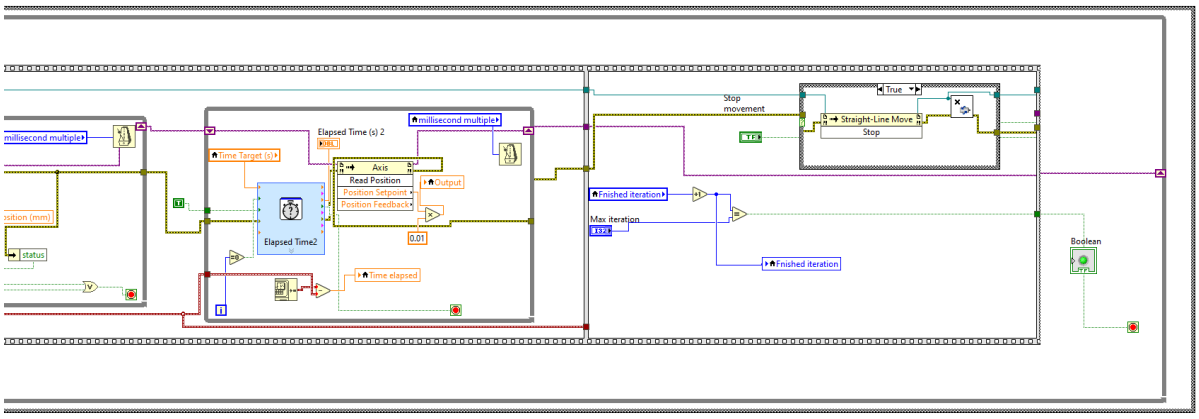

Fig. A 20. The Block diagram of the reciprocating code for the motion control (No. 3).

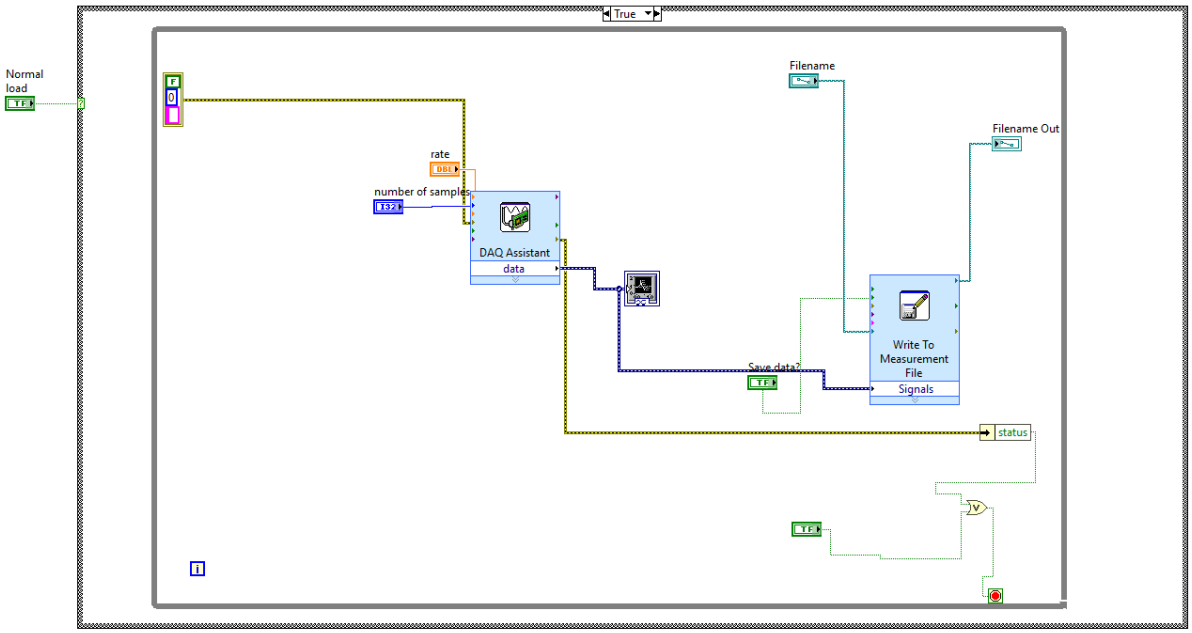

Fig. A 21. The Block diagram of the reciprocating code for the normal load measurements.

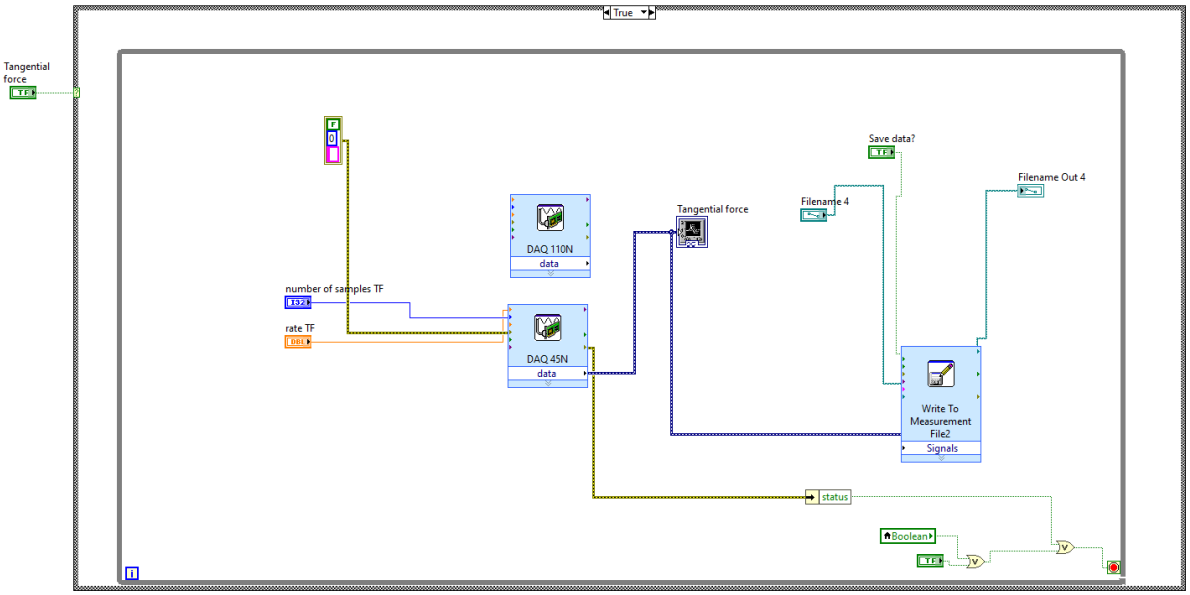

Fig. A 22. The Block diagram of the reciprocating code for the tangential force measurements.

C. Supplementary figures

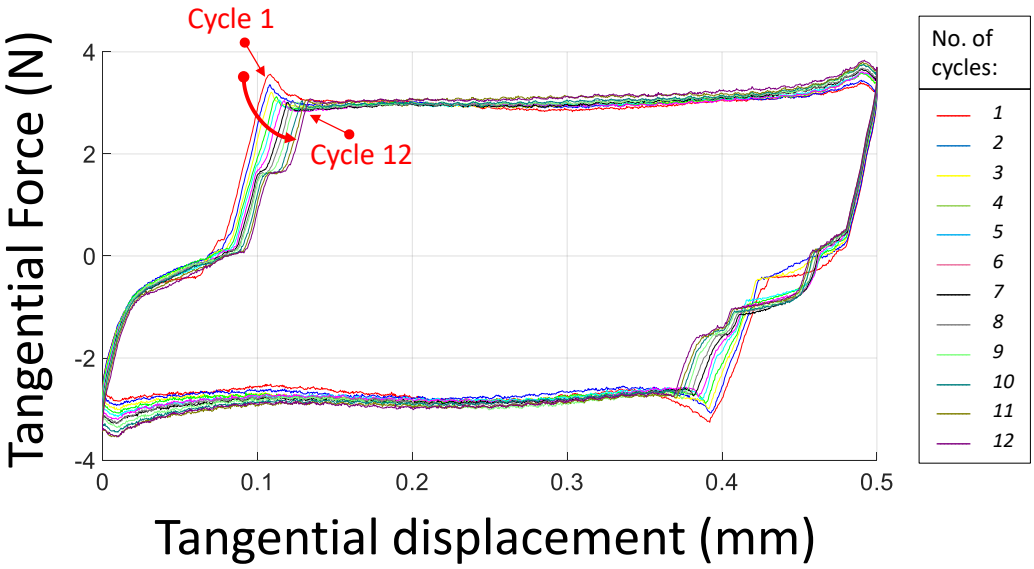

Fig. A 23. The full hysteresis loops for the first 12 cycles presented in Fig. 5. 7.